2010-04-22

Using Buckling-Restrained Braces in Eccentric Configurations

Gary S. Prinz
Brigham Young University - Provo

Using Buckling-Restrained Braces in Eccentric Configurations

Gary S. Prinz

A dissertation submitted to the faculty of
Brigham Young University
in partial fulfillment of the requirements for the degree of

Doctor of Philosophy

Paul W. Richards, Chair
Richard J. Balling
Steven E. Benzley
Fernando S. Fonseca
David W. Jensen

Department of Civil and Environmental Engineering

Brigham Young University

August 2010

ABSTRACT

Using Buckling-Restrained Braces in Eccentric Configurations

Gary S. Prinz

Department of Civil and Environmental Engineering

Doctor of Philosophy

Ductile braced frames are often used to resist lateral earthquake loads in steel buildings; however the presence of a brace element can sometimes interfere with architectural features. One common type of ductile braced frame system sometimes used to accommodate architectural features is the eccentrically braced frame (EBF).

In order to dissipate seismic forces, EBF beam regions (called links) must sustain large inelastic deformations. EBF links with column connections must transmit large moments and shear forces to facilitate link rotation. Experiments have shown that welded link-to-column connections tend to fracture in the link flange prior to large link rotations.

This study investigated methods for improving EBF link-to-column connection performance, and proposed an alternative ductile braced frame system for accommodating architectural features. Several EBF links with reduced web and flange sections were analytically investigated using validated finite element models in ABAQUS. Results indicated that putting holes in the link web reduced stress and strain values in the link flanges at the connection, but increased the plastic strain and stress triaxiality in the web at the edges of holes. Removing area from the link flanges had little effect on connection stresses and strains. Thus, the reduced web section and reduced flange section methods are not a promising solution to the EBF link-to-column connection problem. The alternative braced frame system proposed in the dissertation used ductile beam splices and buckling-restrained braces in eccentric configurations (BRBF-Es) to accommodate architectural features. Design considerations for the BRBF-Es were determined and dynamic BRBF-E performance was compared with EBF performance. BRBF-E system and component performance was determined using multiple finite element methods. Inter-story drifts and residual drifts for the BRBF-Es were similar to those for EBFs. Results indicated that BRBF-Es are a viable alternative to the EBF, and may result in better design economy than EBFs. With the BRBF-E, damage was isolated within the brace, and in the EBF, damage was isolated within the link, indicating simpler repairs with the BRBF-E. Shop welding of BRBF-E members may replace the multiple field welds required in EBF construction.

Keywords: EBF, BRBF-E, dynamic analysis, finite element analysis, steel ductile braced frame, seismic design

ACKNOWLEDGMENTS

The completion of this dissertation research would not have been possible without the help and encouragement of several hard working individuals. First I wish to thank my committee chair, Dr. Paul W. Richards, for his many wise insights, kind encouragement, and for the drive he hit on 9th hole during the civil engineering alumni golf scramble. I also thank Dr. Richard J. Balling, Dr. Steven E. Benzley, Dr. Fernando S. Fonseca, and Dr. David W. Jensen, for serving as members of my graduate committee and teaching me the mysteries of structural engineering in their courses. Additionally, I thank Tom Alley who helped me with some of the EBF designs.

I thank my parents, Steve and Debbie, for their examples and encouragement throughout my life. I thank them for showing me, from an early age, the joy of learning and exploring.

Lastly, this dissertation is dedicated to my wife, Heather, and son, Trevor, who put up with the many, many late nights and long days required to complete this document. Their constant encouragement, love, and support were vital to me finishing.

TABLE OF CONTENTS

LIST OF TABLES

LIST OF FIGURES

xiv

LIST OF TERMS

BRB	Buckling-restrained brace
BRBF	Buckling-restrained braced frame
BRBF-C	Buckling-restrained braced frame in concentric configuration
BRBF-E	Buckling-restrained braced frame in eccentric configuration
CBF	Concentrically braced frame
EBF	Eccentrically braced frame
ELF	Equivalent lateral force
MSC	Mid-splice connection
OpenSEES	Open System for Earthquake Engineering Simulation
PEEQ	Equivalent plastic strain in ABAQUS
PGA	Peak ground acceleration
R	Response modification factor
RBS	Reduced beam section
RFS	Reduced flange section
RWS	Reduced web section
TSC	Top-flange splice connection
A_{brace}	Brace cross-sectional area
A_S	Cross-sectional area of stub connector
a	Radius of hole in infinite plate
b_x	Strong axis bending coefficient
b_y	Weak axis bending coefficient
C_d	Deflection amplification factor

E	Elastic material stiffness (Young's modulus)
F_{brace}	Brace force
$F_{br,i}$	Brace force in ith story
G_S	Shear modulus of stud connector
K_S	Lateral stiffness of stud connector
L_{brace}	Brace length
$L_{br,i}$	Brace length in ith story
L_S	Length of stub connector
M_n	Nominal moment capacity
Pd	Design axial column demand
Pu	Ultimate axial column demand
r	Radial location from center of plate
S_{DS}	Site design spectral accelerations at 0.2 seconds
S_{D1}	Site design spectral accelerations at 1.0 seconds
V	Story shear force
Ve	Elastic story shear force from equivalent lateral force procedure
V_{nx}	Nominal shear capacity
α	Material constant
β	Stiffness proportional damping coefficient
γ_1	Link rotation when the failure index reaches 1.0
Δ_{roof}	Inelastic roof drift
$\dot{\varepsilon}_{ij}^{P}$	Plastic strain rate tensor
$\varepsilon_{p,critical}$	Critical cumulative plastic strain

$\varepsilon_{\theta\theta}$	Tangential strain
ϕ	Resistance factor
σ_e	von Mises stress
σ_m	Hydrostatic stress
σ_m / σ_e	Stress Triaxiality
σ_r	Radial stress
σ_θ	Tangential stress (hoop stress)
$\sigma_{r\theta}$	Radial-tangential stress
τ	Applied shear stress
ω_i	Natural frequency of a mode i
Ω	System overstrength
ζ	Damping ratio

Chapter 1: INTRODUCTION

1.1. Background

Design of steel buildings for seismic loads is generally based on two performance objectives: (1) elastic response during minor to moderate earthquakes, and (2) collapse prevention during extreme (rare) earthquakes. To meet these objectives, buildings are typically designed with enough lateral stiffness to limit large displacements during minor to moderate earthquakes, and with enough ductility to survive large inelastic displacements and prevent collapse during extreme earthquakes. Such a design is often achieved using ductile braced frame systems.

Ductile braced frame systems have both high lateral stiffness and ductility. The high lateral stiffness is provided by a bracing element and the ductility is usually provided by an inelastic mechanism specially designed to isolate frame damage during overloading. Two of the most common types of ductile braced frame systems are eccentrically braced frames (EBFs) and buckling-restrained braced frames (BRBFs).

1.2. Overview of Ductile Braced Frame Systems

1.2.1. Eccentrically Braced Frames (EBFs)

Under severe earthquake loading, eccentrically braced frames (EBFs) dissipate energy as stiffened beam segments, called links, rotate inelastically. These links are typically formed from eccentricities between two brace connections, or between a brace connection and column (see

Fig. 1-1).   Shorter links that rotate due to web shear yielding are more common than longer links which develop flexural hinges at each end (see Fig. 1-2).

Links in EBFs are designed to act as structural fuses, localizing frame damage within link regions during overloading. When links are properly designed, the columns, braces, and beam regions outside the links will remain essentially elastic [1].

EBFs have an advantage over concentrically braced frames (CBFs), in that they can accommodate various architectural features. The eccentricity used to create links in EBFs, provides room for doors, windows, and hallways, allowing access through the frame. Braces in typical concentric configurations get in the way of such features. Fig. 1-3 shows the architectural benefits of EBFs, as compared to typical CBF systems.
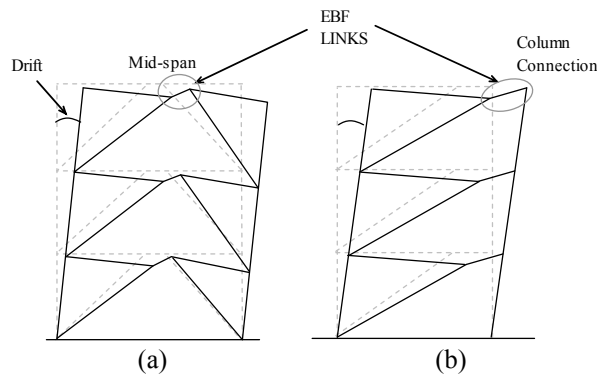
Fig. 1-1 Typical eccentrically braced frames with (a) mid-span links and (b) links with column connection
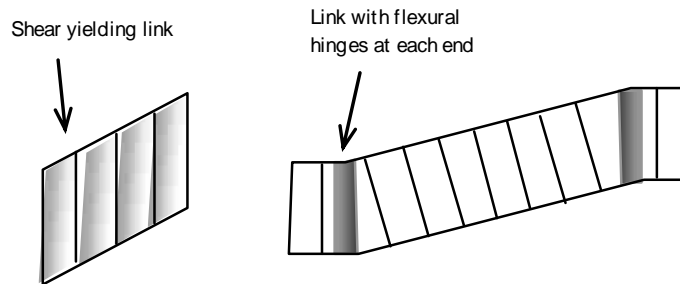
Fig. 1-2 Typical link inelastic behavior

2
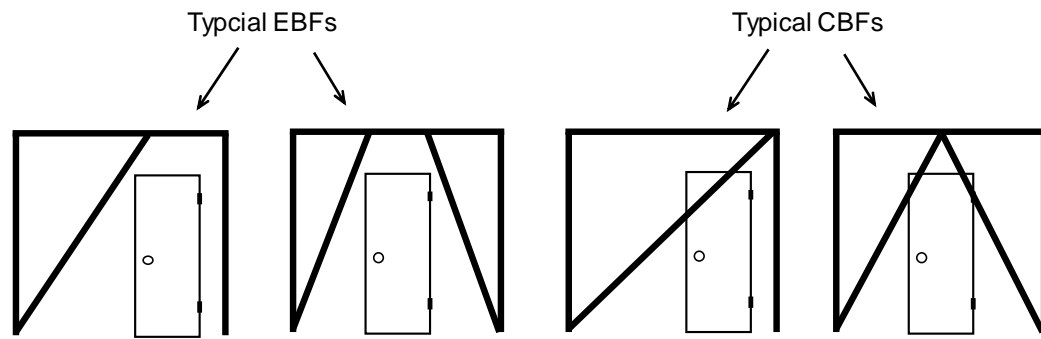
Fig. 1-3 Comparison of EBF and CBF architectural flexibility

1.2.2. Buckling-Restrained Braced Frames (BRBFs)

Buckling-restrained braced frames (BRBFs) are a special type of concentrically braced frame which uses buckling restrained braces. Under severe earthquake loading, BRBFs dissipate energy through axial yielding of the buckling-restrained brace core. The typical concentric configuration of the buckling restrained braces in BRBFs interferes with architectural features (see Fig. 1-3). Buckling-restrained braces are a relatively new type of brace which performs equally well in tension and compression [2,3,4,5]. This symmetric hysteretic behavior provides improved ductility over traditional braces which are limited by poor post-buckling resistance to compressive loads. The symmetric hysteretic behavior of the brace is achieved through its composition. Buckling-restrained braces are comprised of a steel core confined in a concrete filled steel casing (see Fig. 1-4). The core is designed to axially resist the lateral forces while the concrete confinement prevents buckling of the core. A releasing agent, incorporated between the confining material and core, prevents shear transfer and allows for barreling of the steel when in compression.

3
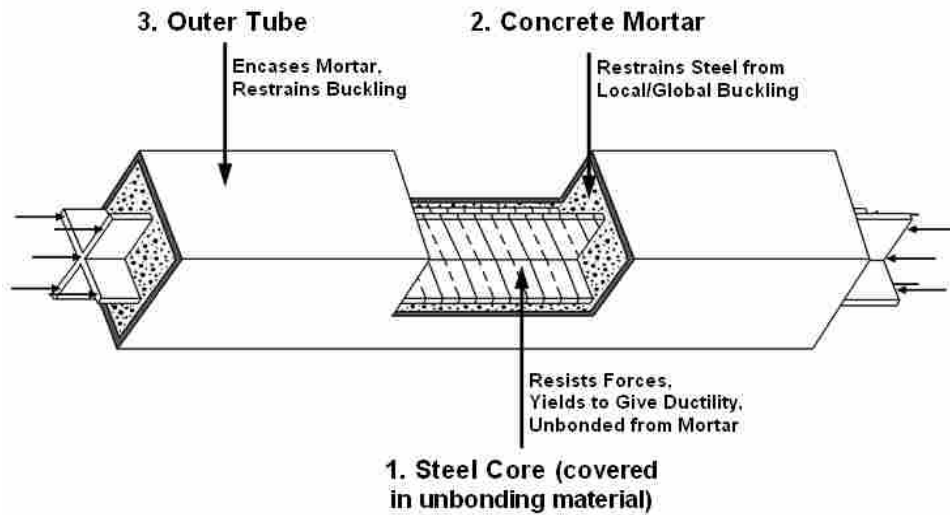
Fig. 1-4 Buckling-restrained brace schematic [6]

1.3. Ductility Issues with EBF and BRBF Connections

Although EBFs and BRBFs are commonly used in steel buildings to resist lateral earthquake loads, recent experimental testing indicates the potential for non-ductile failures near connection regions.

1.3.1 EBF Link-to-Column Connections

Experimental testing has shown that links with column connections (Fig. 1-1b) have less inelastic rotation capacity than mid-span links (Fig. 1-1a), because they tend to fracture in the flange at the connection. Okazaki et al. [7] tested link-to-column connections under cyclic loading and reported the inelastic rotation capacity of links with various link-to-column connection details. Of the twelve W18x40 links tested in [7], ten experienced fracture of the link flanges near the welds at rotations from 0.007 to 0.07 rad. One specimen with a connection that followed the modified welding recommendations outlined in FEMA-350 [8] experienced fracture after 0.05 rad (see Fig. 1-5). Comparable mid-span links achieved rotations beyond 0.08 rad [9].

4

Several additional experimental tests on EBF links with column connections indicate connection failures similar to those observed by Okazaki et al. [7] [10,11,12].

Fig. 1-5 Fracture of specimen MWS at the link-to-column connection [13]

1.3.2. BRBF Gusset Connections

Large-scale testing of BRBFs has shown localized damage within the stiffened gusset connection regions. Roeder et al. recently tested five full-scale BRBF specimens having different gusset connection details [14]. Each frame was subjected to cyclic loading, but concrete slab effects were not considered. The test results indicated that the energy dissipation capacity of the BRBFs was limited by poor performance of the gusset connections. Of the five BRBFs tested in [14], all experienced out-of-plane distortions of the gusset plates leading to ductile tearing near the gusset welds at rotations less than 0.03 rad. In addition to the gusset fractures, test specimen BRB1 developed beam fractures.

Earlier testing of three full-scale BRBF specimens by Aiken et al. [15] indicates connection failures similar to those observed in [12]. Three BRBF specimens tested in [15], all experienced significant yielding in the gusset-beam-column connections and two experienced

gusset-to-beam and gusset-to-column connection fractures at rotations less than 0.03 rad. In the tests, the damage to the connection regions was attributed to pinching of the gussets caused by deformations between the beam and column. All frames were loaded in-plane using cyclic loading protocols and concrete slabs were not considered in the testing.

A full-scale three story BRBF building, with concrete slab, tested by Chen et al. [16] also experienced damage in the beam-column-gusset connection regions. At each floor level, severe buckling, yielding, and out-of-plane displacement of the brace gussets was observed. This damage was observed during drifts as low as 0.02 rad. Subsequent drifts of 0.025 rad caused fractures in the brace end connections. Crushing of the concrete slab occurred at each floor near the beam-column-gusset connections. The test frames were loaded in plane using pseudo-dynamic loading procedures.

1.4. Ductile Beam Splices

A few recent studies using ductile beam splices have shown reductions in BRBF connection damage. A full-scale four story frame having buckling-restrained braces tested by Fahnestock et al. [17] sustained frame drifts near 0.05 rad with little damage to the beams columns or gussets. The frame used beam splices outside the gussets with structural T's joining the beam sections at the web (see Fig. 1-6(a)). In different testing by Coy [6], frame connections achieved rotations greater than 0.06 rad with minimal damage using a beam splice with flange connector plates (see Fig. 1-6(b)). In [17], pseudo-dynamic loads simulated earthquake ground motions; in [6], static cyclic loading protocols replaced dynamic earthquake loads. Concrete slab effects were not considered in either study.

Analytical research by Prinz and Richards [18] investigated BRBFs with beam splice connections at the system level. The study used dynamic nonlinear finite element analysis and a

low-cycle fatigue failure criterion [19] to investigate the beam splice connection tested by Coy [6].   Results indicated that the beam splice connection was effective in reducing stress concentrations at the gusset connections. Also, frame drift values between the spliced and un-spliced connections remained essentially the same, indicating no lateral stiffness loss with the beam splice.   A previously recorded earthquake ground motion, applied in three different directions, loaded the frames.   Interaction between the concrete slab and steel beams was not considered; rather, column constraints simulated a rigid slab by forcing column displacements to be equal.

(a)   (b)
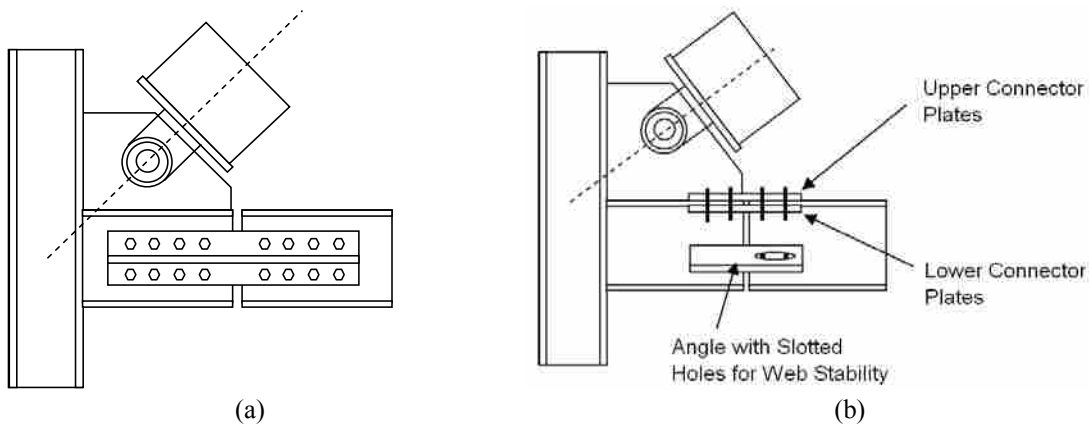
Fig. 1-6 Beam splices: (a) as used by Fahnestock et al [17]; and, (b) as tested by Coy [6]

1.5. Dynamic Finite Element Analysis

Dynamic finite element analysis is a useful tool for analyzing structural response during earthquakes. Traditionally, dynamic earthquake studies predict structural response using beam and truss elements with lumped plasticity. This approach has adequately predicted system structural response in several steel frame studies [20,21,22,23]. However, the lumped inelastic behavior must be determined prior to analysis and the limited geometry definition limits prediction of frame component behavior (connection stresses, local member buckling, and

7

material fatigue).   Also, determining the inelastic behavior for the elements often requires experimental component testing, making it difficult to investigate new connections or members.

Unlike the traditional approach which requires experimental testing to determine inelastic response, dynamic analyses with shell elements need only geometry and material behavior to predict frame component damage.   A recent study by Richards and Prinz [24] compared the predictive capabilities of the traditional non-linear dynamic analysis approach with analyses where connections were modeled explicitly with shell elements.   The shell elements modeled the connection geometry and a stress-modified-strain failure criterion [19] was used to predict local material fatigue.   Both modeling approaches predicted similar system frame behavior (system drifts, velocities, and accelerations); but explicitly modeling the connections in the dynamic analysis allowed much better prediction of material fatigue and plastic strain demands within the connection regions.

1.6. Research Needs

Traditionally, EBFs have been used to accommodate architectural features in braced bays; however, the number of available EBF configurations is limited by the poor performance of link-to-column connections. The poor performance of link-to-column connections has led the current AISC Seismic Provisions [25] to require pre-qualification (experimental testing) of all link-to-column connections prior to use in design, affecting EBF economy.   Additionally, damage to EBF links requires the replacement of entire beams, an expensive and time-consuming repair. Economical solutions that improve the performance of EBF link-to-column connections are needed.   Additionally, there is a need for new and improved braced frame systems that can limit frame damage to easily repairable regions, while still accommodating architectural features.

Methods used to improve BRBF performance may help limit damage to EBF beams, improve frame ductility, and increase architectural flexibility. Ductile beam splices and buckling-restrained braces, incorporated into EBF configurations, have the potential to limit frame damage and improve ductility by moving the inelastic mechanism into the brace and by providing hinges in the beam to accommodate large deformations. Fig. 1-7 shows a typical EBF and an EBF with beam splices and buckling-restrained braces. Research is needed to determine the seismic performance of such frames.
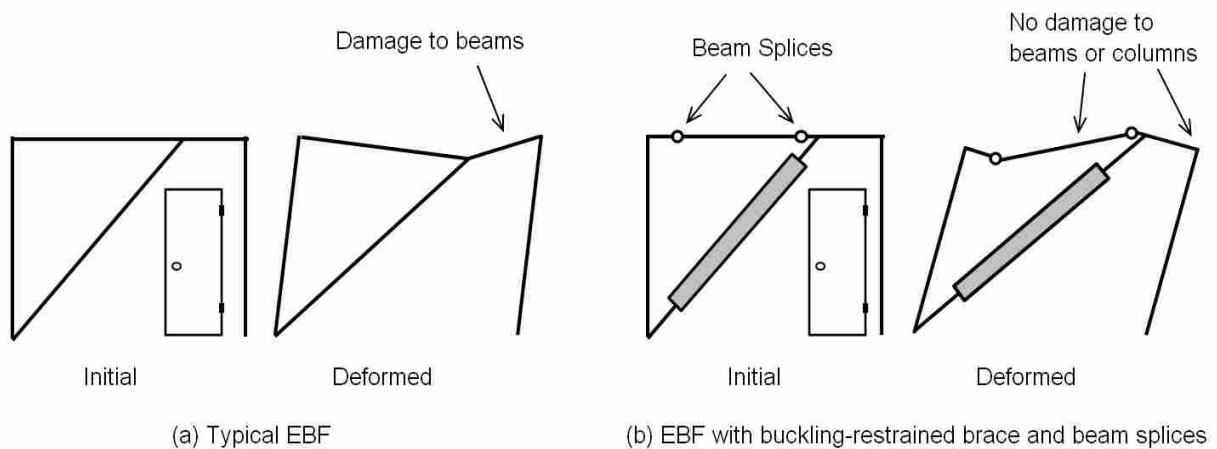
Fig. 1-7 Typical EBF and proposed EBF with buckling-restrained brace and beam splices

1.7. Research Objectives

The following objectives for the dissertation research pertain to the abovementioned research needs.

Dissertation Objectives:

1. Investigate methods for improving link-to-column connection performance in typical EBFs.

2. Develop a new eccentric braced frame system, using beam splices and buckling-restrained braces, which can accommodate architectural features and be easily repaired following a design-level seismic event.

3. Develop efficient analytical modeling techniques for system-level dynamic analysis of steel braced frames with concrete slabs and validate them using existing experimental testing.

4. Analyze the frames developed in Objective 2 using the system-level dynamic modeling techniques developed in objective 3.

5. Develop design recommendations for the new frame developed in Objective 2.

1.8. Organization of the Dissertation

The dissertation is organized into five chapters and five appendices, including this current chapter. Descriptions for the remaining chapters (Chapters 2 through 5) are provided in following paragraphs.

Chapter 2 investigates the effectiveness of removing portions of the EBF link web and link flange in an attempt to limit forces that could develop at the connections and thereby increase connection rotation capacity. Finite element models of several shear yielding links with web and flange cuts are analyzed under cyclic loading. Modeling techniques are validated using data from previous experiments.

In Chapter 3, design considerations for buckling restrained braced frames in eccentric configurations (BRBF-Es) are developed, and the seismic performance of several BRBF-E and EBFs are compared. A comparison study, consisting of 12 BRBF-E and 12 EBF designs, was

developed to investigate the relative seismic performance of BRBF-Es as compared to typical EBFs.   Planar finite element models are subjected to a suite of 10 scaled earthquake accelerations.   Following the comparison study, a BRBF-E design example is presented, and conclusions regarding BRBF-E system behavior are summarized.

In Chapter 4, system level dynamic modeling techniques of ductile braced frames are validated using existing shake table testing, and localized seismic demands in BRBF-Es are investigated.   The system level dynamic response of a five story building having buckling-restrained braces is compared with full-scale shake-table test data obtained from the E-Defense Hyogo Earthquake Engineering Research Center in Tokyo, Japan.   The comparison study focuses on maximum story drift, maximum story displacement, maximum story accelerations, and local column strain response values.   Modeling techniques for the buckling-restrained braces, concrete slab, concrete-slab to beam connections, and gusset connection regions are presented.   Following the validation of modeling methods, two addition BRBF-E models are created and analyzed under multi-directional dynamic loads.   With the additional models, localized connection demands and beam-splice connection types are investigated.   Conclusions regarding BRBF-E seismic performance are summarized.

Chapter 5 summarizes the dissertation work and presents key conclusions regarding ductile braced frame systems having architectural flexibility. A list of the relevant contributions made to field of structural engineering is provided.

Chapter 2: ANALYTICAL INVESTIGATION OF EBF SHORT LINKS WITH REDUCED WEB AND FLANGE SECTIONS

2.1. Introduction

Eccentrically braced frames (EBFs) have good ductility if the links can accommodate the inelastic rotations imposed by severe seismic loading. Most of the experimental testing to determine link inelastic rotation capacity, has addressed shear-yielding links located at beam mid-spans (Fig 2-1a) [26,27,28]. Link experiments with A992 steel indicate that shear-yielding links located at beam mid-spans should be able to achieve inelastic rotations beyond 0.08 rad [9].

Links with column connections (Fig. 2-1b) have less inelastic rotation capacity than mid-span links (Fig. 2-1a), because they tend to fracture in the flange at the connection. Okazaki et al. [7] tested link-to-column connections under cyclic loading and reported the inelastic rotation capacity of links with various link-to-column connection details. Of the twelve W18x40 links tested, ten experienced fracture of the link flanges near the connection at rotations from 0.007 to 0.07 rad. The specimen with a connection that followed the modified welding recommendations outlined in FEMA-350 [8] experienced fracture after 0.05 rad.

The 2005 Seismic Provisions [29] acknowledge the present difficulties with link-to-column connections. The commentary reminds engineers that this is a topic of ongoing research and suggests that it may be wise to avoid these connections altogether until a good solution is found.
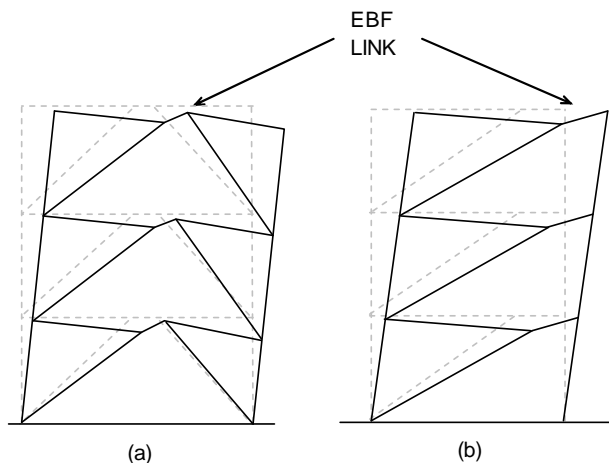
Fig. 2-1 Typical eccentrically braced frames with (a) link at center of beam and (b) link with column connection

Some of the methods developed to improve steel moment frame connections after the Northridge California earthquake may be helpful in improving link-to-column connections. Reduced beam section (RBS) moment connections limit connection demands by weakening the flange a short distance from the connection. Another scheme, which was investigated by Aschheim and Halterman but has not seen widespread implementation, limits connection demands by putting holes in the beam web [30]. The second approach may be good for protecting link-to-column connections for shear yielding links, because removing material from the web is the most direct way to limit the shear capacity of a link.

While including holes in the link web might limit forces at the link-to-column connection, elastic theory indicates that holes will cause stress concentrations in the remaining web material. The case of a thin plate in pure shear with a circular hole (Fig. 2-2) is similar to the case of a link web with a circular area reduction. The stresses in the plate can be derived from the classical solution for a thin plate with a circular hole in tension [31]. The radial stress (σ_r), tangential stress (σ_θ) and shear stress ($\sigma_{r\theta}$) in the plate due to shear loading are:

$$\sigma_r = \tau(1 + \frac{3a^4}{r^4} - \frac{4a^2}{r^2})\cos 2\theta \qquad\qquad (2\text{-}1)$$

$$\sigma_\theta = -\tau(1 + \frac{3a^4}{r^4})\cos 2\theta \qquad\qquad (2\text{-}2)$$

$$\sigma_{r\theta} = -\tau(1 - \frac{3a^4}{r^4} + \frac{2a^2}{r^2})\sin 2\theta \qquad\qquad (2\text{-}3)$$

where: r, τ, a and θ, are the distance from the hole center, applied shear stress, radius of the hole, and counter clockwise angle relative to a horizontal datum [see Fig. 2-2(a)], respectively. Fig. 2-2(b) shows the distribution of tangential stress (hoop stress) in the remaining plate. From Fig. 2-2(b), a tangential stress concentration of four times the applied shear stress can be seen at the edge of the hole.
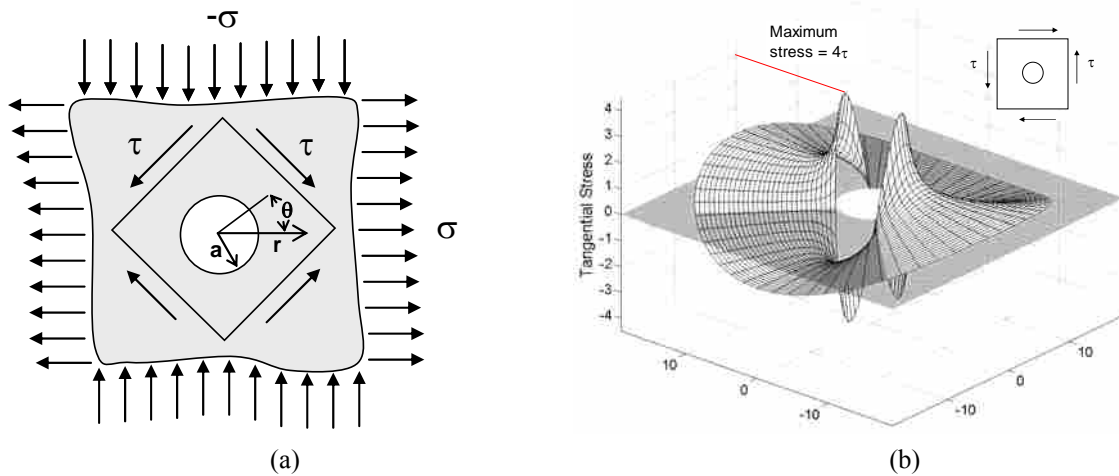
Fig. 2-2 (a) Classical problem of infinite plate with circular hole subjected to shear loading; and, (b) tangential stress distribution in plate with hole subjected to shear

While the link web provides the majority of the shear resistance, the link flanges can also contribute. In a study on link overstrength, Okazaki et al. [9] found that built-up short links with heavy flanges typically had larger than anticipated overstrength factors. Richards [32] explained this overstrength as flange shear contribution. Fig. 2-3 shows the web and flange contribution as

15

described by Richards, with shear resistance coming from the link web and additionally from the link flanges which act as slender beams once the web has fully yielded [32]. Prior to web yielding however, elastic stress analysis suggests that the flange shear contribution is small. Fig. 2-4 shows the shear stress distribution in a general wide flange link, with the maximum shear stress in the flange equal to:

$$\tau_{MAX} = \frac{V \cdot L \cdot t_F \cdot (d - \frac{t_F}{2})}{I \cdot h} \tag{2-4}$$

where τ_{MAX}, V, L, t_F, d, I and h are the maximum shear stress in the flange, story shear, frame length, flange thickness, link depth, link moment of inertia, and frame height respectively. Because the flanges have the potential to contribute to the link shear capacity, it is possible that removing flange material may also help reduce link shear capacity; however, since flange shear contribution is small until the web has significantly yielded, the effect of flange area removal on connection demands may be negligible.

| (a) Total Link Shear | (b) Web Contribution | (c) Flange Contribution |
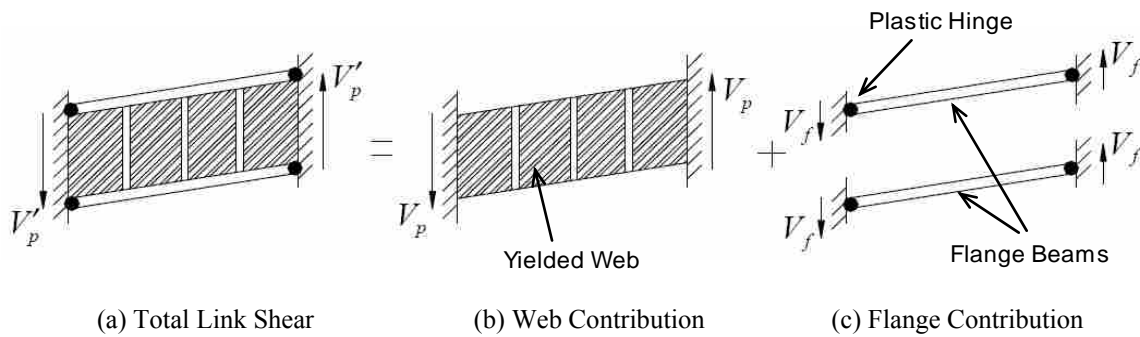
Fig. 2-3 Flange contribution to link shear strength [32]

16

$$\tau_{MAX} = \frac{V \cdot L \cdot t_F \cdot (d - \frac{t_F}{2})}{I \cdot h}$$

General EBF with link-to-column connection

Section A-A
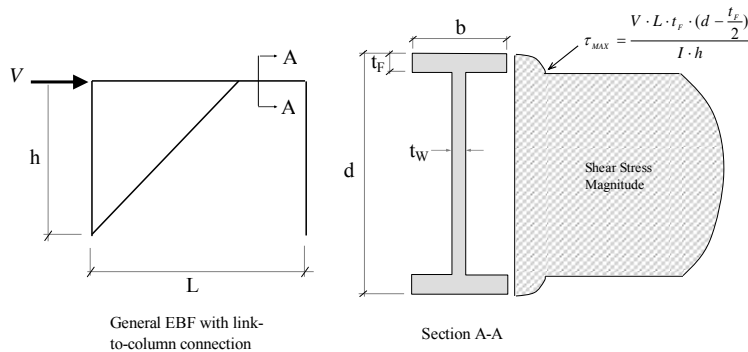
Fig. 2-4 Elastic shear stress distribution in general EBF link

In previous studies, finite element models of EBF links have demonstrated good prediction of link behavior under cyclic loading. Richards and Uang [33] used finite element models of links to predict strength loss due to flange and web local buckling. Berman and Bruneau [34] used finite element models to investigate the behavior of tubular links. Both of these studies were performed in parallel with experimental programs, providing opportunities for extensive model validation. The models in [33] and [34] were shown to have hysteretic behavior and overall deformation patterns that were consistent with the experimental results in [35] and [34].

This chapter discusses an analytical investigation to evaluate the performance of EBF links with portions of the link web and link flanges removed. Since it is possible that removing web material may cause more harm than good, and removing flange material may have negligible effects, the concept was investigated with analytical methods before attempting experimental investigation. The chapter begins by discussing modeling techniques and validation methods for a control link having no web reductions. Included in the discussion are: the model constraints, material properties, element types, and failure criteria used. Then, the models with web section reductions are discussed, followed by a discussion of models with reduced flange sections, which form the basis of the study. Finally, results from the validation model and study

models are presented, and conclusions regarding EBF links with reduced web sections and reduced flange sections are given.

2.2. Finite Element Modeling

2.2.1. Modeling Methods

2.2.1.1. Geometry and Constraints

A control model simulated the test setup and cyclic loading protocol used by Okazaki et al. [7], allowing modeling techniques to be validated with existing experimental data. The specific link specimen simulated by the control model was specimen MWS, which had a welded link-to-column connection based on the modified welding recommendations outlined in FEMA-350 [8]. ABAQUS [36] was used for the analyses.

Displacement constraints simulated the boundary conditions and loading present in the experimental set-up. The constraints are shown in Fig. 2-5. Roller supports located at the top and bottom of the column prevented column rotation. Two other roller supports prevented vertical displacement of the beam. Applied displacements at the bottom of the column simulated the hydraulic loading ram.

2.2.1.2. Elements and Material

Three element types were used to facilitate efficient cyclic nonlinear analysis. Solid elements were used for the link and column flanges in the connection region, while shell elements were used for the link web, column web, and flanges away from the connection (see Fig. 2-6). Shell-to-solid coupling constraints ensured moment transfer at the shell-to-solid element transitions (see Fig. 2-7). In the beam region outside the link, where no yielding was expected, an elastic beam element was used (see Fig. 2-5).
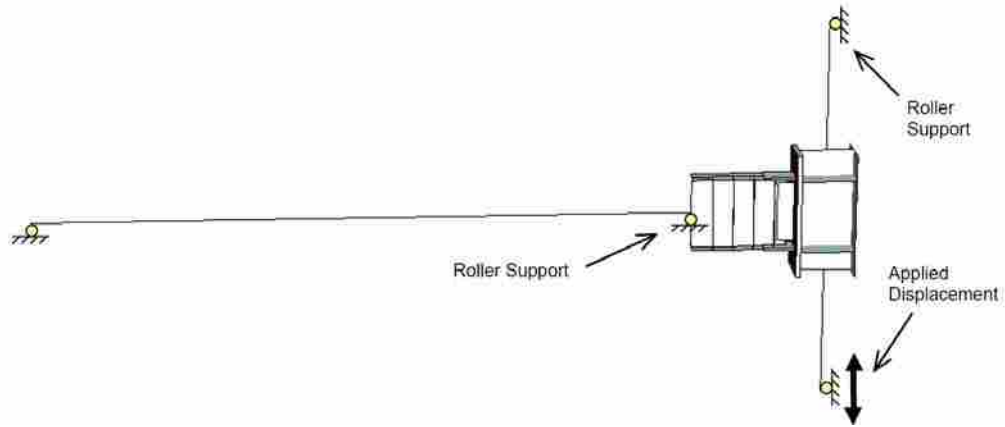
Fig. 2-5 Representation of the model displacement constraints
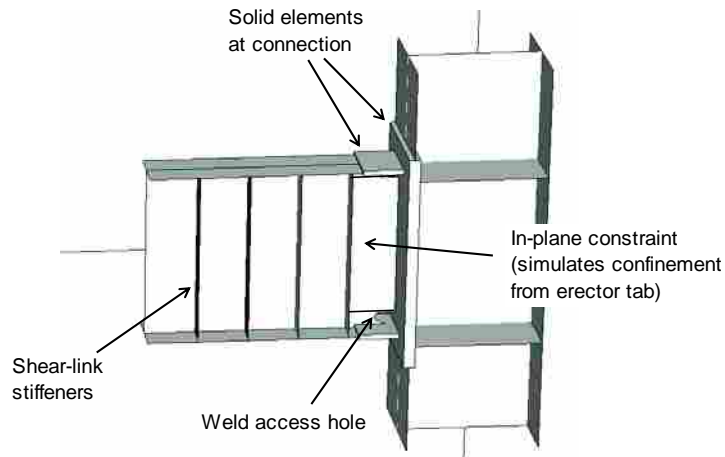
Fig. 2-6 EBF control link modeling techniques
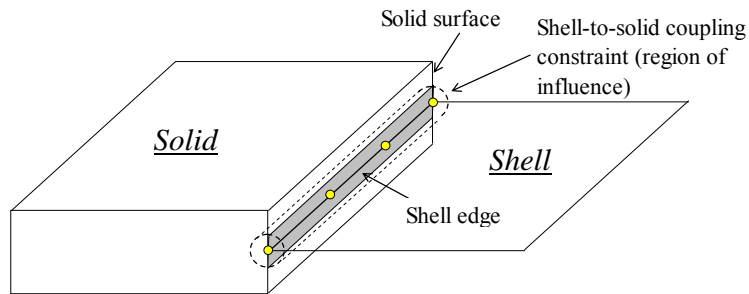
Fig. 2-7 Shell-to-solid coupling constraint [36]

The erector tab present in experimental testing was accounted for using boundary conditions and increased element thickness. The element thickness of the link web was increased at the erector tab connection to account for fusion between the link web and the erector tab. To simulate the influence of the erector tab in inhibiting web buckling, the first panel region in the model was constrained to remain in plane (see Fig. 2-6). Shear transfer through the bolts of the erector tab was neglected; this resulted in somewhat less shear transfer through the link web and somewhat more shear transfer through the link flanges, giving a somewhat high estimation of the stress state in the link flanges near the connection.

Non-linear material properties and large displacement effects were considered in the analyses. Material plasticity was based on a von Mises yield surface and an associated flow rule. Plastic hardening was defined using a nonlinear kinematic hardening law. Data from cyclic coupon testing of A572 Gr. 50 steel [37] (similar to A992 steel) was used to calibrate the material parameters. The same material properties were used for the beam, link, and column. Large displacement effects were accounted for by utilizing the nonlinear geometry option in ABAQUS. Yielding in the web at low rotations introduces sufficient asymmetry to trigger inelastic buckling at larger rotations, without having initial imperfections specified at the beginning. Other studies utilizing these modeling methods have achieved good prediction of inelastic local buckling and associated strength degradation [33,34].

2.3. Low Cycle Fatigue Failure Index

Recent analytical studies of steel frame components have used a low cycle fatigue failure index based on a stress modified critical strain criterion. The failure index is computed as the accumulated equivalent plastic strain (PEEQ in ABAQUS) divided by a critical plastic strain.

$$\text{Failure Index} = \frac{\text{PEEQ}}{\varepsilon_{p,critical}} \qquad (2\text{-}4)$$

20

Accumulated equivalent plastic strain is defined using the plastic strain rate tensor, $\dot{\varepsilon}_{ij}^{P}$, as:

$$\text{PEEQ} = \int_{0}^{t} \sqrt{\frac{2}{3} \dot{\varepsilon}_{ij}^{P} \dot{\varepsilon}_{ij}^{P}} \, dt \qquad (2\text{-}5)$$

The critical plastic strain is taken as [38]:

$$\varepsilon_{\text{p,critical}} = \alpha \ \exp\left(-1.5 \frac{\sigma_m}{\sigma_e}\right) \qquad (2\text{-}6)$$

where σ_m is the hydrostatic stress, σ_e is the von Mises stress, and α is a material constant. The ratio of the hydrostatic and von Mises stress is the stress triaxiality. Fracture initiation is predicted when the failure index exceeds 1.0 over a characteristic length, l^*, in the model. Fell et al. used the failure index to estimate ductile fracture initiation in tube braces subjected to repeated cyclic loads [39]; Richards and Prinz used the failure index to evaluate demands in steel moment frame connections subjected to dynamic earthquake loads [24]; and Chao et al. used the failure index to estimate locations for ductile fracture initiation in EBF link webs subjected to monotonic loading [40].

Two parameters α and l^* are required for the failure index. To calibrate α, the critical plastic strain obtained from finite element models is compared with the critical strain obtained from coupon testing [41]. For the control model, α was taken as 2.6 [42]. The calibration of the characteristic length, l^*, is more subjective, requiring interpretation of fractographic images taken of the coupon fracture surfaces [41].

The computational expense of cyclic loading prohibits mesh refinement down to the size of the characteristic length. Therefore, fracture initiation is predicted whenever the failure index reaches a value of 1.0 for any element. Other studies have obtained reasonable results using this approach [24,39]. The smallest element length used for the link models in this study was

3.175mm. For reference, the characteristic length, l^*, calibrated by Kanvinde and Deierlein [41] for A572 Grade 50 steel is 0.198mm.

The failure index described above has been shown to reasonably predict fracture initiation under monotonic loading, but is less accurate for cyclic loading. Kanvinde and Deierlein [19] showed on average, 10% agreement between the fracture criterion and monotonic coupon tests. When large variations in triaxial stress occurred (such is the case with reversed cyclic loading), the fracture criterion tended to be less accurate, consistently over-predicting failure index values and giving a somewhat conservative estimation of fracture initiation [19]. The level of conservancy under cyclic loading was not quantified in [19].

In this study, the failure index is not intended to predict exact rotation capacities for links, although the rotation when the failure index reaches 1.0 will be discussed. Rather, the failure index provides a tool for comparing various models.

2.4. Control Model Validation

To evaluate the modeling techniques used in this study, the control model was subjected to cyclic loading and results were compared with the full-scale test performed by Okazaki et al. [7] (specimen MWS). The comparison study considered system behavior as well as failure index values and fracture initiation in the link flanges. Findings from the comparison study are presented later in the results section.

2.5. Models to Investigate Reduced Web Sections

Nineteen additional models were analyzed, representing shear yielding links with reduced web sections. The same modeling techniques were used as described for the control model. The cross-section (nominal W18x40) and length (635mm) of the models matched those of the control

model. The nineteen link models will be considered as three groups, with each group designed to investigate specific aspects of link performance.

The first group consisted of six links designed to investigate the effects of various hole patterns, the amount of web removed, and the loading protocol. The response parameters were the link rotational stiffness, ultimate strength, and rotation when the failure index reached 1.0 (hereafter referred to as γ_1) at any location. Table 2-1 describes and illustrates each of the links in the first group and gives values for the response parameters. Results will be discussed in a following section.

The second group consisted of ten links that had the same hole pattern; the only variation for these models was the size of the holes in the web. The hole pattern is shown in Table 2-2, along with response values from the analyses. The reduced web sections, given as a percentage of the web cross-section removed, ranged from 6% to 24%.

The third group consisted of three links with different hole patterns, but the same percentage of web section removed. The patterns are shown in Table 2-3, along with response values from the analyses.

2.6. Models to Investigate Reduced Flange Sections

Fifteen models were analyzed, representing shear yielding links with reduced flange sections. The geometry of the flange section reductions are shown in Fig. 2-8, with cut dimension parameters *a*, *b*, and *c*. The cross-section (nominal W18x40) and length (635mm) of the flange reduction models matched those of the control model. The fifteen models will be considered as three groups, each designed to investigate specific aspects of link performance.

23
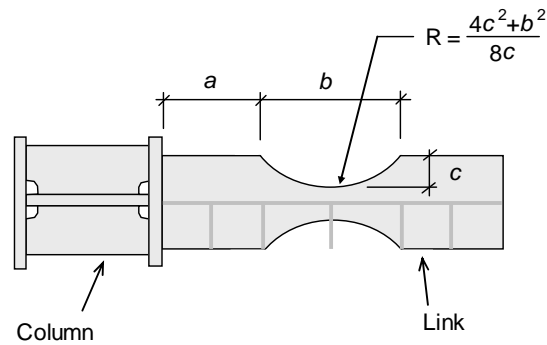
Fig. 2-8 Reduced flange section geometry

The first group consisted of seven links designed to investigate how the amount of flange removed affects link performance. The seven links had the same cut length (*b*) and distance from the column (*a*), but different cut depths (*c*). The response parameters were the link rotational stiffness, ultimate strength, and rotation when the failure index reached 1.0 (hereafter referred to as γ_1) at any location. The amount of flange area removed varied from 0% to 70%. Table 2-4 describes and illustrates each of the links in the first group and gives values for the response parameters. Results will be discussed later in the Results section.

The second group consisted of four links designed to investigate the effect of cut location on link performance. All four links had the same amount of area removed and cut length (*b*), but different spacing from the column (*a*). The varying cut distances (measured from the face of the column) are shown in Table 2-5, along with response values from the analyses.

The third group consisted of four links designed to investigate the effect cut length has on link performance. All four links in the third group had the same amount of flange area removed and spacing from the column (*a*), but different cut length (*b*). The group three models are shown in Table 2-6, along with response values from the analyses.

24

2.7. Cyclic Loading Protocols

   With the exception of model N1a in the first group of reduced web section models, the loading protocol described in the 2005 Seismic Provisions [25] was used exclusively in all analyses. The control model (N1a) was analyzed under the protocol given in the 2002 AISC seismic provisions [29], which facilitated direct comparison between the control model and the experimental test. The protocol described in the 2005 Seismic Provisions [25] was used for the other models to provide results that can be better compared with design rotations. Fig. 2-9 shows the two loading protocols used. Both cyclic loading protocols are in terms of the link rotation angle, γ.

(a)

(b)
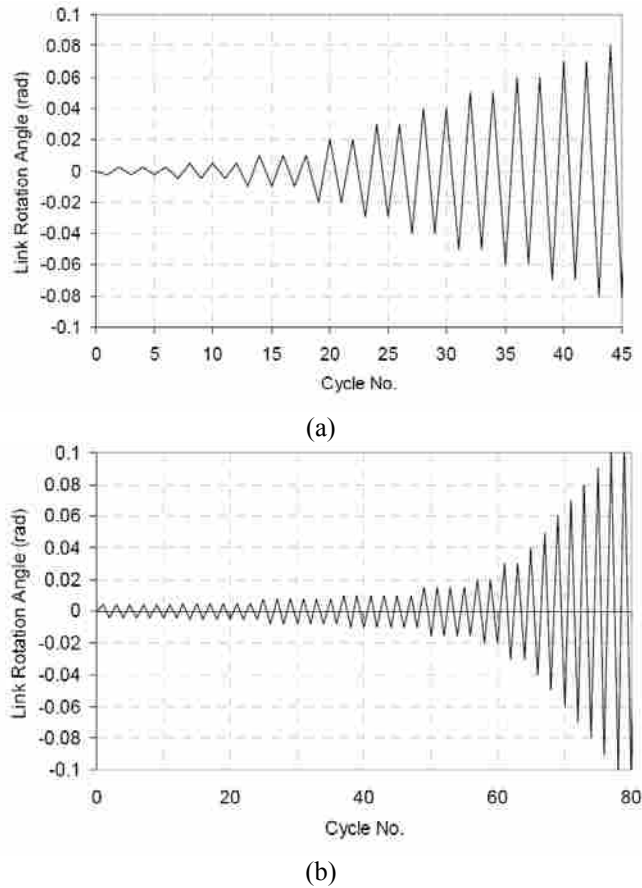
Fig. 2-9 Cyclic loading protocols used: (a) AISC 2002 [29]; and, (b) AISC 2005 [25]

2.8. Mesh Refinement

A mesh refinement study was performed to determine the appropriate level of mesh refinement for regions with the highest potential for low cycle fatigue. Links in the mesh refinement study were monotonically loaded up to 0.1 rad of rotation. Fig. 2-10 shows the incremental change in plastic strain as a function of decreasing mesh size. Because there is a rather steep strain gradient at the edge of the web holes, decreasing the size of the mesh continued to improve the accuracy of strain results (as noticed by continual changes in plastic strain, see Fig. 2-10). A typical mesh of the link and column is shown in Fig. 2-11. A typical mesh of the flange reduction region is shown in Fig. 2-12.
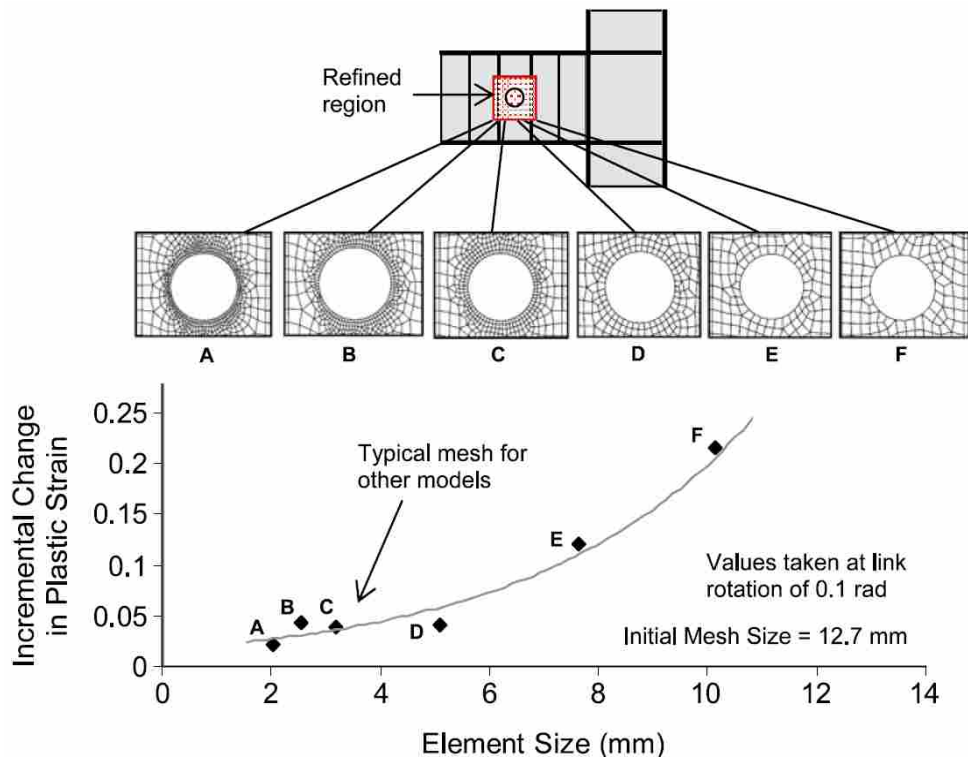
Fig. 2-10 Element size vs. change in strain relationship near web hole
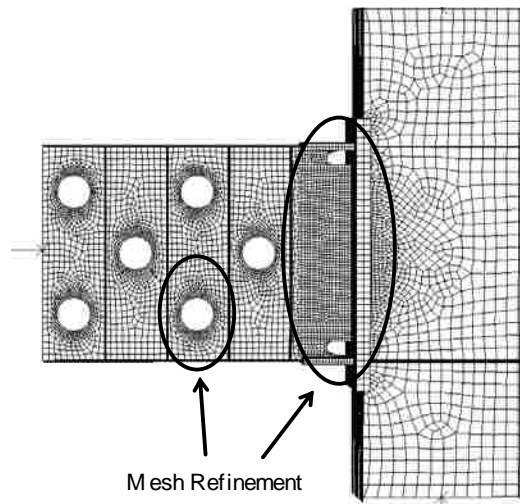
Fig. 2-11 Typical mesh of link and column region
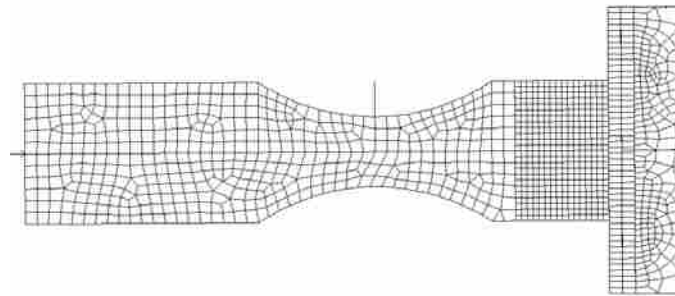
Fig. 2-12 Typical mesh of flange cut region

2.9. Results

2.9.1. Validation of Control Model

Hysteretic plots of force vs. link rotation for both the control model and prototype experiment are shown in Fig. 2-13.   From the plots, similar elastic and plastic behavior is observed.   Both the model and experiment sustained loads near 1112kN (250 kips) at 0.06 rad, and showed similar inelastic strength gain.

27

Failure index values from the control link model were compared with experimental results. Stress and strain data from the control model were used to compute the failure index in the link flange near the connection. The equivalent plastic strain, which contributes heavily to the failure index, is shown at a rotation of 0.05 rad in Fig. 2-14. It is important to note that while the link-web experiences the largest plastic strains, the triaxial stress in the web is lower than that of the flange, making the flange the critical region for ultra low cycle fatigue. Fig. 2-15 shows a plot of the failure index values obtained from the center of the top flange near the flange-to-column connection. For the control model, γ_1 was 0.04 rad. Compared to the experiment which experienced flange fracture after the 0.05 rad cycles [7], the result is somewhat conservative. This was expected, based on the limitations of the failure index and the modeling assumptions related to the bolted erector plate.
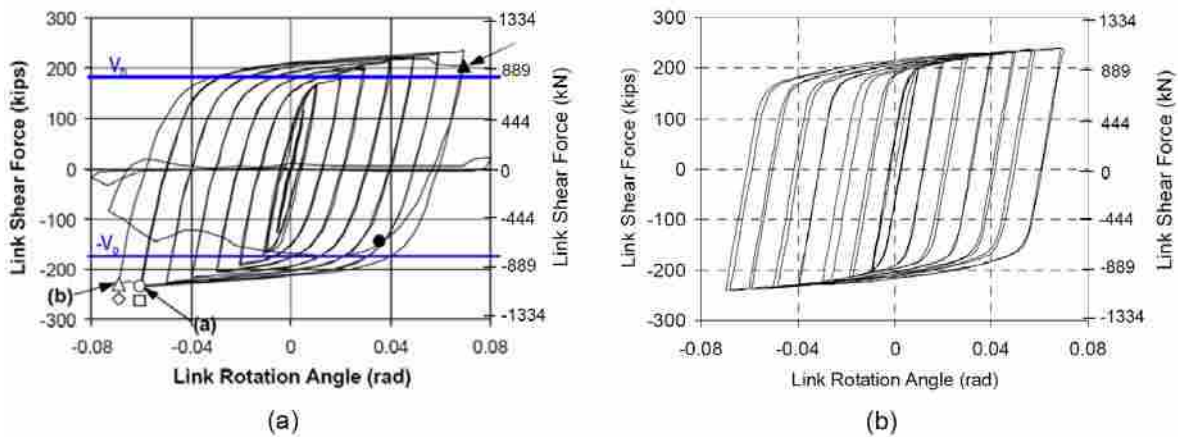
Fig. 2-13 Link shear vs. link rotation for: (a) test [13]; and, (b) ABAQUS model
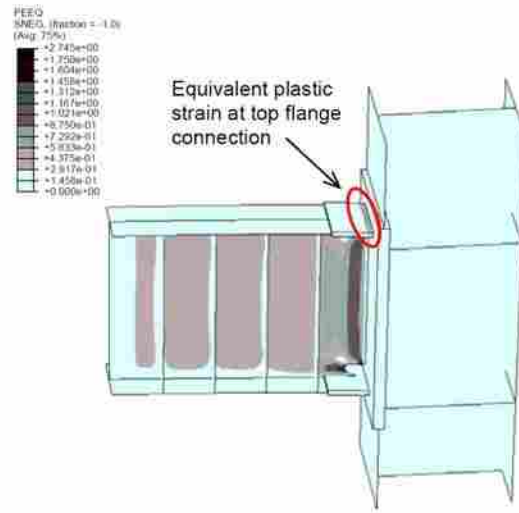
Fig. 2-14 Equivalent plastic strain contours
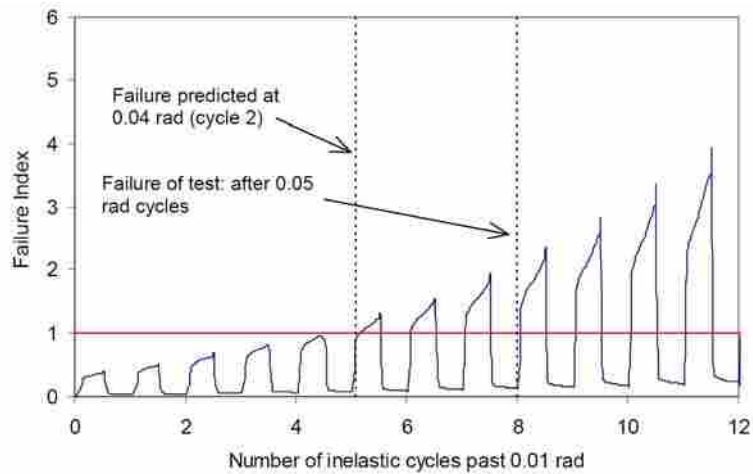
Fig. 2-15 Failure index values

2.9.2. Models with Reduced Web Sections

2.9.2.1. Effect of Web Removal on Link Performance

Table 2-1 lists results from the first group of models with web reductions. Included in the results are: the elastic stiffness of the link, maximum link strength, and link rotation when the

failure index reaches 1, γ_1. The elastic stiffness and maximum link strength are presented as a percentage of the control link.

Adding holes to the link web had little effect on web buckling. For all models in the first group, significant buckling of the link web did not occur at rotations less 0.08 rad. This is consistent with experimental testing of links that satisfy current stiffener requirements. The largest γ_1 for any model in the first group was 0.05 rad.

When holes are introduced into the link web, the stresses and strains increase in the web near the holes, but decrease in the link flanges near the connection. Fig. 2-16 shows the distribution of plastic strain in the link web when holes are introduced. Fig. 2-17 shows that when a web section is removed, the triaxial stress in the link flange decreases slightly [Fig. 2-17 (a)] and the plastic strains in the flange drop significantly [Fig. 2-17 (b)].

The models indicate that adding holes to the link web will not increase γ_1 because of large failure index values around the edges of the holes. Comparing the γ_1 of models without web reductions and models with 15% web reductions (compare models N1b and N3b in Table 2-1), γ_1 for the 15% web section reduction was lower due to higher failure index values in the web. For model N1b, γ_1 was 0.05 rad, with the critical element being in the flange. For model N3b, γ_1 was 0.04 rad, with the critical element being in the web.

Removing more material from the web resulted in a lower γ_1. Comparing models N2b and N3b, the web section reduction of 30% in model N2b resulted in a γ_1 of 0.03 rad, as compared to model N3b with a 15% web reduction which experienced a critical failure index during the first cycle to 0.04 rad. The relationship between the amount of web removed and γ_1 was explored further in the second group of models.
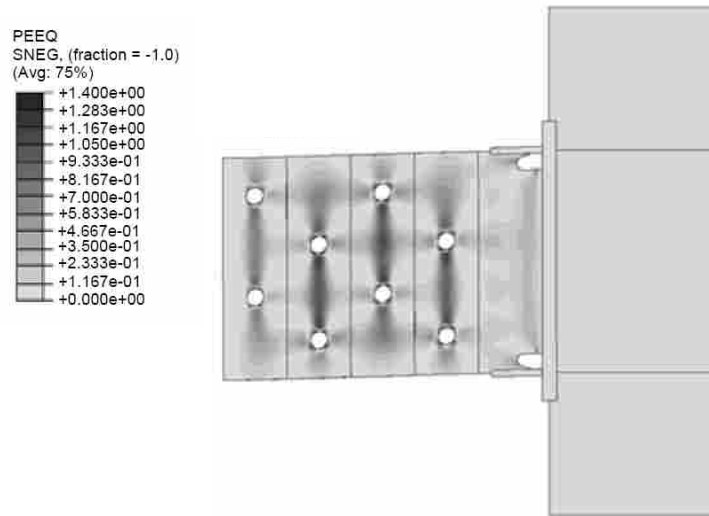
Fig. 2-16 Plastic strain contours in link web with area reductions (model N3b, 15% web removal, 0.04 rad rotation)

(a)

(b)
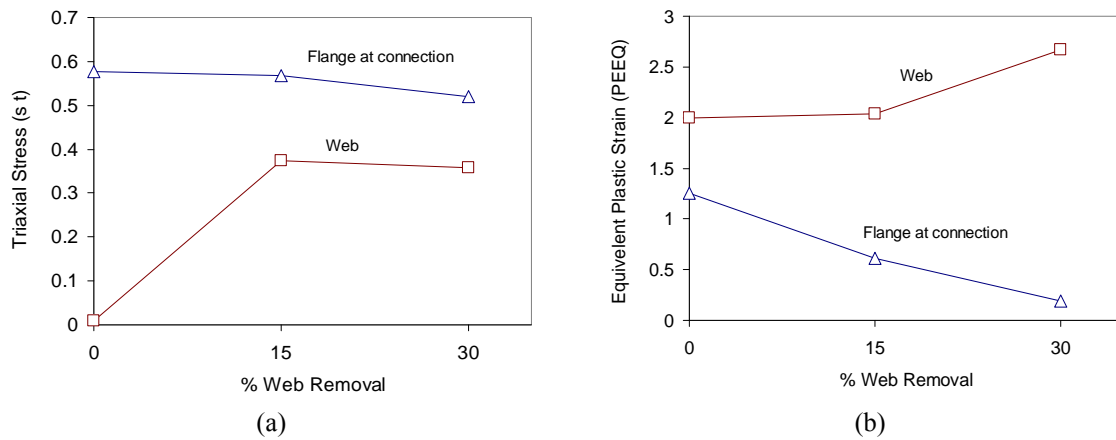
Fig. 2-17 (a) Triaxial stress; and, (b) equivalent plastic strain at 0.05 rad rotation vs. percent web removal for models N1b (0% web removal), N2b (15% web removal), and N3b (30% web removal)

Table 2-1: Description of RWS Group 1 Link Models and Summary of Results

Model Designation	Loading Protocol	Web Holes	% Reduction in web section area	Sketch	Elastic Stiffness (% of control)	Rotation when Failure Index Reached 1, γ_1 (rad)	Strength when Failure Index Reached 1 (% of control)	Location where index = 1
N1a [a]	2002 AISC	No web holes provided; "control" model	0		100	0.04 (2[b])	100	Top link flange near column connection
N1b	2005 AISC	No web holes provided	0		100	0.05 (1)	103.9	Top link flange near column connection
N2b	2005 AISC	Two holes at reduced sections. Rows of holes at 45 degrees.	30		89.7	0.03 (2)	80.2	At edge of web reduction
N3b	2005 AISC	Two holes at reduced sections. Rows of holes at 38 degrees.	15		96.3	0.04 (1)	90.3	At edge of web reduction
N4b	2005 AISC	Two holes at reduced sections. Rows of holes at 38 degrees.	30		87.5	0.03 (1)	69.7	At edge of web reduction
N5b	2005 AISC	Two holes at reduced sections. Rows of holes at 30 degrees.	15		96.3	0.03 (2)	91.8	At edge of web reduction

[a] Control model
[b] Failure index reached 1 during the second cycle at 0.04 rad

2.9.2.2. Influence of Hole Size on γ_1

Larger holes resulted in smaller values of γ_1. Table 2-2 shows the amount of web area removed and the resulting γ_1 for each model in the second group. As the area of the web holes increased, γ_1 decreased. The largest γ_1 was 0.04 rad at web reductions ranging from 6 to 12%. Links with no web section reductions in the first group also achieved a γ_1 of 0.04 rad (beginning of first cycle to 0.05 rad, see Table 2-1).

2.9.2.3. Influence of Hole Spacing on Web Strain Concentrations and γ_1

Closely spaced holes caused increased strains and lower values of γ_1. When holes were spaced closely together, strain concentrations from one hole overlapped with and compounded the strain concentrations from other holes. Hole spacing refers to the shortest distance between two adjacent hole centers (including adjacent holes separated by stiffeners). Table 2-3 shows the γ_1 values for each of the three link models in the third group, all having 15% web section reductions but different hole spacing. Model HLS3, which had two holes in each panel and the largest hole spacing, achieved a γ_1 of 0.03 rad. Models HLS1 and HLS2 (see Table 2-3) which had single hole patterns and closer hole spacing, achieved a γ_1 of 0.02 rad.

2.9.2.4. Expected Link Rotation for Experimental Testing

Due limitations of the failure index, conservatism with some of the modeling techniques, and the fact that fracture initiation may not instantaneously preclude unstable fracture propagation, link rotations from experimentation are expected to exceed the γ_1 values from this study. Based on the difference observed between the experimental test and the control model, link rotations from experimental testing might be expected to be on the order of 0.01 rad greater than the γ_1 achieved by the models in this study (Table 2-1). The largest γ_1 achieved for any

33

model with web section reductions was 0.04 rad (see model N1b in Table 2-1). This is lower than the 0.08 rad hoped for with shear yielding links.

Table 2-2: Description of RWS Group 2 Link Models and Summary of Results

Model Designation	% Reduction in web section area	Sketch	Rotation when Failure Index Reached 1, γ_1 (rad)
L1	6		0.04 (1[a])
L2	8		0.04 (1)
L3	10		0.04 (1)
L4	12		0.04 (1)
L5	14		0.03 (2)
L6	16		0.03 (2)
L7	18		0.03 (1)
L8	20		0.03 (2)
L9	22		0.03 (1)
L10	24		0.03 (1)

[a] Failure index reached 1 during the first cycle at 0.04 rad

Table 2-3: Description of RWS Group 3 Link Models and Summary of Results

Model Designation	Web Holes	% Reduction in web section area	Sketch	Rotation when Failure Index Reached 1, γ_1 (rad)
HLS 1	Semi-circular holes at top and bottom of link web	15		0.02 (1[a])
HLS 2	Holes in middle of link web	15		0.02 (1)
HLS 3	Two holes organized in two horizontal lines	15		0.03 (2)

[a] Failure index reached 1 during the first cycle to 0.02 rad

34
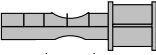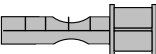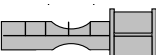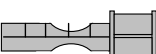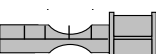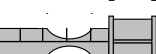
2.9.3. Models with Reduced Flange Sections

2.9.3.1. Effect of Flange Removal on Link Performance

Table 2-4 lists results from the first group of models with flange reductions. Included in the results are: the elastic stiffness of the link, maximum link strength, and link rotation when the failure index reaches 1, γ_1. The elastic stiffness and maximum link strength are presented as a percentage of model A0 having no flange reductions.

Removing area from the link flange had little effect on link stiffness, strength, or rotation capacity. Link A6, having the largest reduction in flange area (70%), saw only one additional radian of link rotation over link A0 which had no flange area reduction. Decreasing the link flange area had a minimal effect on link stiffness (reducing the elastic stiffness by only 1.1% with a 70% area reduction) and a negligible effect on link strength (the maximum link strength increased by only 2.5% with 70% flange removal).

Table 2-4 Description of RFS Group 1 Link Models and Summary of Results

Model Designation	% Reduction in flange section area	Cut Dimensions			Sketch	Elastic stiffness (% of A0)	Rotation when failure index reached 1, γ_1 [rad]	Strength when failure index reached 1 (% of A0)
		a [in.]	b [in.]	c [in.]				
A0	0	--	--	--		100	0.05 (1[a])[b]	100
A1	20	6	10	0.60		99.8	0.05 (1)[b]	99.6
A2	30	6	10	0.90		99.7	0.05 (1)[b]	99.6
A3	40	6	10	1.20		99.6	0.05 (1)[b]	99.3
A4	50	6	10	1.51		99.4	0.05 (1)[b]	99.2
A5	60	6	10	1.81		99.2	0.06 (1)[b]	102.8
A6	70	6	10	2.11		98.9	0.06 (1)[b]	102.5

[a] Failure index reached 1 during the first cycle at 0.05 rad.

[b] Failure index reached 1 in the top link flange near the column connection.

All seven links in the first group of flange reduction models exceeded the critical failure index in the link top flange at the column connection. Fig. 2-18(a) and Fig. 2-18(b), show the plastic strain and triaxial stress values in the web, connection, and flange cut regions. In Fig. 2-18(a), the web and connection regions experience similar amounts of plastic strain; however, in Fig. 2-18(b) the triaxial stress in the web is much lower than that at the connection, leading to a lower failure index value in the web and higher failure index value at the flange connection. The plastic strain at the connection was small, and remained relatively constant over the entire range of flange area reductions (decreasing only 10% with a flange area reduction of 70%).
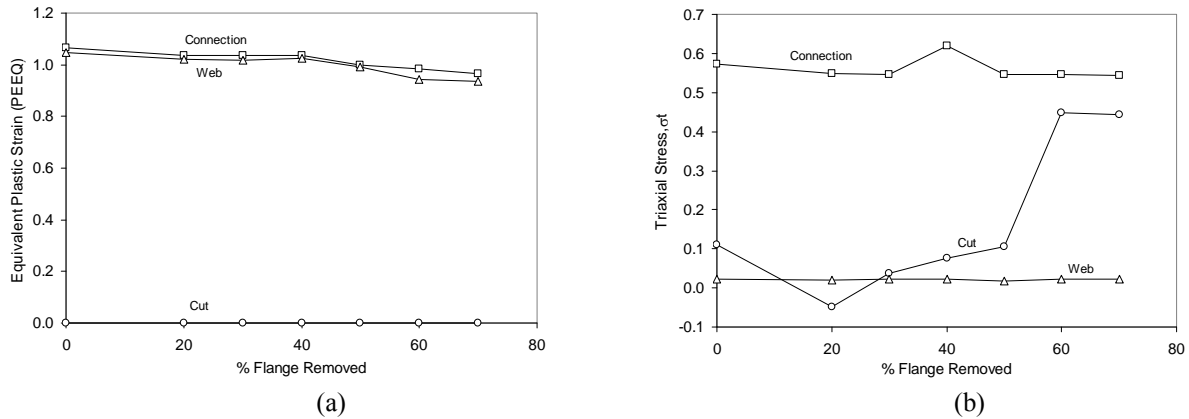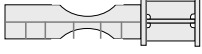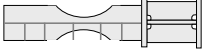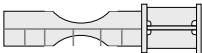
Fig. 2-18 (a) Equivalent plastic strain; and, (b) triaxial stress at 0.05 rad rotation vs. percent web removal for models A0 (0% web removal)-A6 (70% web removal)

2.9.3.2. Influence of Flange Removal Location and Flange Removal Length on γ_1

The flange cut location along the length of the link had no effect on γ_1. Table 2-5 shows flange cut locations and corresponding values of γ_1 for the second group of models with flange area reductions. In Table 2-5, γ_1 remained constant for all four variations in cut location.

Similar to flange reduction location, the length of the flange cut had no effect on γ_1. Table 2-6 shows no change in γ_1 as the length of flange cut is changed from 5 in. (20% of the link length) to 12.5 in. (50% of the link length).

36
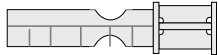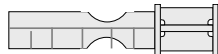
Table 2-5: Description of RFS Group 2 Link Models and Summary of Results

| Model Designation | Cut Dimensions | | | Sketch | Rotation when failure index reached 1, γ_1 [rad] |
	a [in.]	b [in.]	c [in.]		
D1	5	9	1.51		0.05 (1[a])[b]
D2	6.25	9	1.51		0.05 (1)[b]
D3	7.5	9	1.51		0.05 (1)[b]
D4	8.75	9	1.51		0.05 (1)[b]

[a] Failure index reached 1 during the first cycle at 0.05 rad.

[b] Failure index reached 1 in the top link flange near the column connection.

Table 2-6: Description of RFS Group 3 Link Models and Summary of Results

| Model Designation | Cut Dimensions | | | Sketch | Rotation when failure index reached 1, γ_1 [rad] |
	a [in.]	b [in.]	c [in.]		
L1	5	5	1.51		0.05 (1[a])[b]
L2	5	7.5	1.51		0.05 (1)[b]
L3	5	10	1.51		0.05 (1)[b]
L4	5	12.5	1.51		0.05 (1)[b]

2.9.3.3. Discussion of the Findings by Berman et. al

A recent study by Berman et al. [43] also investigated the effects of reduced flange sections on EBF link-to-column connection performance. In [43] link flange cuts were used at each end of the link, similar to RBS cuts in moment frame beams (see Fig. 2-19). All link geometry was modeled using shell elements in MSC Marc Mentat 2005r3 [44], and each link was loaded using the cyclic loading protocols outlined in the 2005 AISC Seismic Provisions [25] (similar to the links in this study). The boundary conditions used in analysis assumed no link end rotation or axial load (see Fig. 2-19 for further description of the boundary conditions used by [43]).
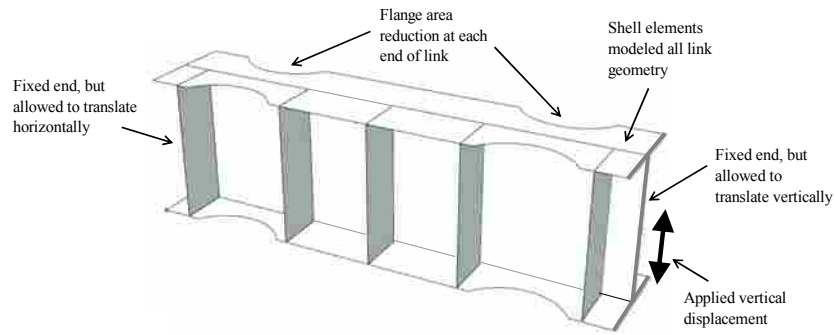
Fig. 2-19 Flange reductions and boundary conditions for Berman et al. links

The findings by Berman et al. are different from those presented earlier in this chapter for EBF links with reduced flange sections.   Berman et al. indicated plastic strain reductions near 60-80% at the end of the link with 50-60% area removed from the flanges, suggesting flange removal as a viable option for reducing EBF link-to-column connection demands. In the RFS study in this chapter, there was very little change in plastic strain at the end of the link, for area reductions ranging between 20-70% (see Fig. 2-18(a) from earlier discussion).

In order to investigate the difference in results, a model analyzed by Berman et al. was recreated and compared with the models in this study. The recreated model corresponded to the Case 2 model in [43]. The following paragraph discusses the findings from the Berman et al. comparison.

The difference between the results presented in this chapter and those of Berman et al. can be explained by stiffener spacing and consideration of the weld access holes. The links analyzed by Berman et al. neglected web stiffeners within the reduced flange region, while the links analyzed in this study did not. The links analyzed by Berman et al. neglected the weld access hole at the end connection, while the links analyzed in this chapter did not. The larger stiffener spacing near the flange reduction in the Berman et al. model increased the out-of-plane web deformations within the flange reduction region and allowed for collapse of the link flanges,

38

increasing the flange strains. Also, the weld access hole geometry for the links analyzed in this chapter, reduced the link shear strength in the first panel and concentrated the link deformations near the connection, away from the reduced flange section (see Fig. 2-20(a)). Neglecting the weld access holes and web stiffeners in the Berman et al. model allowed link deformations to begin near the reduced flange region, increasing the flange strains near the flange reductions, and decreasing flange strains near the connection (see Fig. 2-20(b)).
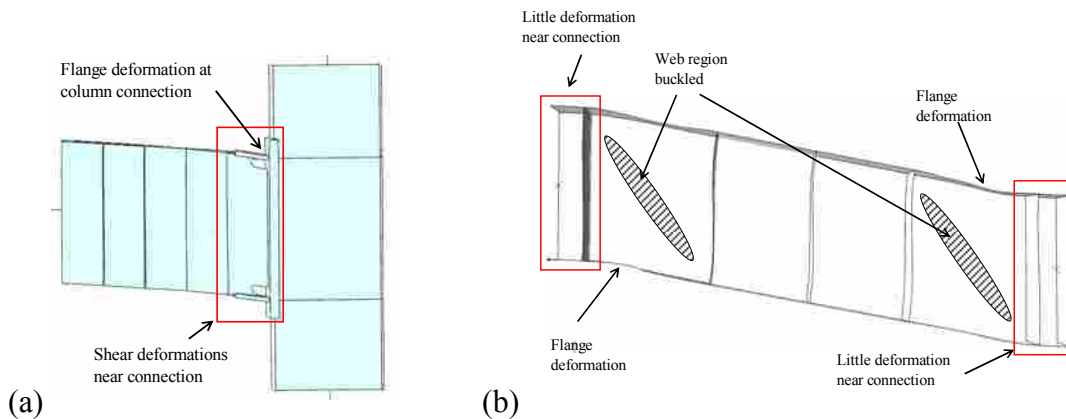
Fig. 2-20 Deformed link shape scaled 3x for (a) model A6 from group 1 models and (b) Berman et al. Case 2 model (deformations taken at 0.09 rad of rotation)

2.10. Summary and Conclusions

In this chapter, the cyclic behavior of EBF links with reduced web sections and reduced flange sections was investigated using nonlinear finite element analysis. Finite element models were developed to simulate typical experimental testing of EBF links. Validation of modeling techniques was performed using existing experimental data. Low-cycle material fatigue was estimated using a failure index.

The following conclusions regarding EBF links with reduced web and flange sections are based on the cyclic analysis of twenty-four W18x40 links with link-to-column connections, circular flange cuts, and circular holes in the web.

39

Computer Models Indicate:

1. Putting holes in the link web reduces plastic strains in the link flanges near the connection.

2. Putting holes in the link web increases plastic strains and stress triaxiality in the web, prior to web buckling, at the edges of the holes.

3. The stress-strain state at the edge of the web holes is worse than at the flanges when no holes are added. This suggests that links with web holes will have a different failure mode and lower/similar rotation capacity to links without web holes.

4. Removing area from the link flanges has little effect on γ_1 and strains at the flange-to-column connections.

5. The flange area reduction location and length of flange cut have no effect on γ_1.

Chapter 3: DESIGN CONSIDERATIONS AND SEISMIC PERFORMANCE OF BUCKLING-RESTRAINED BRACED FRAMES IN ECCENTRIC CONFIGURATIONS

While the previous chapter focused on improvement methods for existing EBF configurations, the objective for this chapter is to investigate the feasibility of using BRBFs in eccentric configurations, as an alternative to the EBF. The chapter begins in the introduction by discussing some negative aspects of EBF design and performance, followed by an introduction to the concept of BRBFs in eccentric configurations (hereafter referred to as BRBF-Es). Next, design considerations for the BRBF-Es are developed and compared to those of typical EBFs. Then, the static and dynamic performance of several BRBF-Es and EBFs having equal strength are compared. Following the comparison study, a BRBF-E design example is presented, and lastly, conclusions regarding the performance and design of BRBF-Es are summarized.

3.1. Introduction

Eccentrically braced frames (EBFs) are sometimes chosen for seismic design specifically because EBF configurations can accommodate architectural openings [45]; however, even though EBFs have architectural benefits, it is challenging to produce economical designs that will perform well. In EBF design, engineers must balance frame performance with practical design, both of which depend on beam size. Because EBF beams are expected to yield during frame overloading, good performance requires beam sizes to vary between floors so that drifts

are not concentrated [46]. Unique beam sizes at each floor result in unique connection details, so good performance in EBFs comes at a cost.

Another difficulty with EBFs is the poor experimental performance of link-to-column connections, as highlighted in Chapter 2. The poor link-to-column performance in EBFs has lead the current AISC Seismic Provisions [25] to require experimental verification of all link-to-column connections, affecting design costs, and limiting the number of practical EBF configurations. As demonstrated in Chapter 2, improving EBF link-to-column connection performance is difficult.

BRBFs with braces in eccentric configurations (BRBF-Es) may combine the architectural benefits of EBFs with the design benefits of BRBFs. BRBF-Es could accommodate architectural features using brace eccentricities similar to EBFs, and dissipate seismic forces through axial yielding of a buckling-restrained brace, similar to concentric BRBFs (BRBF-Cs).

Methods used to improve BRBF-C performance may also help improve BRBF-E performance. As mentioned in Chapter 1, recent studies indicate using beam splices may help reduce forces and moments that develop in BRBF-C beams and gusset connections [6,17,18]. A full-scale four-story frame having buckling-restrained braces tested by Fahnestock et al. [17] sustained frame drifts near 0.05 rad with little damage to the beams columns or gussets. The frame used beam splices outside the gussets with structural T's joining the beam sections at the web. In different testing by Coy [6], frame connections achieved rotations greater than 0.06 rad with minimal damage using a beam splice with flange connector plates. Incorporating the ductile beam splices into BRBF-E configurations may limit frame damage by reducing beam moments at large deformations. Fig. 3-1 shows typical EBFs and two proposed BRBF-Es with beam splices, in their initial and deformed configurations.
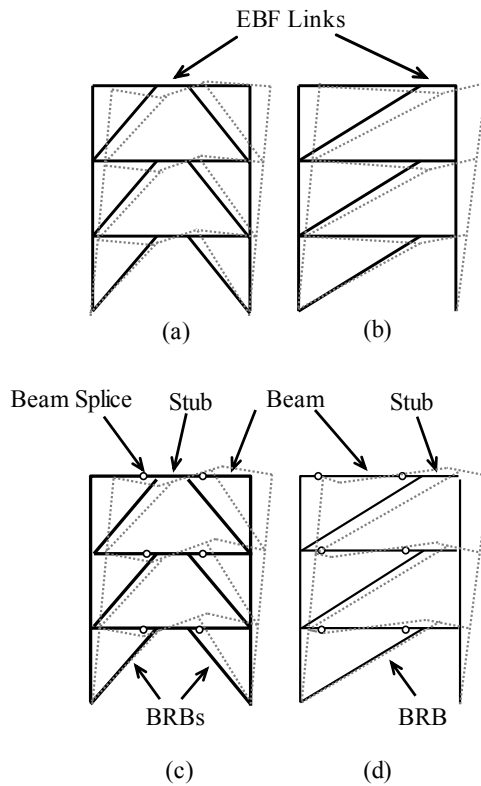
Fig. 3-1 Initial and deformed configurations for (a-b) EBFs and (c-d) BRBF-Es

3.2. Design Considerations

There are four members to consider when designing BRBF-Es: the brace, stub, beam, and columns. In BRBF-Es, the braces provide lateral frame stiffness and are designed to undergo large inelastic axial deformations. For the stub-to-column configuration shown in Fig. 3-1(d), the BRBF-E stubs act as cantilevered beams and are designed to remain elastic while transferring ultimate brace forces into the columns; separate from the stub, the BRBF-E beam (see Fig. 3-1(d)) acts as a simply-supported beam, and is designed to carry axial and flexural loads from the earthquake and gravity loads. For the mid-span configuration in Fig. 3-1(c), the beam is cantilevered while the stub is simply-supported. BRBF-E columns are designed to transfer the stub shear force and bending moment into the foundation.

The goal in designing BRBF-Es is to isolate yielding and damage within the buckling-restrained brace. This can be achieved using a capacity based design method where the braces are designed first based on seismic demand, and then the beam, stub, and columns are designed based on ultimate brace forces. In order to isolate yielding within the braces, the forces generated from a fully strain-hardened brace must be understood.

3.2.1. Ductile-Member Forces

3.2.1.1. Brace Force in BRBF-Es with Stub-to-Column Connections

Fig. 3-2(a) shows a typical BRBF-E with stub-to-column configuration (similar to EBF link-to-column configuration), with an applied lateral load V. In Fig. 3-2(a), if the brace-end moments are neglected, the brace force can be determined easily using force equilibrium alone (see free-body diagram in Fig. 3-2(b)). The resulting brace force provided in Equation 3-1 is similar to that of typical BRBF-Cs with diagonal bracing, with the added term $\left(1 - \dfrac{e}{L}\right)$ accounting for the axial force taken by the stub.
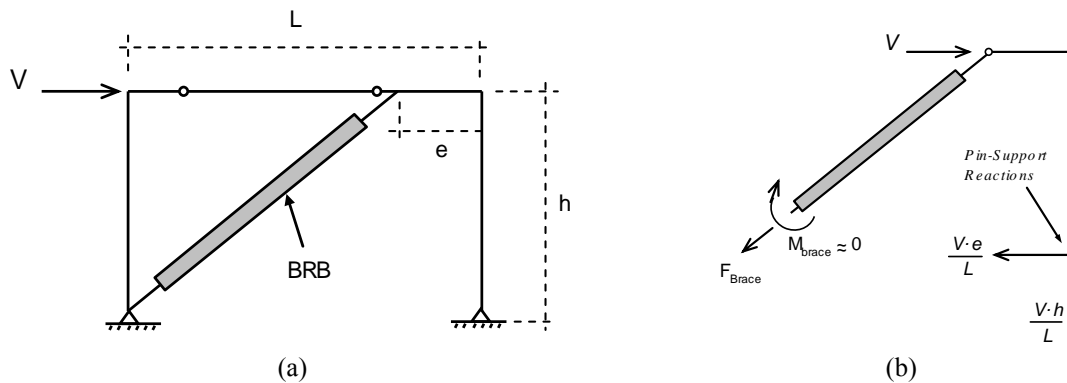
Fig. 3-2 (a) Generic BRBF-E with applied lateral load V; and, (b) free-body diagram of BRBF-E with reaction forces solved

$$F_{BRACE} = V \cdot \left(1 - \frac{e}{L}\right) \frac{\sqrt{(L-e)^2 + h^2}}{(L-e)}$$ (3-1)

44

Determining EBF member forces is more difficult than BRBF-E member forces. EBFs in link-to-column configurations are statically indeterminate, even when the brace-end moment and link axial force are neglected. Alternative analysis methods, such as elastic analysis, are required to determine EBF member forces.

3.2.1.2. Brace Force in BRBF-Es with Mid-Span Links

Another possible BRBF-E configuration is shown in Fig. 3-3(a), with the stub located at the beam mid-span (similar to EBF mid-span configurations). To ensure beam stability under gravity loads (once the braces have yielded), only one splice is allowed on either side of the stub (see Fig. 3-3(a)). Similar to the stub-to-column configuration, neglecting brace end moments allows for easy determination of the brace force using equilibrium. Fig. 3-3(b) shows a typical free-body diagram of one brace exploiting symmetry and Equation 3-2 presents the resulting axial force in the brace.

(a)   (b)
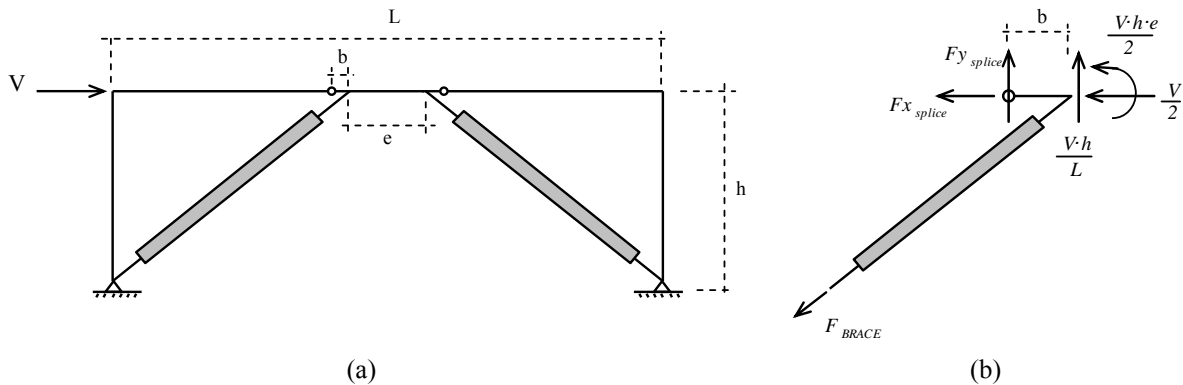
Fig. 3-3 (a) Generic BRBF-E with applied lateral load V; and, (b) free-body diagram of one BRBF-E brace

$$F_{BRACE} = \left(\frac{V}{L}\right) \cdot \left(1 + \frac{e}{2 \cdot b}\right) \sqrt{\left(\frac{L-e}{2}\right)^2 + h^2} \qquad (3\text{-}2)$$

3.2.2 Link and Beam Design

Determining the design forces in BRBF-E beams is more straightforward than in EBF beams. Fig. 3-4 compares the beam moment distribution in BRBF-E and EBF configurations. It can be seen in Fig. 3-4(a) that the beam splices in the BRBF-Es allow the stub to act as a cantilevered beam, simplifying the beam moment distribution and allowing for simplified force calculations. For BRBF-Es in mid-span configurations, the beams are essentially cantilevered while the stub is simply-supported between the two beam splices (see Fig. 3-4(c)). In EBFs, the continuous beam allows for significant moment to develop at the brace connection, complicating the beam moment distribution and making determination of beam forces more difficult (see Fig. 3-4(b) and Fig. 3-4(d)). Additionally, with the continuous EBF beams, it is difficult to prevent yielding in the beam outside the link, an issue that can lead to beam instability and loss of strength and ductility [10].

Equation 3-3 and Equation 3-4 represent the resulting stub design shear force and bending moment for the BRBF-E stub-to-column configuration. Equation 3-5 and Equation 3-6 represent the beam stub design shear force and bending moment for the mid-span stub configuration.

Stub Design Forces for Stub-to-Beam Configuration:

$$V_s = (\beta \cdot \omega \cdot R_y) \cdot \left(\frac{V \cdot h}{0.9 \cdot (L-e)} \right) \cdot \left(1 - \frac{e}{L} \right) \tag{3-3}$$

$$M_s = (\beta \cdot \omega \cdot R_y) \cdot \left(\frac{V \cdot h \cdot e}{0.9 \cdot (L-e)} \right) \cdot \left(1 - \frac{e}{L} \right) \tag{3-4}$$

Stub Design Forces for Mid-Span Configuration:

$$V_S = (\beta \cdot \omega \cdot R_y) \cdot \left(\frac{V \cdot h}{1.8 \cdot L} \right) \cdot \left(1 + \frac{e}{2 \cdot b} \right) \qquad (3\text{-}5)$$

$$M_S = (\beta \cdot \omega \cdot R_y) \cdot \left(\frac{V \cdot h \cdot b}{1.8 \cdot L} \right) \cdot \left(1 + \frac{e}{2 \cdot b} \right) \qquad (3\text{-}6)$$

For the BRBF-E stub shear force and bending moment provided in Equations 3-3 through 3-6, $(\beta \omega R_y)$, V, L_{br} are brace overstrength factors, story shear, and brace length respectively.

(a) BRBF-E with Stub-to-Column Connection   (b) EBF with Link-to-Column Connection

(c) BRBF-E with Mid-Span Stub

(d) EBF with Mid-Span Link
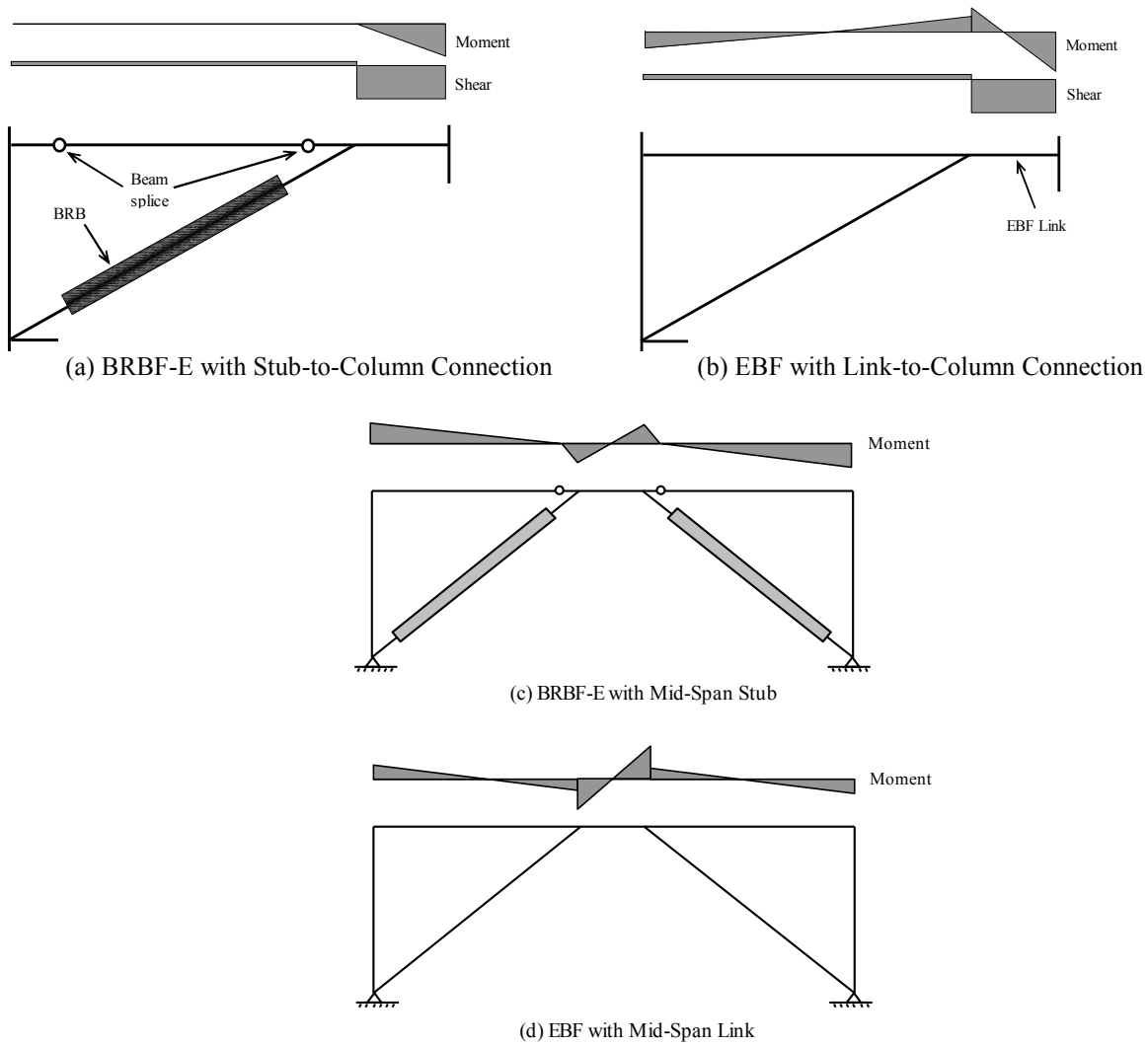
Fig. 3-4 Typical beam force distribution in BRBF-E and EBF configurations

Design of BRBF-E stubs allows for repetition of beam size throughout the building height. Following capacity based design principles, forces and moments for BRBF-E stubs are determined from ultimate brace capacities. Since brace capacities are determined from individual story shears, and since story shears typically decrease up the building height (ASCE Standard 7-05 [47]), stub designs from lower stories will typically satisfy the strength requirements of higher stories. This allows repeatability in BRBF-E stub sizes as well as consistency with brace geometries and connection details.

Unlike EBF links, stiffeners are not required for BRBF-E stub stability. Design of EBF links requires the addition of multiple web stiffeners to ensure stability under the expected large inelastic rotations [25,26,27]; BRBF-E stubs are expected to remain elastic and must only satisfy web and flange compactness requirements to prevent local buckling [25].

The BRBF-E beam splices allow for efficient use of beam material at each floor. The BRBF-E beam splices prevent moment transfer between the stubs and beams (see Fig. 3-4(a) and Fig. 3-4(c)), allowing the beam and stub to be designed separately based on their individual demands. In EBFs, beams are typically continuous and sized from the large seismic demand in the links.

3.2.3 BRBF-E Column Design

The columns of BRBF-Es must have adequate strength to withstand the forces generated from the fully strain-hardened braces. Columns in BRBF-Es with stub-to-column configurations (see Fig. 3-4(a)) must be able to withstand the maximum bending moments and axial forces transferred from the stub. Depending on the length of the stub and building height, these column demands can become quite large, considering that the ultimate capacity of a buckling-restrained brace is nearly twice that of its yield strength [48,49]. One advantage of using the BRBF-E mid-

span configuration (see Fig. 3-4(c)), is that the brace forces are transferred to the column without generating large column moments.

Determining ultimate column demands for BRBF-Es is less straightforward than for the beams. While the ultimate forces in BRBF-E beam stubs depend on individual brace capacities only, ultimate column demands depend on story moments, as well as cumulative axial forces from the stories above. Equation 3-7 represents the design column axial demand, based on capacity-based design, in which all ductile elements are assumed to reach their ultimate capacity simultaneously:

$$P_{COL_i} = (\alpha\beta\omega) \sum_i^{nstory} F_{br_i} \left(\frac{h_i}{L_{br_i}} \right) \quad i = 1, 2, ..., nstory \tag{3-7}$$

Recent research has shown that a capacity-based design approach is adequate for predicting axial column demands of low-rise BRBF-C buildings; however, for taller buildings, column demands using this approach are overly conservative [50]. Richards [50] showed that column demands in the lower stories of high-rise BRBF-Cs (9-stories and greater) were between 55-70% of those predicted using the capacity based design approach [50].

3.3. BRBF-E and EBF Performance Comparison

To investigate the relative seismic performance of BRBF-Es compared to typical EBFs, twelve EBF and twelve BRBF-E buildings were designed and analyzed. The twelve EBF and BRBF-E designs represented three building heights (3-, 6-, and 9-story), two bay widths (20 ft and 30 ft), and two strength levels (I=1 and I=1.5, ASCE Standard 7-05 [47]). Accidental torsion effects from potential eccentricities between the buildings center of mass and center of rigidity were considered in the design. EBF and BRBF-Es with link-to-column connections were used exclusively in the comparison study. Fig. 3-5 shows the 20 ft and 30 ft bay width EBF and

BRBF-E configurations for the 3-, 6-, and 9-story buildings. To directly compare EBF and BRBF-E performance, the EBF buildings were designed first, and then the BRBF-Es were designed to have equal story strength. Based on findings presented in [50], columns in the 9-story BRBF-E designs were sized based on demands that had been reduced by 30%. Member sizes for the twenty-four building designs are provided in Table 3-1 through Table 3-6.
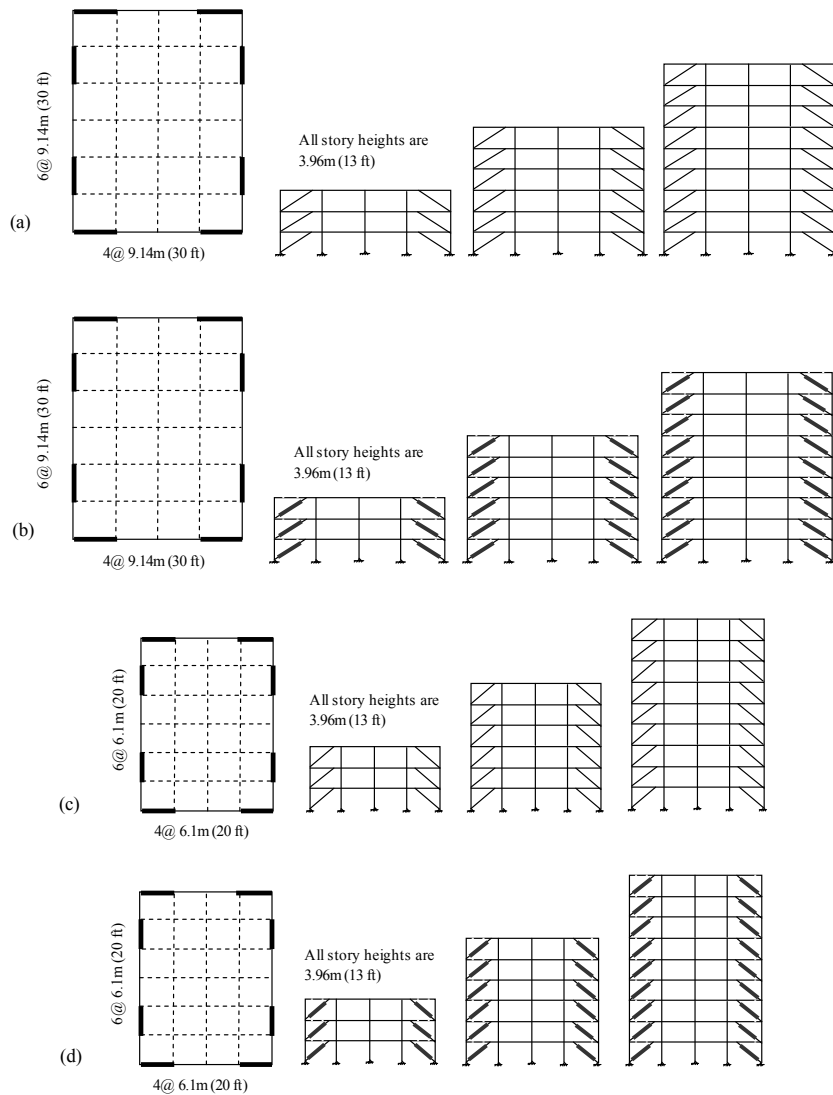
Fig. 3-5 3-, 6-, and 9-story frame configurations for (a) 30ft bay width EBF; (b) 30ft bay width BRBF-E; (c) 20ft bay width EBF; and (d) 20ft bay width BRBF-E

Table 3-1 3-Story EBF Member Sizes

| | Shape (U.S. designation) | | | |
| | Bay Width = 30ft | | Bay Width = 20ft | |
Member	I [f] =1	I=1.5	I=1	I=1.5
BM1[a,b]	W14x53	W18x65	W16x89	W24x94
BM2	W12x50	W14x74	W16x57	W21x68
BM3	W10x45	W12x50	W10x68	W14x68
BR1[c]	W12x79	W14x120	W14x145	W14x145
BR2	W12x79	W12x106	W12x96	W14x109
BR3	W12x79	W12x79	W12x72	W12x87
CL1-CL3[d]	W14x61	W14x53	W12x53	W14x68
CR1-CR3[e]	W14x120	W14x132	W12x120	W14x159

a. BM1 is beam at first story, BM2 is beam at second story…

b. All beam links are 4 ft long

c. BR1 is first story brace, BR2 is second story…

d. CL1 is first story left column, CL2 is second story…

e. CR1 is first story right column, CR2 is second story…

f. Occupancy importance factor (ASCE 7-05)

Table 3-2 6-Story EBF Member Sizes

| | Shape (U.S. designation)[a] | | | |
| | Bay Width = 30ft | | Bay Width = 20ft | |
Member	I=1	I=1.5	I=1	I=1.5
BM1	W14x82	W18x97	W21x73	W24x131
BM2	W14x68	W18x86	W21x62	W27x94
BM3	W14x68	W18x86	W16x89	W24x94
BM4	W12x50	W16x77	W16x77	W21x83
BM5	W10x45	W14x53	W14x68	W16x89
BM6	W10x45	W10x45	W10x68	W14x48
BR1[c]	W14x132	W14x159	W14x120	W14x176
BR2	W14x109	W14x159	W14x109	W14x145
BR3	W14x109	W14x159	W14x109	W14x145
BR4	W12x106	W14x132	W12x120	W14x145
BR5	W12x87	W14x109	W12x79	W12x120
BR6	W10x68	W12x87	W10x60	W12x58
CL1-CL2	W12x96	W14x120	W12x120	W14x176
CL3-CL4	W10x68	W14x74	W12x120	W12x120
CL5-CL6	W10x68	W12x45	W12x35	W12x45
CR1-CR2	W12x152	W14x193	W14x176	W14x257
CR3-CR4	W12x106	W14x145	W14x132	W14x211
CR5-CR6	W10x68	W12x96	W14x82	W12x120

a. See all notes from Table 3-1

Table 3-3 9-Story EBF Member Sizes

Member	Shape (U.S. designation)[a]			
	Bay Width = 30ft		Bay Width = 20ft	
	I=1	I=1.5	I=1	I=1.5
BM1	W16x77	W18x106	W24x76	W24x146
BM2	W14x82	W18x97	W21x73	W24x131
BM3	W14x82	W18x97	W21x73	W27x102
BM4	W14x74	W18x86	W21x68	W24x103
BM5	W14x68	W16x89	W16x89	W24x94
BM6	W14x53	W16x77	W16x77	W21x83
BM7	W12x50	W14x74	W14x74	W21x68
BM8	W10x45	W12x50	W12x50	W14x82
BM9	W10x45	W10x45	W10x45	W12x50
BR1[c]	W14x109	W14x176	W14x132	W14x193
BR2	W14x109	W14x176	W14x120	W14x176
BR3	W14x109	W14x159	W14x120	W14x159
BR4	W14x109	W14x159	W14x109	W14x159
BR5	W14x109	W14x145	W12x106	W14x145
BR6	W14x109	W14x132	W12x106	W14x132
BR7	W12x106	W14x109	W12x96	W14x109
BR8	W12x96	W12x106	W14x82	W12x106
BR9	W12x96	W12x87	W14x68	W12x72
CL1-CL3	W14x145	W14x211	W14x211	W14x311
CL4-CL6	W12x96	W14x109	W12x120	W14x159
CL7-CL9	W10x45	W12x45	W12x45	W14x68
CR1-CR3	W14x193	W14x283	W14x257	W14x398
CR4-CR6	W12x152	W14x176	W14x193	W14x257
CR7-CR9	W12x79	W12x106	W12x96	W14x132

a. See all notes from Table 3-1

Table 3-4 3-Story BRBF-E Member Sizes

Member	Shape (U.S. designation) or BRB Area (in^2)			
	Bay Width = 30ft		Bay Width = 20ft	
	I[e]=1	I=1.5	I=1	I=1.5
BM1-BM3[a,b]	W24x94	W24x162	W24x162	W24x229
BRB1[c]	6.77	11.10	8.17	12.00
BRB2	5.89	8.28	6.66	8.77
BRB3	4.52	5.35	4.3	5.39
C1-C3[d]	W21x147	W14x283	W14x311	W14x398

a. BM1 is beam at first story, BM2 is beam at second story…

b. All beam "links" are 4 ft long

c. BRB1 is first story brace area, BRB2 is second story…

d. C1 is first story column, C2 is second story…

e. Occupancy importance factor (ASCE 7-05)

Table 3-5 6-Story BRBF-E Member Sizes

	Shape (U.S. designation) or BRB Area (in^2) [a]			
	Bay Width = 30ft		Bay Width = 20ft	
Member	I=1	I=1.5	I=1	I=1.5
BM1-BM2	W24x131	W24x192	W24x192	W27x258
BM3-BM4	W24x117	W24x162	W24x162	W24x229
BM5-BM6	W24x68	W24x103	W21x122	W24x162
BR1	9.36	13.15	9.28	14.17
BR2	7.60	11.80	8.18	12.93
BR3	7.60	11.80	8.18	12.00
BR4	5.89	9.95	7.05	10.55
BR5	4.52	6.78	5.39	8.17
BR6	4.52	4.52	4.30	4.44
C1-C2	W14x283	W14x398	W14x426	W14x605
C3-C4	W14x211	W14x311	W14x311	W14x455
C5-C6	W14x120	W14x176	W14x193	W14x257

a. See all notes from Table 3-4

Table 3-6 9-Story BRBF-E Member Sizes

	Shape (U.S. designation) or BRB Area (in^2) [a]			
	Bay Width = 30ft		Bay Width = 20ft	
Member	I=1	I=1.5	I=1	I=1.5
BM1-BM3	W18x175	W24x192	W24x146	W24x207
BM4-BM6	W18x143	W24x163	W24x131	W24x176
BM7-BM9	W18x97	W24x117	W14x132	W24x131
BR1	9.95	14.47	10.26	15.10
BR2	9.36	13.15	9.28	14.17
BR3	9.36	13.15	9.28	13.55
BR4	8.28	11.80	8.77	12.82
BR5	7.60	11.52	8.17	12.00
BR6	6.78	9.95	7.05	10.55
BR7	5.35	8.28	5.87	8.77
BR8	4.52	5.89	4.18	6.64
BR9	4.52	4.52	3.21	4.18
C1-C3	W14x398	W14x500	W14x398	W14x550
C4-C6	W14x257	W14x370	W14x283	W14x398
C7-C9	W14x145	W14x211	W14x159	W14x233

a. See all notes from Table 3-4

3.4. Computer Modeling

3.4.1. Methods

The EBF and BRBF-E frames were modeled as 2-dimensional systems using the Open System for Earthquake Engineering Simulation (OpenSEES) [51] (see Appendix A for example OpenSEES source code). Nonlinear beam-column elements with inelastic fiber sections were used to model all beams and columns. The bases of the columns were considered fixed. Floor masses (see Fig. 3-6) were lumped into the column nodes at each story. Material behavior for all beams, columns, and EBF braces was modeled using a Giuffre-Menegotto-Pinto material model [52] with isotropic strain hardening and yield strength of 50 ksi (Steel02 with Fy=50 ksi in OpenSEES).

The buckling-restrained braces in the BRBF-E were modeled using truss elements which resist only axial forces and deformations. Although the cross-section of typical BRBs consists of a smaller steel core and larger end connections, a constant cross-sectional area was assigned to the entire length of the truss element. To account for the change in BRB cross-section, the elastic stiffness of the truss element was modified similar to Oxborrow [6]. The brace material yield strength for the truss element was modified to match experimental result, similar to Coy [53].

Modeling of the EBF shear links and BRBF-E beam splices followed techniques used in previous EBF and BRBF-C studies. The shear links of the EBF were modeled using techniques proposed by Ramadan and Ghobarah [54] and modified slightly by Richards [32] (see Appendix B for description and validation of link model). The beam splices in the BRBF-E were modeled as fully pinned connections, based on findings in [18].

54

To account for P-delta effects, a single continuous column was added to each model, representing all gravity columns associated with the frames (one quarter of the buildings gravity columns were considered). The representative column was pinned at the base, and rigidly constrained to match the frame deformation at each floor. The stiffness and strength of the representative column was equal to the sum of the individual gravity columns, considering weak-axis bending. This technique is similar those used in other dynamic analysis studies [50,55,56,57]. Gravity loads corresponding to 1.2D+0.5L [47] were applied to the representative column. Fig. 3-6 shows the imposed constraints on the EBF and BRBF-E models.
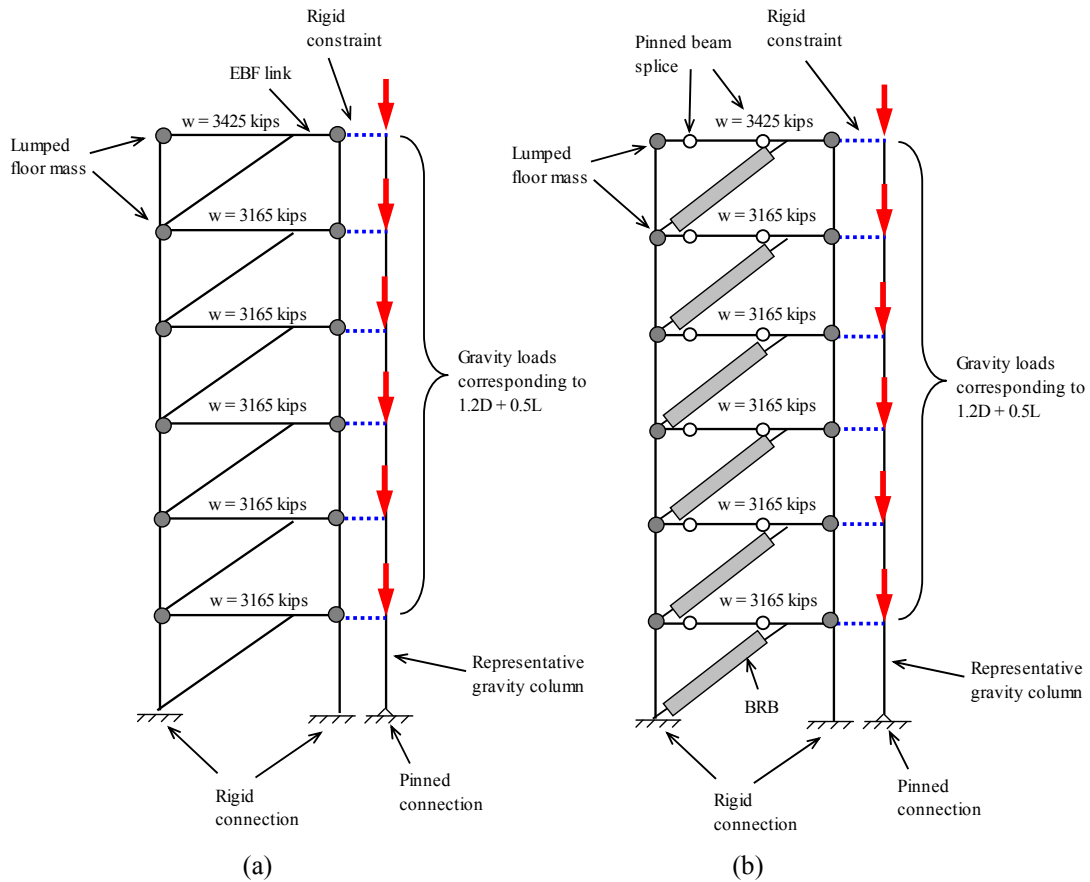
Fig. 3-6 Description of OpenSEES model constraints for (a) EBF and (b) BRBF-E

3.4.2. Analysis

Modal and static-pushover analyses were performed to ensure similar system strength between the EBF and BRBF-E designs and to investigate the relative stiffness of each frame type. The pushover analyses used the lateral force distribution prescribed by the equivalent lateral force procedure [47].

Dynamic analyses using ten scaled earthquake ground motions were also performed on each model, resulting in 240 analyses. The ground motions were scaled to match the design spectra at the fundamental period of each frame. A description of the ground motions used, along with the scale factors for each building are provided in Table 3-7 through Table 3-10. Fig. 3-7 shows the acceleration spectra for the ten earthquake records, along with the design acceleration spectrum. The design acceleration spectrum was determined from a design basis earthquake with 10% probability of exceedance in 50 years [47].

Table 3-7 EBF Earthquake Scale Factors for 30 ft Bay Width Frames

| | | | | Scale Factor | | | | | |
| | | | | 3-Story | | 6-Story | | 9-Story | |
Record	PGA^a (g)	R^b (km)	Site^c	I =1	I =1.5	I =1	I =1.5	I =1	I =1.5
1989 Loma Prieta									
47381 Gilroy Array No.3, LOMPAP/GO3090 ^{d}	0.37	14.40	D	1.20	1.21	0.77	0.81	0.75	0.72
57382 Gilroy array No. 4, LOMPAP/GO4090	0.21	16.10	D	1.25	1.35	0.85	0.75	1.65	1.30
1028 Hollister City Hall, LOMAP/HCH090	0.25	28.20	D	0.68	0.72	1.15	1.30	1.20	1.10
1656 Hollister Diff Array, LOMAP/HDA255	0.28	25.80	D	0.70	0.80	1.33	1.50	1.50	1.45
1695 Sunnyvale-Colton Ave., LOMAP/SVL360	0.21	28.80	D	2.00	2.10	1.45	1.05	1.00	1.05
1994 Northridge									
90053 Canoga Park, NORTHR/CNP196	0.42	15.80	D	0.70	0.88	0.65	0.65	0.55	0.60
90014 Beverly Hills-12520 Mulhol, NORTHR/MU2125	0.44	20.80	C	1.60	1.50	2.00	2.60	2.40	2.50
24278 Castaic - Old Ridge Route, NORTHR/ORR090	0.57	22.60	B	0.60	0.52	0.72	0.83	1.20	0.88
24088 Pacoima Kagel Canyon, NORTHR/PKC360	0.43	8.20	B	0.67	0.67	1.10	1.00	1.50	1.00
90021 LA-N Westmoreland, NORTHR/WST000	0.40	29.00	D	2.90	2.80	2.90	1.90	4.00	4.00

a. Peak Ground Acceleration

b. Distance to fault rupture

c. NEHRP Site class

d. Designation in Pacific Earthquake Engineering Research (PEER) database

Table 3-8 BRBF-E Earthquake Scale Factors for 30 ft Bay Width Frames

| | | | | Scale Factor [a] | | | | | |
| | | | | 3-Story | | 6-Story | | 9-Story | |
Record	PGA (g)	R(km)	Site	I =1	I =1.5	I =1	I =1.5	I =1	I =1.5
1989 Loma Prieta									
47381 Gilroy Array No.3, LOMPAP/GO3090	0.37	14.40	D	1.40	1.30	0.80	1.00	0.70	0.75
57382 Gilroy array No. 4, LOMPAP/GO4090	0.21	16.10	D	1.40	0.85	0.75	0.95	1.30	1.10
1028 Hollister City Hall, LOMAP/HCH090	0.25	28.20	D	1.20	1.40	1.25	0.95	1.10	1.00
1656 Hollister Diff Array, LOMAP/HDA255	0.28	25.80	D	0.93	0.82	1.50	1.00	1.50	1.35
1695 Sunnyvale-Colton Ave., LOMAP/SVL360	0.21	28.80	D	2.35	1.95	1.05	1.50	1.05	1.37
1994 Northridge									
90053 Canoga Park, NORTHR/CNP196	0.42	15.80	D	0.88	0.55	0.65	1.00	0.60	0.68
90014 Beverly Hills-12520 Mulhol, NORTHR/MU2125	0.44	20.80	C	1.30	1.20	2.80	1.70	2.40	1.85
24278 Castaic - Old Ridge Route, NORTHR/ORR090	0.57	22.60	B	0.61	0.80	0.80	0.90	0.85	0.71
24088 Pacoima Kagel Canyon, NORTHR/PKC360	0.43	8.20	B	0.60	0.67	1.05	0.90	1.00	1.20
90021 LA-N Westmoreland, NORTHR/WST000	0.40	29.00	D	2.20	2.80	2.00	2.85	4.00	3.80

a. See all notes from Table X

Table 3-9 EBF Earthquake Scale Factors for 20 ft Bay Width Frames

| | | | | Scale Factor [a] | | | | | |
| | | | | 3-Story | | 6-Story | | 9-Story | |
Record	PGA[a] (g)	R[b] (km)	Site[c]	I =1	I =1.5	I =1	I =1.5	I =1	I =1.5
1989 Loma Prieta									
47381 Gilroy Array No.3, LOMPAP/GO3090 [d]	0.37	14.40	D	1.20	1.40	0.75	0.80	0.80	0.70
57382 Gilroy array No. 4, LOMPAP/GO4090	0.21	16.10	D	1.30	1.40	1.00	0.78	1.80	1.30
1028 Hollister City Hall, LOMAP/HCH090	0.25	28.20	D	0.69	1.20	1.10	1.20	1.20	1.20
1656 Hollister Diff Array, LOMAP/HDA255	0.28	25.80	D	0.73	0.92	1.35	1.60	1.40	1.45
1695 Sunnyvale-Colton Ave., LOMAP/SVL360	0.21	28.80	D	2.10	2.30	1.40	1.10	0.70	1.10
1994 Northridge									
90053 Canoga Park, NORTHR/CNP196	0.42	15.80	D	0.80	0.80	0.68	0.60	0.65	0.55
90014 Beverly Hills-12520 Mulhol, NORTHR/MU2125	0.44	20.80	C	1.50	1.31	1.90	2.96	2.50	2.50
24278 Castaic - Old Ridge Route, NORTHR/ORR090	0.57	22.60	B	0.54	0.70	0.70	0.76	1.40	0.89
24088 Pacoima Kagel Canyon, NORTHR/PKC360	0.43	8.20	B	0.67	0.60	1.15	1.10	1.50	1.05
90021 LA-N Westmoreland, NORTHR/WST000	0.40	29.00	D	2.80	2.20	3.00	2.00	4.20	4.00

a. See all notes from Table X

Table 3-10 BRBF-E Earthquake Scale Factors for 20 ft Bay Width Frames

| | | | | Scale Factor [a] | | | | | |
| | | | | 3-Story | | 6-Story | | 9-Story | |
Record	PGA (g)	R(km)	Site	I =1	I =1.5	I =1	I =1.5	I =1	I =1.5
1989 Loma Prieta									
47381 Gilroy Array No.3, LOMPAP/GO3090	0.37	14.40	D	1.40	1.30	0.80	1.00	0.70	0.75
57382 Gilroy array No. 4, LOMPAP/GO4090	0.21	16.10	D	1.40	0.85	0.75	0.95	1.30	1.10
1028 Hollister City Hall, LOMAP/HCH090	0.25	28.20	D	1.20	1.40	1.25	0.95	1.10	1.00
1656 Hollister Diff Array, LOMAP/HDA255	0.28	25.80	D	0.93	0.82	1.50	1.00	1.50	1.35
1695 Sunnyvale-Colton Ave., LOMAP/SVL360	0.21	28.80	D	2.35	1.95	1.05	1.50	1.05	1.37
1994 Northridge									
90053 Canoga Park, NORTHR/CNP196	0.42	15.80	D	0.88	0.55	0.65	1.00	0.60	0.68
90014 Beverly Hills-12520 Mulhol, NORTHR/MU2125	0.44	20.80	C	1.30	1.20	2.80	1.70	2.40	1.85
24278 Castaic - Old Ridge Route, NORTHR/ORR090	0.57	22.60	B	0.61	0.80	0.80	0.90	0.85	0.71
24088 Pacoima Kagel Canyon, NORTHR/PKC360	0.43	8.20	B	0.60	0.67	1.05	0.90	1.00	1.20
90021 LA-N Westmoreland, NORTHR/WST000	0.40	29.00	D	2.20	2.80	2.00	2.85	4.00	3.80

a. See all notes from Table X

Fig. 3-7 Design spectra and individual earthquake spectra

3.4.3. Modal and Static Pushover Results

The static pushover results indicate similar design system strengths were achieved between the EBF and BRBF-E designs. Fig. 3-8 and Fig. 3-9 show the normalized base shear (V/Ve) versus roof drift for each EBF and BRBF-E design. For the pushover curves, V/Ve equal to one represents the frame drift under the equivalent lateral forces. The similar yield and ultimate strength values between the EBF and BRBF-E designs confirm that similar design system strengths were achieved. Also, system overstrength at a drift of 0.015 rad was between 1.3 and 1.7, reasonably similar to the value of 2 assumed in design [47]. System overstrength was determined by the peak normalized shear (see Fig. 3-10). As expected, the system stiffness decreased with building height, evident by the slope decrease progressing between the 3-, 6-, and 9-story pushover curves.

Natural vibration periods indicate that BRBF-Es are stiffer than EBFs when designed to have equal strength. Table 3-11 shows the fundamental natural period of each frame, determined from modal analysis. Vibration periods are directly related to building stiffness, with shorter

periods indicating a stiffer structure. The natural periods of the BRBF-E designs were consistently shorter than those of the EBFs; on average the BRBF-E periods were 22% shorter than the EBF periods. The periods for the 3-, 6-, and 9-story BRBF-Es ranged from 0.55-2.24 seconds, while the periods for the EBFs ranged from 0.71-2.45 seconds. As expected, periods for the strength level I=1.5 designs were shorter than those of the I=1.0 designs (compare columns 1-2 with columns 3-4 in Table 3-11).

a. = Roof drift under equivalent lateral force

Fig. 3-8 Pushover analysis results for EBF and BRBF-Es with 30 ft bay width

59

EBF

BRBF-E

a. = Roof drift under equivalent lateral force
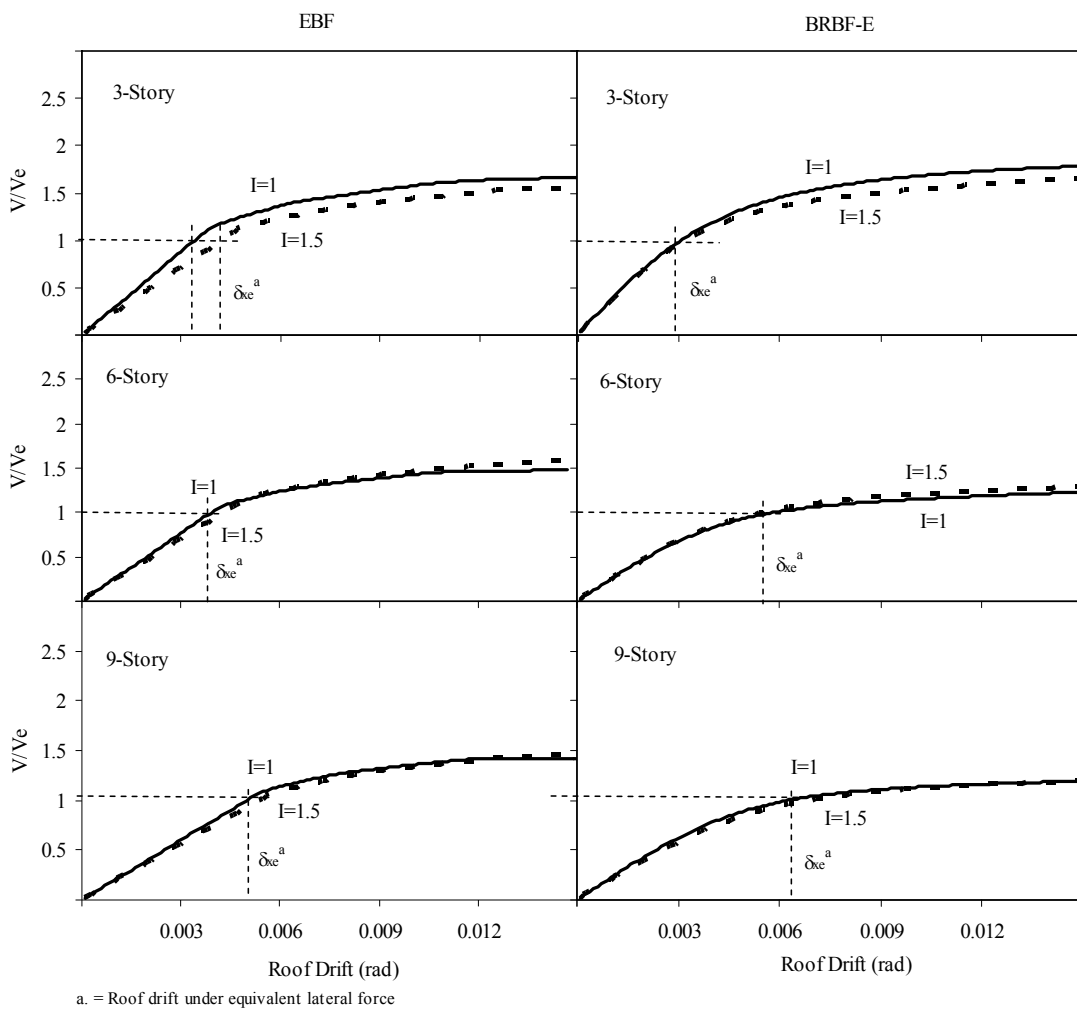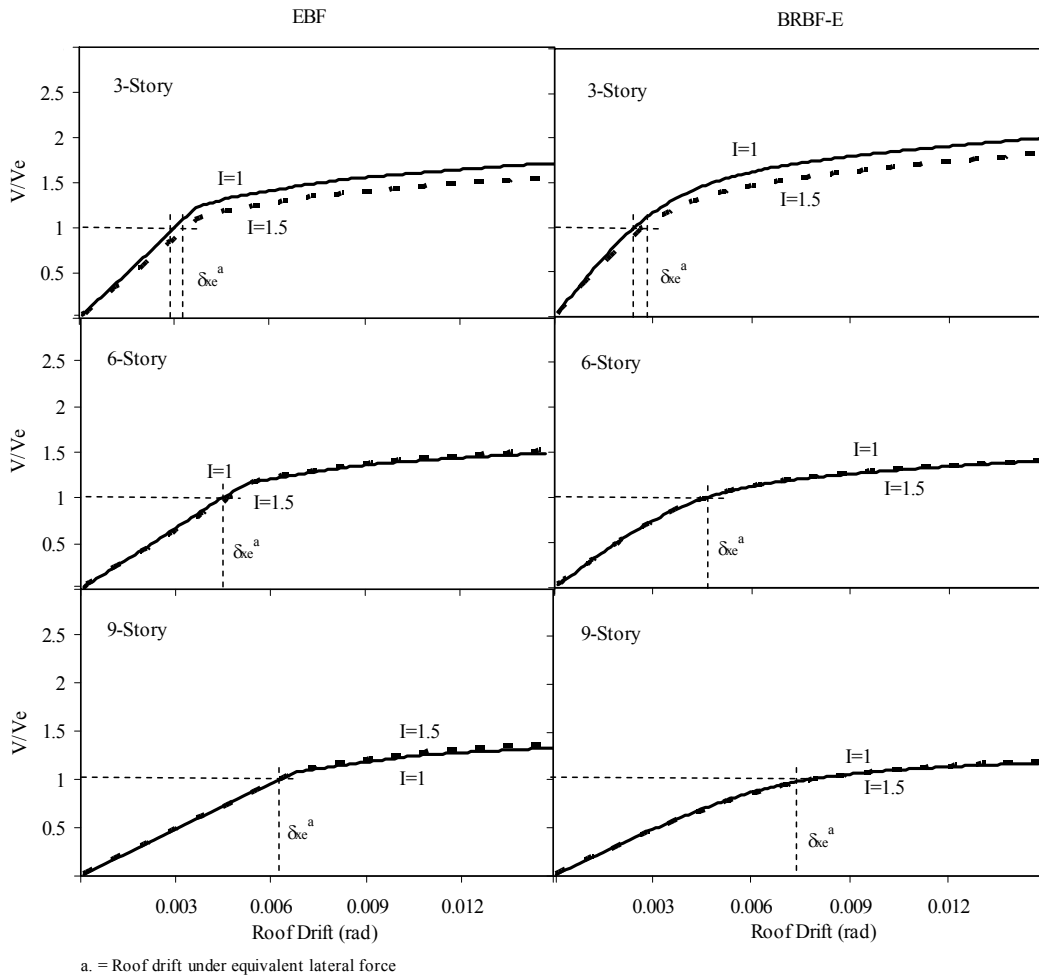
Fig. 3-9 Pushover analysis results for EBF and BRBF-Es with 20 ft bay width
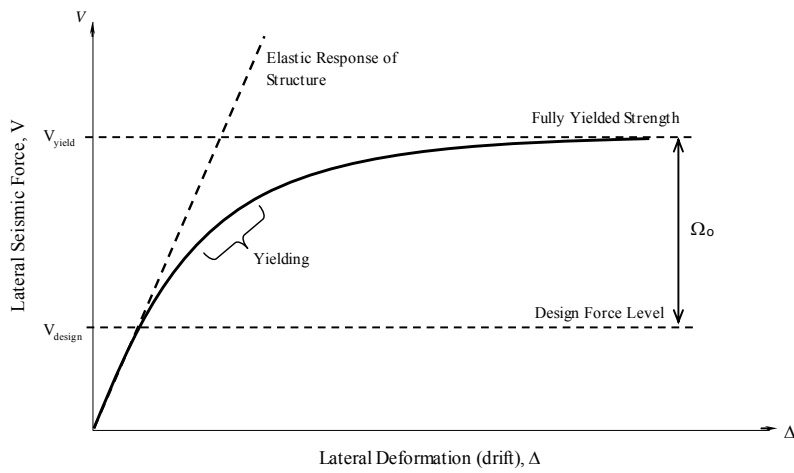
Fig. 3-10 Determination of system overstrength factor from pushover curve

60

Table 3-11 Fundamental Natural Periods for EBF and BRBF-E design

System	I=1[a]		I=1.5	
	20ft[b]	30ft[c]	20ft	30ft
3-Story				
EBF	0.83	0.88	0.71	0.79
BRBF-E	0.65	0.72	0.55	0.59
6-Story				
EBF	1.64	1.56	1.36	1.31
BRBF-E	1.28	1.34	1.05	1.09
9-Story				
EBF	2.45	2.30	2.03	1.95
BRBF-E	2.24	1.95	1.86	1.66

a. Occupancy importance factor (ASCE 7-05)

b. 20ft bay width frames

c. 30ft bay width frames

3.5. Results from Nonlinear Dynamic Analyses

The dynamic performance of the BRBF-E and EBF models is presented in three parts. The first part focuses on peak inter-story drift, to compare the relative deformation demands between the EBF and BRBF-E frames. Next, the amount of frame damage resulting from the dynamic loading is assessed for both the EBF and BRBF-Es by looking at residual frame drifts. Finally, seismic column demands for each frame type are discussed, and compared with design column demands to validate design assumptions and determine applicable design modifications.

3.5.1. Peak and Residual Story Drifts

The 3-, 6-, and 9-story BRBF-E and EBF designs all performed well under the dynamic loading. Fig. 3-11 shows the average maximum story drift for the 30 ft bay width EBF and BRBF-E designs due to ten scaled earthquake ground motions. Fig. 3-12 shows the average maximum story drift for the 20 ft bay width designs. Individual drift responses for each frame are provided in Appendix C. The EBF and BRBF-E designs responded with average maximum drift values less than 2%, meeting the life-safety drift performance objective for EBF and BRBF-

61

C structures [58]. Drifts for the I=1.5 designs were lower on average than the I=1 designs, which is expected considering the increased stiffness. Note however, that the drifts in the top stories are worse for I=1.5, possibly due to dynamic effects.
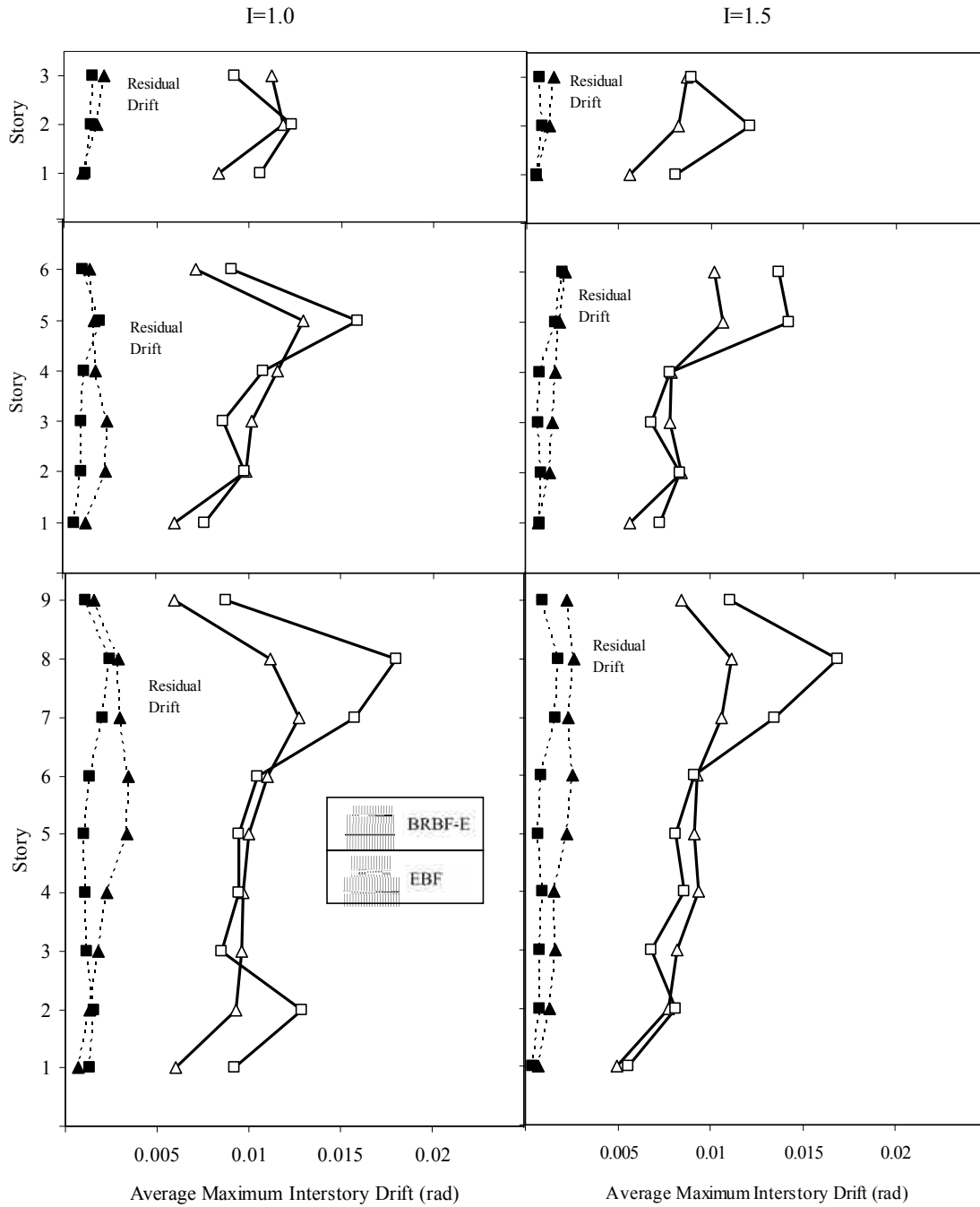
Fig. 3-11 Average maximum inter-story drift for EBF and BRBF-Es with 30 ft bay width
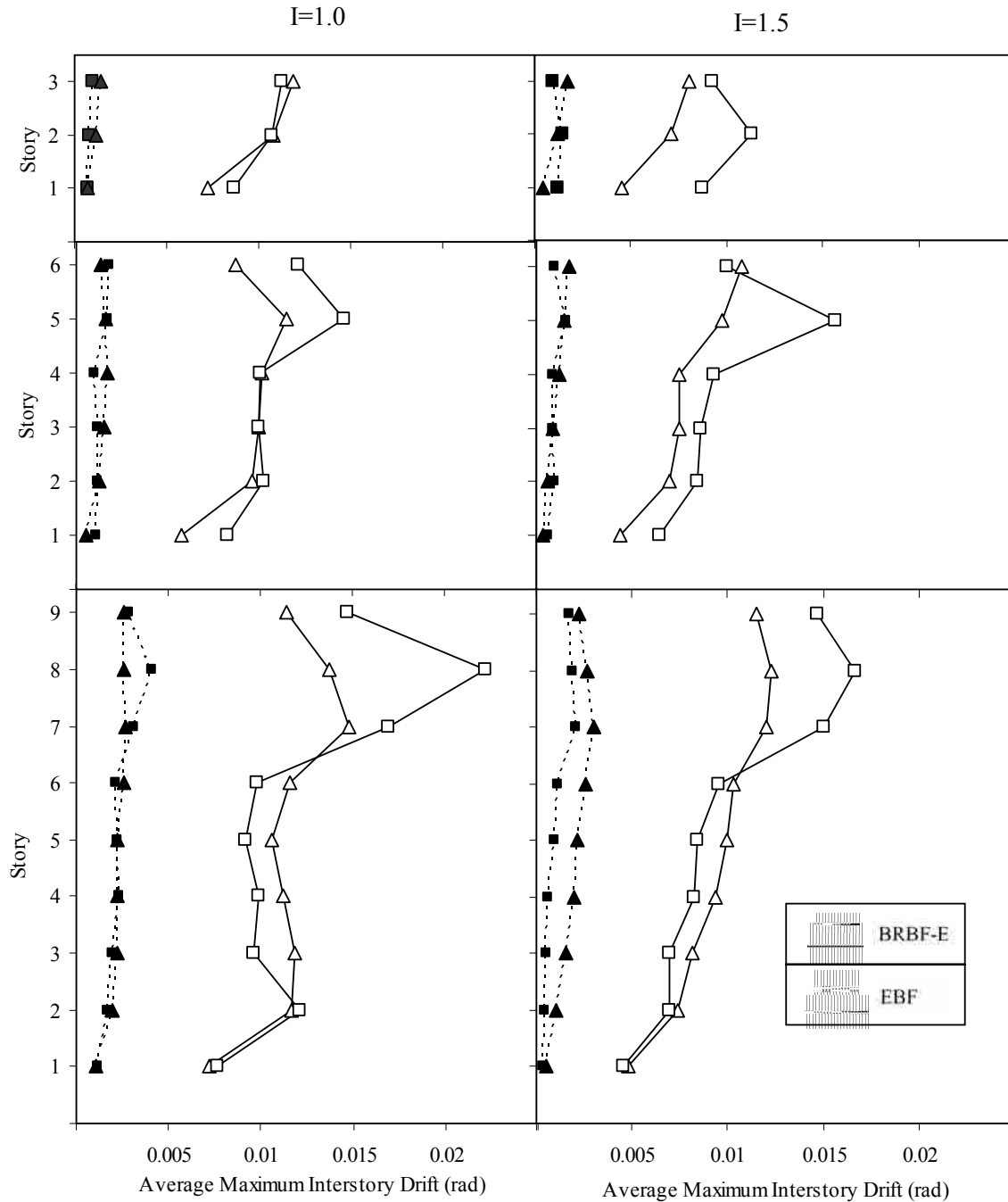
Fig. 3-12 Average maximum inter-story drift for EBF and BRBF-Es with 20 ft bay width

Further comparison of drift values between the EBF and BRBF-E models indicates that the BRBF-E designs performed slightly better than the EBF designs. Drift values in the lower and upper stories of the BRBF-Es were consistently lower than those of the EBFs, while drifts in

the mid-stories of each frame type were similar (see Fig. 3-11 and Fig. 3-12). Since story strengths between the EBF and BRBF-Es were similar, increased drift in the upper and lower EBF stories is likely due to dynamic effects (note the difference in periods between the EBF and BRBF-Es in Table 3-11). These dynamic effects are less evident in the 3-story designs, most likely due to the shorter building heights and periods.

Frame damage within the EBF and BRBF-E models were limited to the links and braces respectively. Residual frame drifts for both frame types were reasonably low, with the average maximum residual drifts for both frame types less than 0.5%, for all frame heights (see Fig. 3-11 and Fig. 3-12). A Japanese study on permissible residual deformation levels conducted by [59] concluded that buildings having residual drifts less than 0.5% were more economical to repair rather than re-build.

Although both frame types had low residual story drifts, the BRBF-Es sustained higher residual drifts than the EBFs. Comparing residual drifts between the EBF and BRBF-E designs (see Fig. 3-11 and Fig. 3-12), BRBF-E residual drifts are somewhat greater than the EBF residual drifts. This is somewhat expected; for a given drift angle, BRBF-E braces will strain more than the EBF links rotate. When designed to a higher strength level (I=1.5) residual drifts in the BRBF-Es decreased, due to decreased yielding.

While the EBF inter-story drifts in Fig. 3-11 and Fig. 3-12 were relatively small (less than 2%), EBF link rotations in the upper stories of the taller frames were large, indicating ductility issues with the EBF designs. Fig. 3-13 and Fig. 3-14 show the EBF link rotations for the 30 ft and 20 ft frame designs respectively. In Fig. 3-13 and Fig. 3-14 average link rotations for the 6- story frames exceeded 0.07 rad. Link rotations in the 9-story frames exceeded 0.09 rad for the 30 ft designs and 0.08 rad for the 20 ft designs. The largest experimental link rotation

achieved by Okazaki et al. [7] was 0.07 rad with specimen NAS, having no weld access holes and a modified welding detail. At 0.07 rad, specimen NAS experienced non-ductile fractures originating in the web at the stiffener welds.

I=1   I=1.5
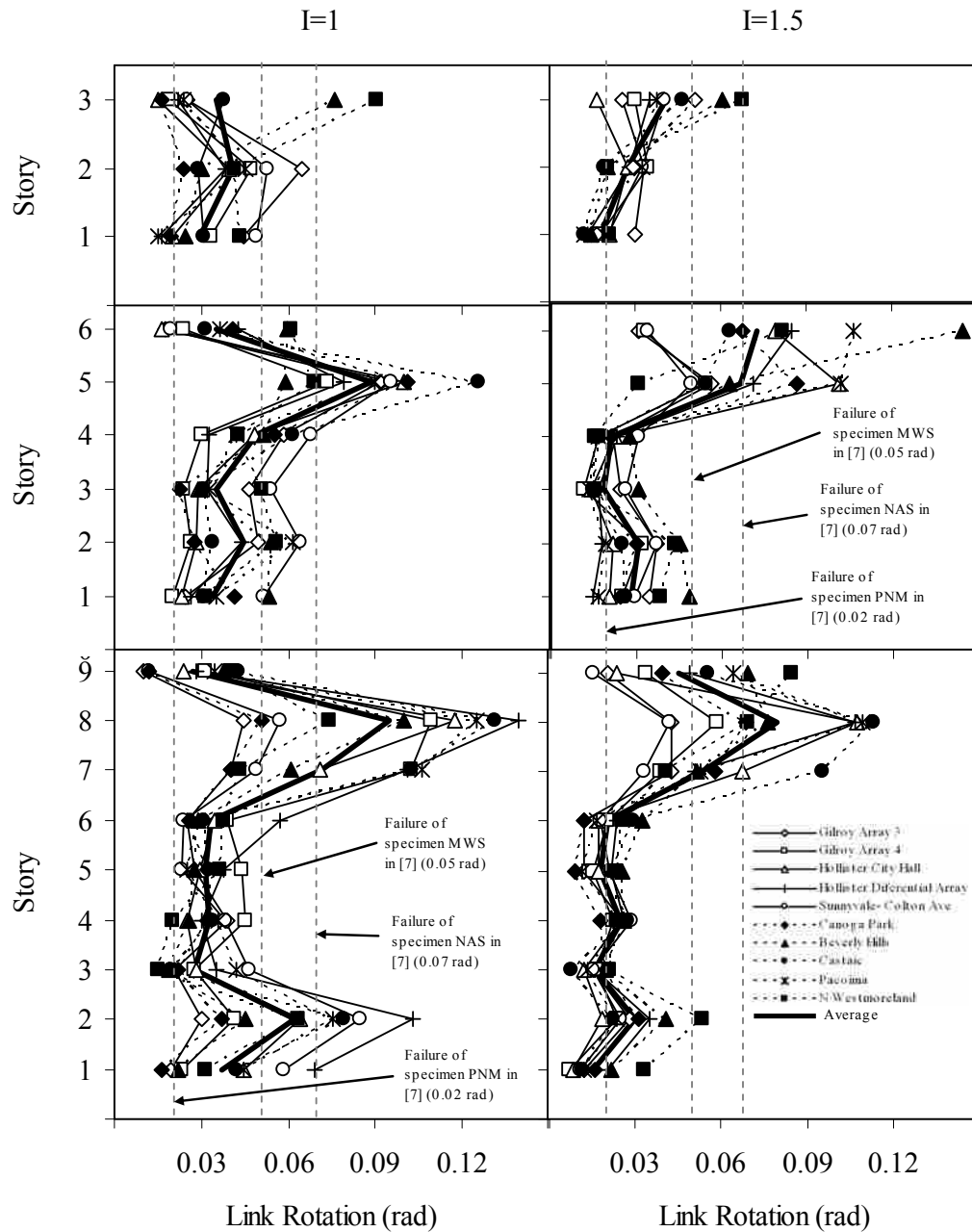
Fig. 3-13 EBF link rotations for 30 ft bay width frames

I=1   I=1.5
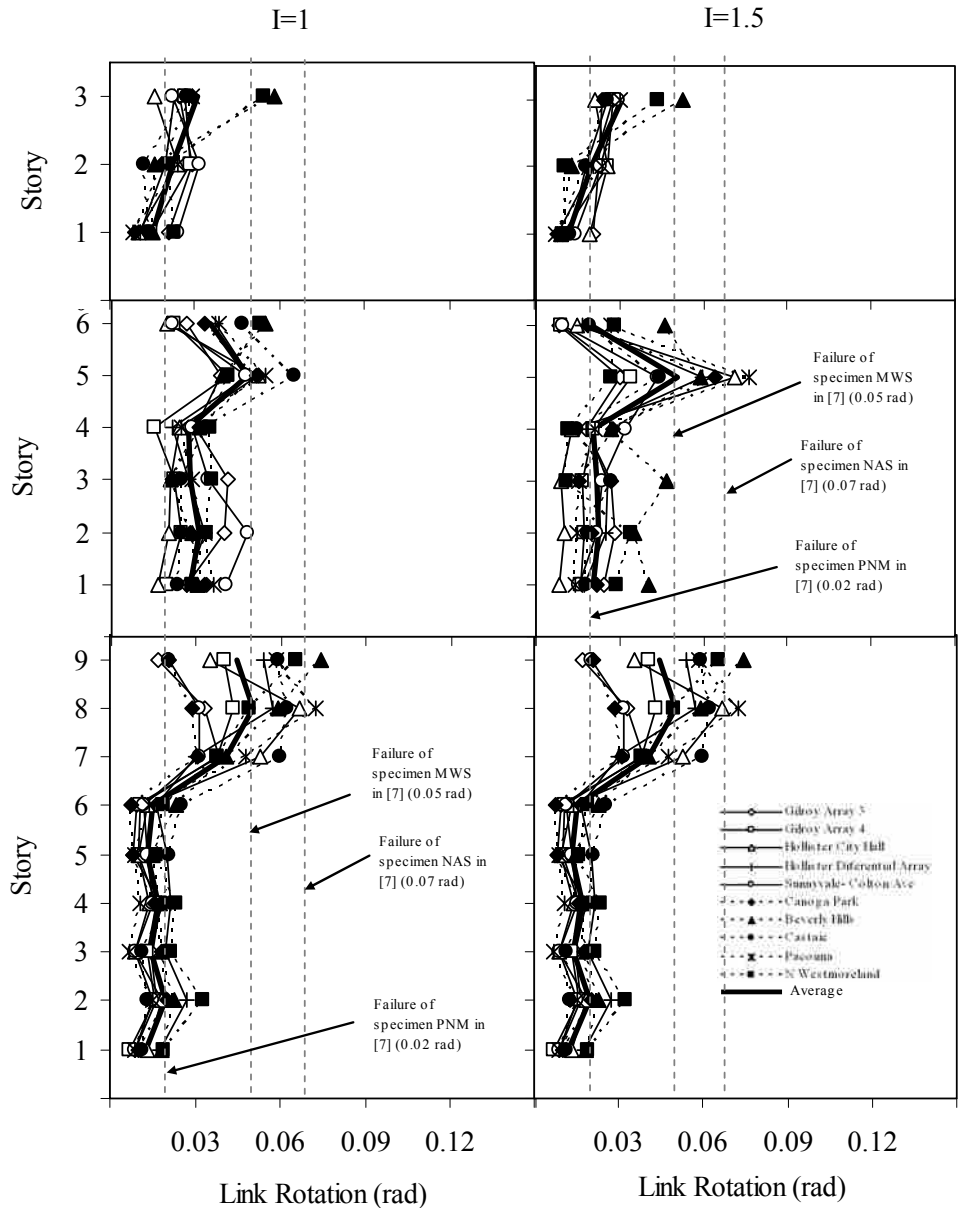
Fig. 3-14 EBF link rotations for 20 ft bay width frames

3.5.2. Column Demands

The average ultimate axial column demand at each story, Pu, resulting from the ten

earthquake ground motions were normalized by the design column axial demand, Pd.   The

design axial demands (Pd) assumed simultaneous yielding of all ductile members throughout the

frame height.   By comparing actual column demands with design column demands, the

66

conservancy of various design assumptions can be evaluated. The normalized axial demands (Pu/Pd) are provided for each strength level (I=1 and I=1.5) and frame width (30 ft and 20 ft). Fig. 3-15 shows the column demands for the 30 ft bay width frames and Fig. 3-16 shows the column demands for the 20 ft bay width frames. In Fig. 3-15 and Fig. 3-16, the dashed line at Pu/Pd=1 represents the column demands assuming all braces developed their ultimate capacity simultaneously (hereafter called design column demand).
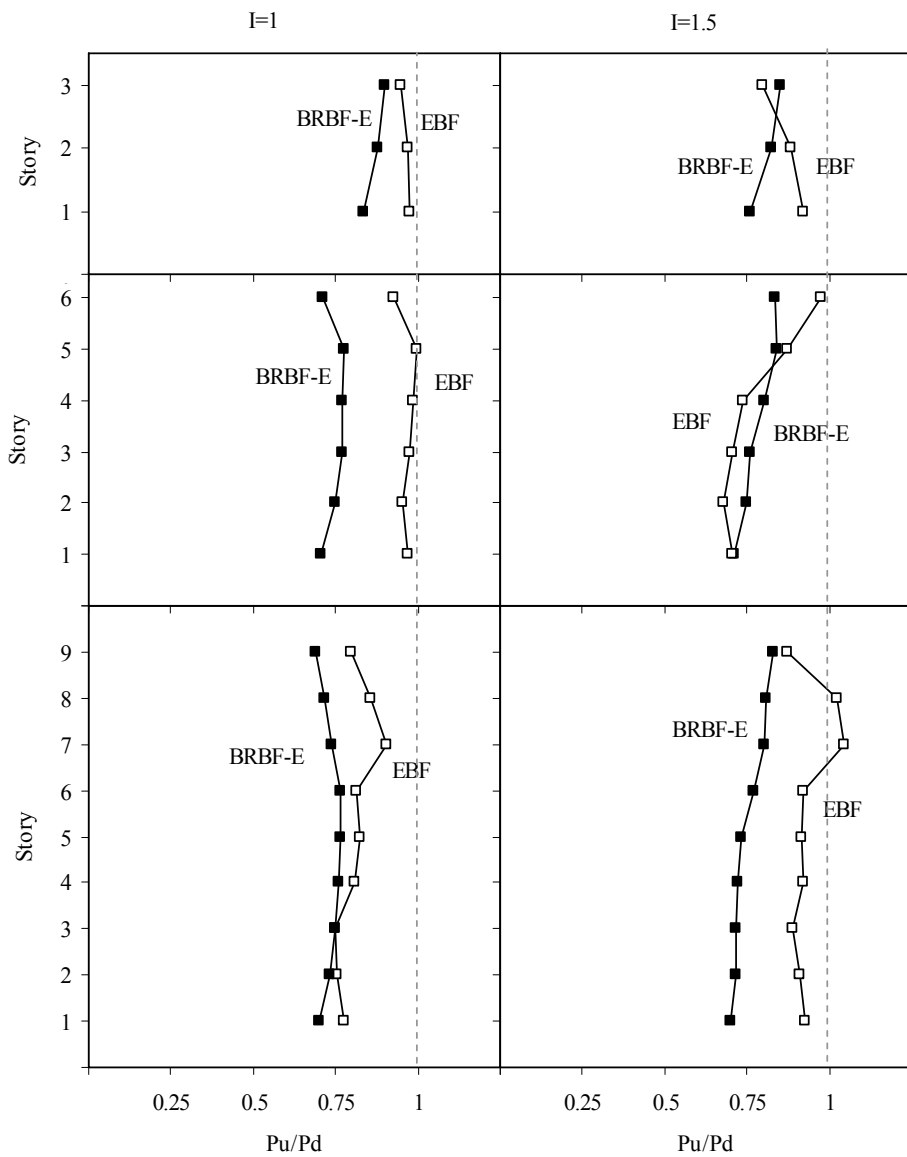
Fig. 3-15 Normalized average maximum column demands for 30 ft bay width frames

67
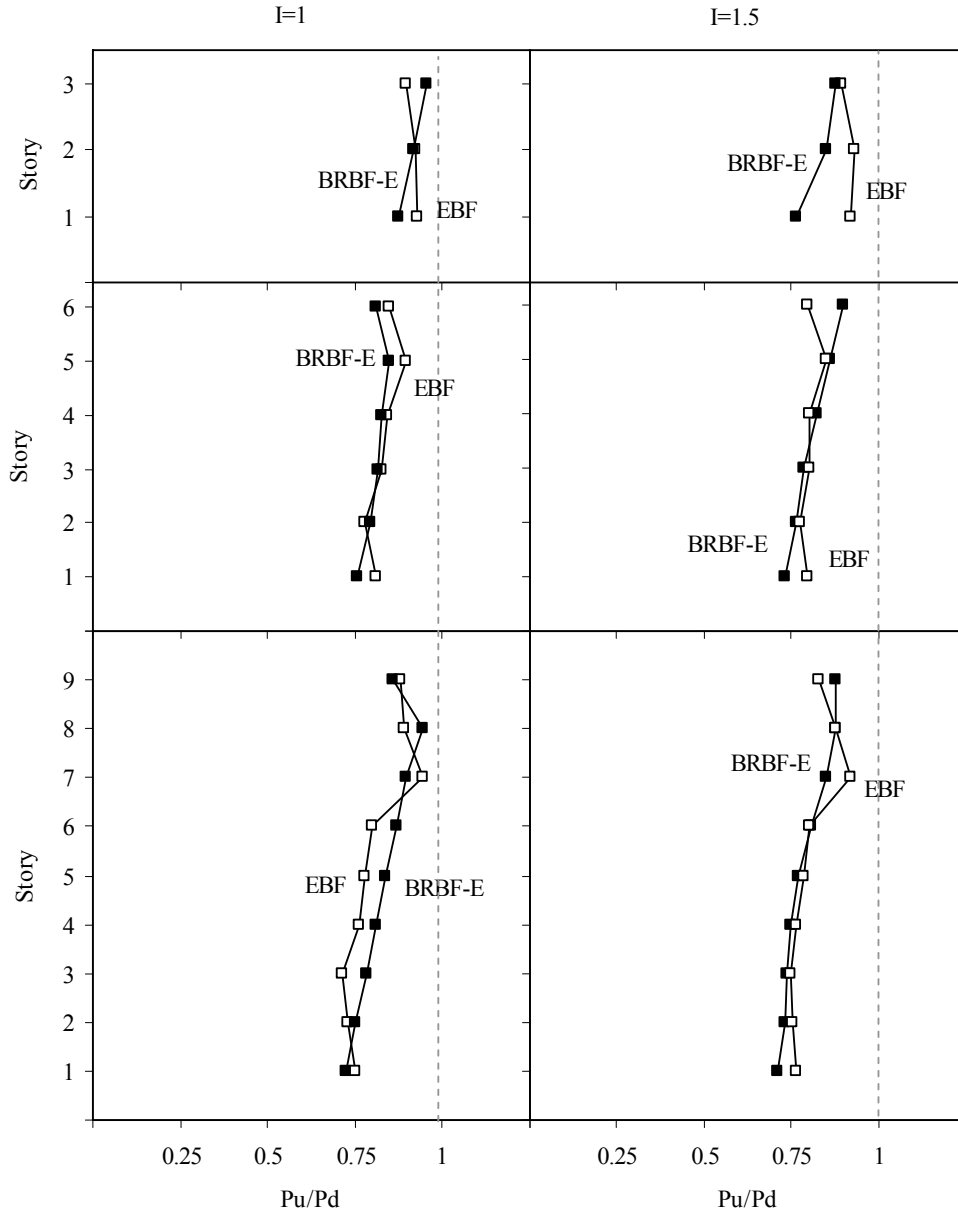
Fig. 3-16 Normalized average maximum column demands for 20 ft bay width frames

Average normalized column demands for the BRBF-Es and EBFs were lower than those assumed in design. In the 6- and 9-story 30 ft BRBF-Es, ultimate column demands were 30% lower on average than those calculated for design (see Fig. 3-15). In the lower stories of the 6- and 9-story 20 ft BRBF-Es and EBFs, ultimate column demands were 27% lower on average than those calculated for design (see Fig. 3-16). This reinforces the findings in [50], and

validates the design assumption used when sizing the columns of the 9-story frames (design column demands in the 9-story frames were reduced by 30%). In the bottom story of the 30 ft 3-story BRBF-E frames, normalized column demands were 10-15% lower on average than the design demands, and between 5-12% lower on average for the 20 ft frames.

The difference between the design column demand and the actual column demand can be attributed to the braces and links not reaching their full capacity. Consider the distribution of maximum brace and link force along the frame height, presented as a percent of their individual capacities (F/Fult), for one of the 6-story frames (I=1, width=20 ft) (see Fig. 3-17). In the sample 6-story frames, the braces and links fail to simultaneously reach their full capacity (evident by the differing amounts of brace and link yielding between floors), suggesting design column demands are over conservative.
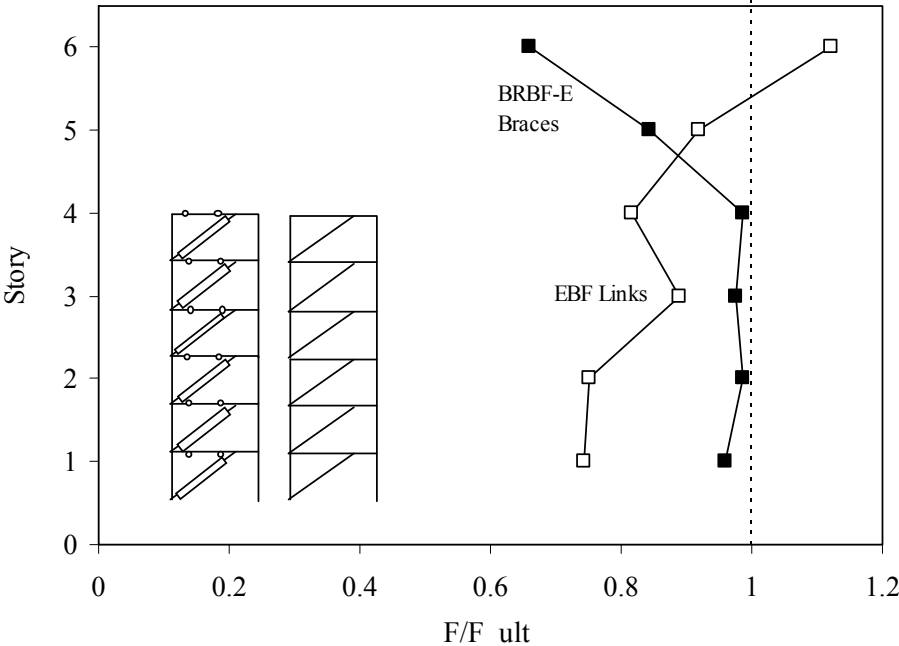
Fig. 3-17 Distribution of brace and link yielding in 6-story (I=1, width=30 ft) frame due to Gilroy Array 3 motion

There was little variation in Pu/Pd between the two strength levels (I=1 or I=1.5) of the 6- and 9-story BRBF-Es.   Less than 2% variation in Pu/Pd was observed in the lower stories of the 6- and 9-story BRBF-Es; however, column demands between the different strength levels of the 3-story frames differed by nearly 10%, with Pu/Pd being lower for the stronger frames.

Column demand reductions proposed by [50] for BRBF-Cs are also applicable to BRBF-Es. Axial column demand results from nonlinear dynamic analysis of BRBF-Es suggest it is reasonable to reduce the design column demands.   Column demands used for the BRBF-E design were determined assuming all braces develop their ultimate capacity simultaneously; however, normalized column demands resulting from 120 dynamic analyses indicate that this does not happen. Normalized mean plus one standard deviation column demand values for the lower columns of the 9-story frames ranged between 81-77% of the design column demand, which along with average 6-story results suggest that for taller BRBF-Es (6-stories and greater) design column demands can be reduced by between 20-30%.   This result is similar to the findings presented in [50] for tall BRBF-Cs.

3.6. EBF and BRBF-E Weight Comparison

In this section, the 12 EBF and 12 BRBF-E designs were broken down into individual components (beams, braces, and columns), and the steel weight for each component was determined. The weight of the buckling-restrained braces was determined from the steel core area and brace length only; the concrete encasement was not considered. All weight calculations assumed a constant steel density equal to 490 lb/ft^3 (7849 kg/m^3). The following paragraphs compare the overall frame weight between the EBF and BRBF-Es, as well as the frame weight contribution from the individual components.

70

BRBF-E designs are heavier than EBF designs when designed to have equal strength. Figs. 3-18 through 3-19 show the total frame weight for the 30 ft and 20 ft bay width BRBF-E and EBF designs respectively. Frame steel weights for the taller BRBF-Es (6- and 9-stories) were, on average, 46% heavier than the EBFs at a strength level I=1, and 98% heavier at a strength level I=1.5 (see Fig. 3-18 and Fig. 3-19). For the 3-story 30 ft bay width designs, the BRBF-Es were 48% heavier than the EBFs, on average; for the 20 ft bay width designs, the BRBF-Es were 95% heavier than the EBFs, on average.
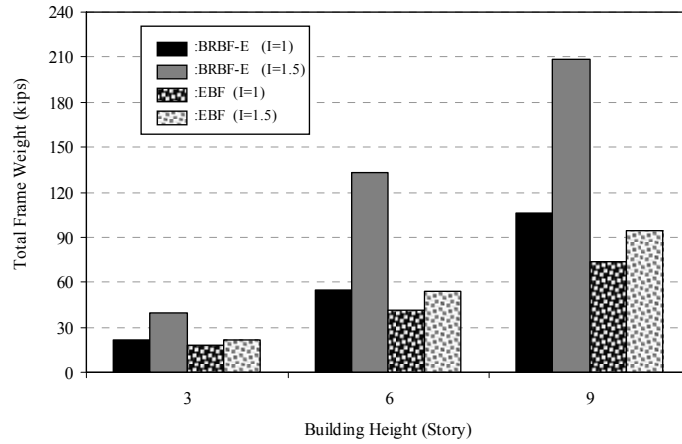
Fig. 3-18 Comparison of total frame weight for the 30 ft EBF and BRBF-E designs
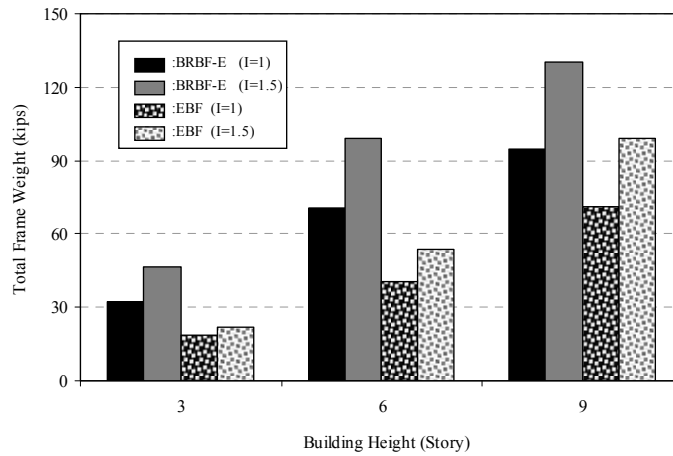
Fig. 3-19 Comparison of total frame weight for the 20 ft EBF and BRBF-E designs

71

Building height has little effect on frame weight distribution. Fig. 3-20 shows the percentage of total frame weight for BRBF-E and EBF beams, columns, and braces. The distribution of frame weight between the beams, columns, and braces is consistent across multiple story heights. Due to large axial and moment demands, BRBF-E columns contribute most to the frame weight. Column sizes in BRBF-Es account for near 60% of the total frame weight for the 3-, 6-, and 9-story, 30 ft-width frames, and near 70% of the weight of the 20 ft-width frames (see Fig. 3-20). As expected, the ductile elements (EBF beams and BRBF-E braces) made up the smallest fraction of total frame weight.
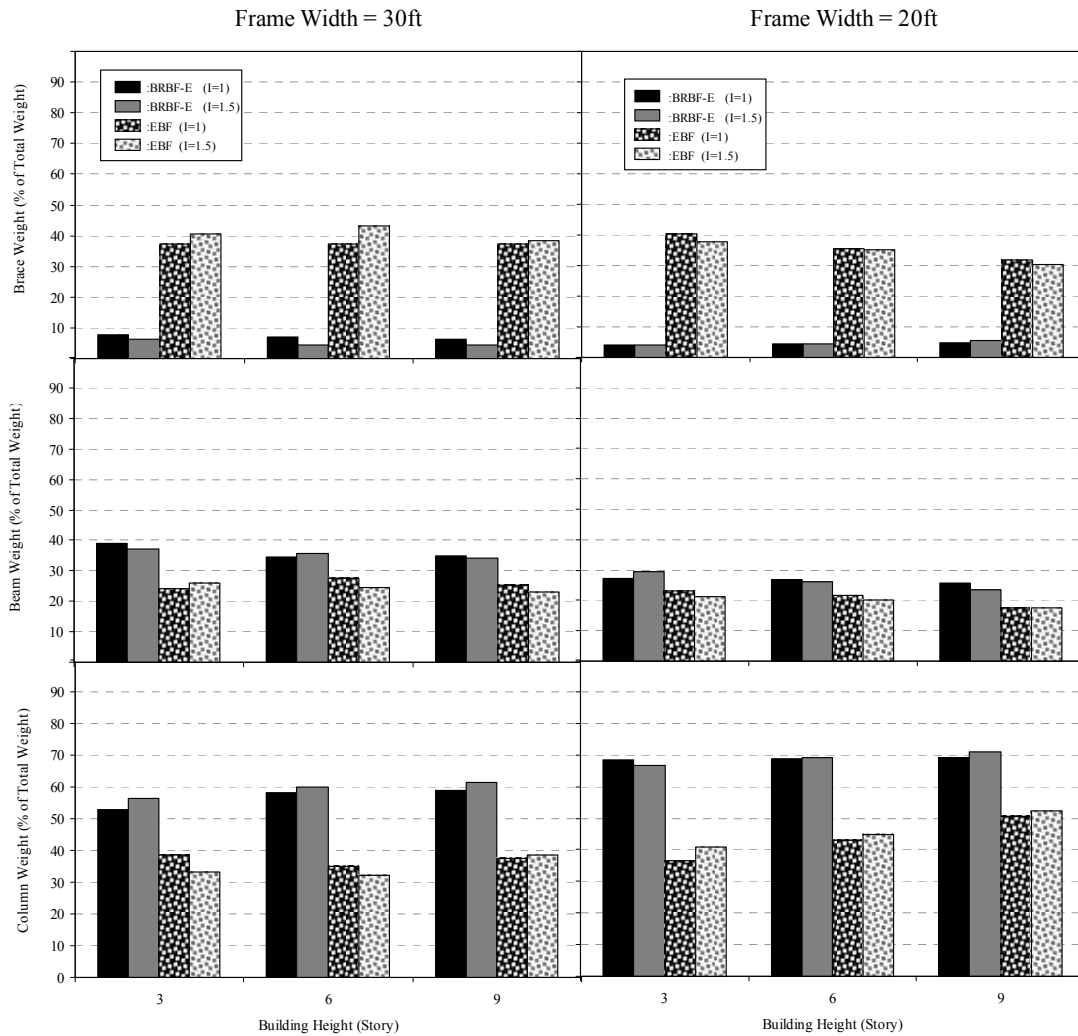
Fig. 3-20 Normalized frame component weights for the 30 and 20 ft EBF and BRBF-E designs

72

3.7. Performance Comparison Summary

Consider the 6-story BRBF-E and EBF designed for the comparison study (I=1, width=30 ft). Both frame types accommodated architectural openings using brace eccentricities; both frames had similar strength (compare pushover curves in Fig. 3-8); both frames sustained similar average maximum story drifts, less than 2%, when dynamically loaded under multiple scaled ground motions; and both frames had similar residual story drifts, less than 0.5%.

With similarities in performance and configuration, the advantages of the BRBF-E over the EBF are ease of design, ease of reparability, and economy. The BRBF-E was simpler to design than the EBF. Determining design forces for the BRBF-E beams, columns, and braces was simpler than determining EBF member forces, which needed to be determined from elastic analysis. Also, unlike the EBF design, beam sizes and brace connection details could be repeated throughout the BRBF-E height (without sacrificing performance), simplifying both design and construction. In the BRBF-E, damage was isolated within the brace, and in the EBF, damage was isolated within the link. Damage to the BRBF-E could be easily repaired by replacing the brace, whereas replacement of the entire beam in the EBF would be more difficult (especially when connected to the concrete slab).

With construction accounting for the majority of a building project's cost, BRBF-Es may be more economical than EBFs, because they are easier to construct. In construction of EBF links, multiple stiffener welds are done in the shop, but usually the braces need to be field welded. Depending on the number of EBF links and braces specified in design, the amount of welding can significantly impact construction costs. The amount of field welding for BRBF-Es is significantly less than that for EBFs, since BRBF-E stubs don't require web stiffeners, and the buckling-restrained braces can be attached to the frame through bolted gusset connections.

The low-rise EBF and BRBF-E designs in the previous comparison study don't represent common engineering practice. The EBFs in the comparison study were designed with different beam sizes at each floor, to achieve the best possible performance; however, it is common practice to repeat beam sizes in low-rise EBFs, to simplify design and construction. Also, for comparison purposes, the BRBF-Es in the previous section were designed based on demands from EBF story strengths rather than code-based seismic forces.

3.8. Design Example

The following design example is provided to compare the relative performance of EBFs and BRBF-Es, designed according to common engineering practice. The design example is presented in four parts. First, design procedures for BRBF-Es with stub-to-column and mid-span configurations are summarized. Then two prototype buildings are described, along with details of the building-site characteristics. Next, designs of two BRBF-Es having different story heights are presented, and the designs are compared with code designed EBFs of similar configuration. Lastly, nonlinear dynamic analysis is performed for each BRBF-E and EBF, and their seismic performance is compared.

3.8.1. BRBF-E Design Steps

The design of BRBF-E systems can be described in ten steps. The following step-by-step design procedure is based on earlier development of BRBF-E static member forces and current BRBF-C capacity based design procedures. The ten steps apply to BRBF-Es with stub-to-column and mid-span configurations, as shown in Fig. 3-1(c and d):

1) Get frame base shear and story forces using equivalent lateral force (ELF) procedure described in ASCE Standard 7-05 [47].

2) Determine brace axial force $F_{brace}=V(1-e/L)L_{brace}$ (for stub-to-column configurations) or $F_{brace}=(V/L)(1+e/(2b))((L-e)^2/4+h^2)^{1/2}$ (for mid-span configurations), where V=story shear, e=stub length, L=bay length, h=story height, L_{brace}=brace length, and b=distance between brace connection and beam splice.

3) Select a brace area that satisfies $\phi A_{br}F_y \geq F_{br}$, where A_{brace}=brace area, ϕ=0.9 (strength reduction factor), F_y=brace yield strength, and F_{brace}=brace force (from Step 2).

4) Determine ultimate brace capacity $F_{br\_ult}=(\alpha\beta\omega)F_{brace}/\phi$, where $(\alpha\beta\omega)$=approximately 1.8 (buckling-restrained brace overstrength factors).

5) Obtain the shear force (V_s) and bending moment (M_s) in the stub using equations 3-3 through 3-6; obtain the column axial force (P_{col}) and moment (M_{col}) considering cumulative stub shears and moments; and obtain the beam axial load (P_b) from V, and the shear force (V_b) and bending moment (M_b) from factored gravity loads.

6) Select a stub size such that $\phi V_{nx}>V_s$ and $\phi M_n>M_s$, where ϕ=0.9 (strength reduction factor), V_{nx}=stub nominal shear capacity, M_n=stub nominal moment capacity, V_s=stub shear force (from Step 5), and M_s=stub moment (from Step 5).

7) Select a beam size such that $\phi V_{nx}>V_b$, $\phi M_n>M_b$, and $\phi_c P_n$>Pb, where ϕ=0.9 (strength reduction factor), V_{nx}=beam nominal shear capacity, M_n=beam nominal moment capacity, P_n=beam nominal axial capacity, V_b=beam shear force (from Step 5), M_b=beam moment (from Step 5), and P_b=beam axial force (from Step 5).

8) Select a column size that satisfies the following interaction equation:
$$\left.\begin{cases} pP_{col}+b_xM_{xcol}+b_yM_{ycol}\leq 1.0 & [pP_{col}\geq 0.2] \\ (1/2)pP_{col}+(9/8)(b_xM_{xcol}+b_yM_{ycol})\leq 1.0 & [pP_{col}<0.2] \end{cases}\right\},$$
where $p=1/(\phi_c P_n)$, $b_x=8/(9\phi_b M_{nx})$ strong axis bending coefficient, $b_y=8/(9\phi_b M_{ny})$ weak axis bending coefficient, $\phi_c P_n$=column axial capacity, $\phi_b M_{nx}$=column moment capacity (strong axis), $\phi_b M_{ny}$=column moment capacity (weak axis), P_{col}=column axial load (from Step 5), M_{xcol}=column moment (strong axis, from Step 5), and M_{ycol}=column moment (weak axis, from Step 5).

9) Obtain the approximate inelastic roof drift
$$\Delta_{roof}=C_d\sum_{i=1}^{nstory}\frac{V_iL_{br,i}^3}{EA_i(L-e)^2},$$
where C_d=deflection amplification factor (C_d=5.5 for BRBF-Cs), V_i=story shear at story i, $L_{br,i}$=brace length at story i, E=elastic material stiffness, A_i=brace area at story i, L=bay length, e=stub length.

10) Compare Δ_{roof} with allowable drift in [58], if Δ_{roof}>allowable drift, return to Step 3 and select a larger brace area.

3.8.2. Description of Prototype Buildings

The two prototype buildings considered in the design example consist of a 3-, and 6-story office building having both BRBF-Es and EBFs (see Fig. 3-21 and Fig. 3-22). The bay dimensions and floor masses used in the design were slightly modified from a SAC study [60]. The seismic weight for the entire 3-story building is 9,755 kips (1.5 times that in [60]) and 19,250 kips for the 6-story building. The location and configuration of the 3-, and 6-story BRBF-Es and EBFs are shown in Fig. 3-21 and Fig. 3-22 respectively. A Los Angeles, California site was used for design with S_{DS}=1.12 and S_{D1}=0.63, where S_{DS} and S_{D1} are the site design spectral accelerations at 0.2 and 1.0 seconds in terms of gravity. The equivalent seismic demands for the BRBF-Es and EBFs, as determined from the equivalent lateral force procedure [47], are provided in Table. 3-12.

Total Floor Weights:
Floor 1= 3165 kips
Floor 2= 3165 kips
Floor 3= 3425 kips

All stub and link lengths are 1.22m (4 ft)

All story heights are 3.96m (13 ft)
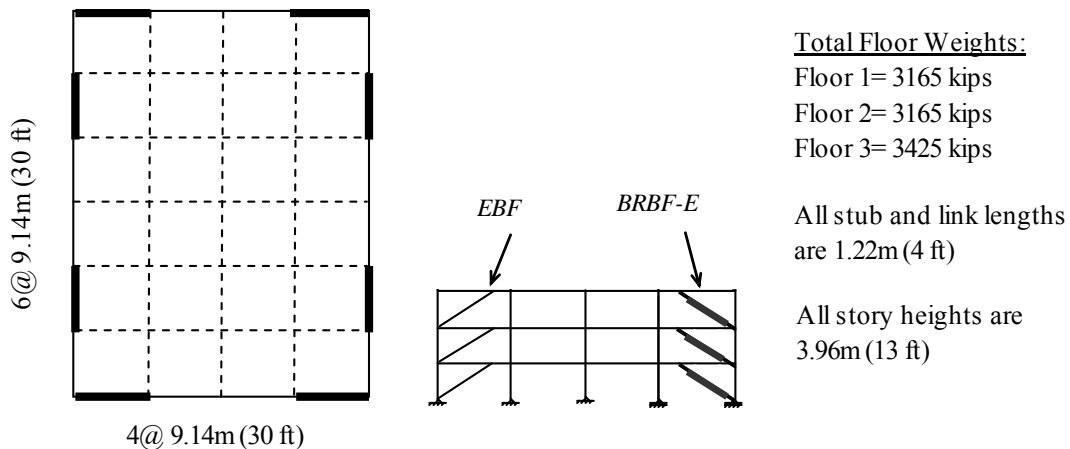
Fig. 3-21 Frame configurations, dimensions, and floor weights for the 3-story prototype building

76
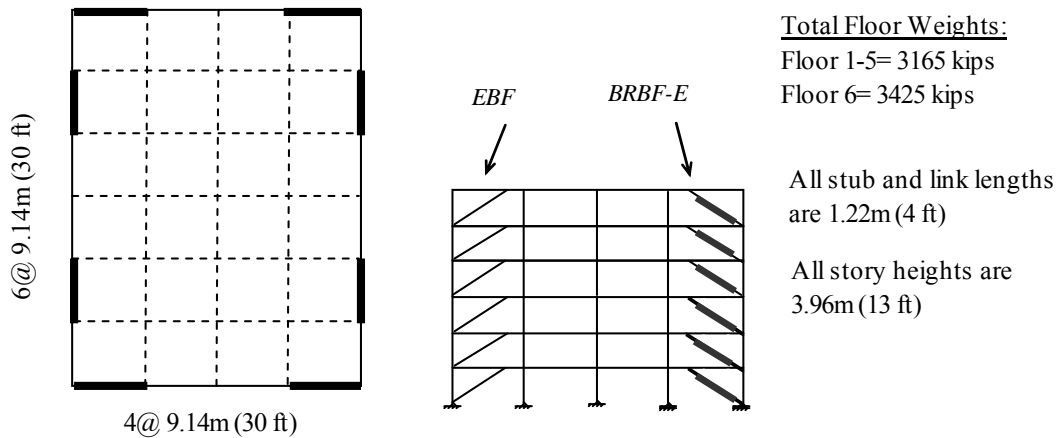
Fig. 3-22 Frame configurations, dimensions, and floor weights for the 6-story prototype building

Table 3-12 Equivalent Lateral Story Forces for BRBF-Es and EBFs

| | Equivalent Lateral Force (kips) | | | |
| | 3-Story | | 6-Story | |
Floor	BRBF-E	EBF	BRBF-E	EBF
1	60.0	48.5	22.4	11.5
2	120.3	102.4	48.6	28.3
3	195.2	171.4	76.4	47.9
4	--	--	105.4	69.7
5	--	--	135.2	93.1
6	--	--	179.3	127.8

3.8.3. BRBF-E and EBF Designs

The BRBF-Es for the 3- and 6-story buildings were designed using the procedure outlined in section 4.1, and the EBFs were designed using codified procedures outlined in [25]. To simplify design and future construction, the BRBF-E stubs and EBF links were repeated every three stories (allowing the same brace orientation and brace connection details between floors). Table 3-13 and Table 3-14 show the resulting BRBF-E and EBF member sizes for the 3 and 6-story building designs respectively.

77

Table 3-13 EBF and BRBF-E Member Sizes for 3-Story Designs

| Member | Shape (U.S. designation) or BRB Area (in2) | |
	EBF	BRBF-E
BM1-BM3[a,b]	W14x53	W27x102
BR1[c]	W12x79	9.0
BR2	W12x79	7.5
BR3	W12x79	5.0
CL1-CL3[d]	W14x61	W24x162
CR1-CR3[e]	W14x120	W24x162

a. BM1 is stub or link at first story, BM2 is stub or link at second story…
b. All stub or links are 4 ft long
c. BR1 is first story brace, BR2 is second story…
d. CL1 is first story left column, CL2 is second story…
e. CR1 is first story right column, CR2 is second story…

Table 3-14 EBF and BRBF-E Member Sizes for 6-Story Designs

| Member | Shape (U.S. designation) or BRB Area (in2)[a] | |
	EBF	BRBF-E
BM1-BM3	W14x82	W21x201
BM4-BM6	W14x48	W21x166
BR1	W14x109	13.5
BR2	W12x120	13.0
BR3	W12x120	11.5
BR4	W12x120	10.0
BR5	W12x79	7.5
BR6	W10x60	4.5
CL1-CL3	W12x96	W14x426
CR1-CR3	W14x159	W14x426
CL4-CL6	W10x49	W14x257
CR4-CR6	W12x106	W14x257

a. See notes from Table 3-13

3.8.4. Modeling and Analysis

Similar to the comparison study, the EBF and BRBF-E designs were modeled and dynamically loaded using ten earthquake ground accelerations. Modeling of the BRBF-E and EBF designs was performed in OpenSEES, and followed the same techniques discussed earlier in the comparison study. Similar to the comparison study, the response spectrum for each ground motion was scaled to match the design spectrum at the fundamental period of the frame. Table 3-15 lists the earthquake record and scale factor for all ten ground accelerations.

Table 3-15 Ground Motions and Scale Factors for Design Example Frames

| | | | | Scale Factor | | | |
| | | | | BRBF-E | | EBF | |
Record	PGA[a] (g)	R[b] (km)	Site[c]	3-Story	6-Story	3-Story	6-Story
1989 Loma Prieta							
47381 Gilroy Array No.3, LOMPAP/GO3090 [d]	0.37	14.40	D	1.70	1.00	1.20	0.79
57382 Gilroy array No. 4, LOMPAP/GO4090	0.21	16.10	D	1.30	0.95	1.25	0.77
1028 Hollister City Hall, LOMAP/HCH090	0.25	28.20	D	1.40	0.95	0.67	1.15
1656 Hollister Diff Array, LOMAP/HDA255	0.28	25.80	D	0.81	1.00	0.70	1.60
1695 Sunnyvale-Colton Ave., LOMAP/SVL360	0.21	28.80	D	2.50	1.50	2.10	1.30
1994 Northridge							
90053 Canoga Park, NORTHR/CNP196	0.42	15.80	D	0.62	1.00	0.70	0.55
90014 Beverly Hills-12520 Mulhol, NORTHR/MU2125	0.44	20.80	C	1.34	1.70	1.54	2.80
24278 Castaic - Old Ridge Route, NORTHR/ORR090	0.57	22.60	B	0.92	0.90	0.56	0.75
24088 Pacoima Kagel Canyon, NORTHR/PKC360	0.43	8.20	B	0.61	2.85	0.66	1.02
90021 LA-N Westmoreland, NORTHR/WST000	0.40	29.00	D	2.40	0.90	2.80	2.40

a. Peak Ground Acceleration

b. Distance to fault rupture

c. NEHRP Site class

d. Designation in Pacific Earthquake Engineering Research (PEER) database

3.8.5. Dynamic Analysis Results

The following section presents the inter-story drift results for the EBF and BRBF-E designs. Individual and average maximum story drifts for each design, due to each of the ten earthquake ground motions, are presented.

3.8.5.1. Peak Inter-Story Drift

The 3-story EBF and BRBF-E designs performed well under dynamic loading. Fig. 3-23 shows the maximum inter-story drift results for the 3-story EBF and BRBF-Es with link-to-column and stub-to-column configurations. In Fig. 3-23, the EBF story drifts are concentrated in the lower story, with the average maximum first story drift being 77% larger than the average maximum third floor drift. This is somewhat expected, given the extra link capacity at the second and third floor from the repeated first floor beam size. In contrast to the EBF drifts, the average BRBF-E drifts increased in the upper stories, resulting in 62% higher drift at the roof than in the first story. Although drifts were concentrated in the first story for the EBF, and in the roof for the BRBF-E, both designs performed well, responding with story drifts less than 2%.
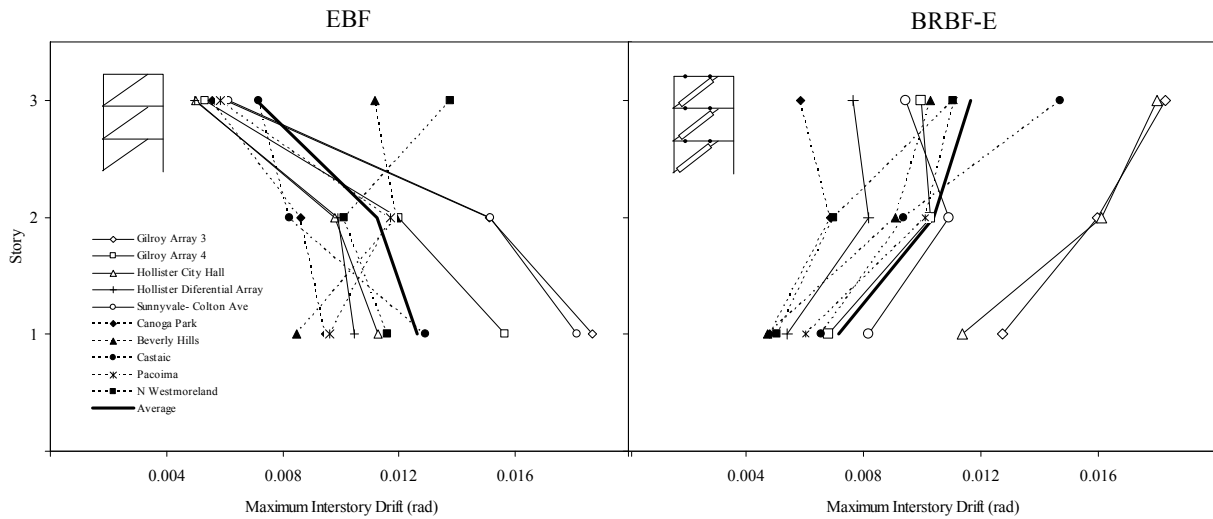
Fig. 3-23 Maximum inter-story drift for 3-story EBF and BRBF-E

The benefit of the BRBF-E over the EBF is more apparent in the 6-story frames than in the 3-story frames. Fig. 3-24 shows the individual and average inter-story drift values for the 6-story EBF and BRBF-E frames. In Fig. 3-24, EBF story drifts are concentrated in first and fourth floor, with the highest drift values occurring at the fourth floor. While the average maximum story drift in the 6-story EBF is less than 2%, the distribution of story drift is undesirable. The EBF drift concentrations in the first and fourth floors are expected, since the 6-story EBF design repeated the links every 3-stories. The average maximum BRBF-E story drifts are more uniform than the EBF, ranging from 0.6% in the first floor, to 1% at the roof, with values for intermediate stories in-between (see Fig. 3-24).
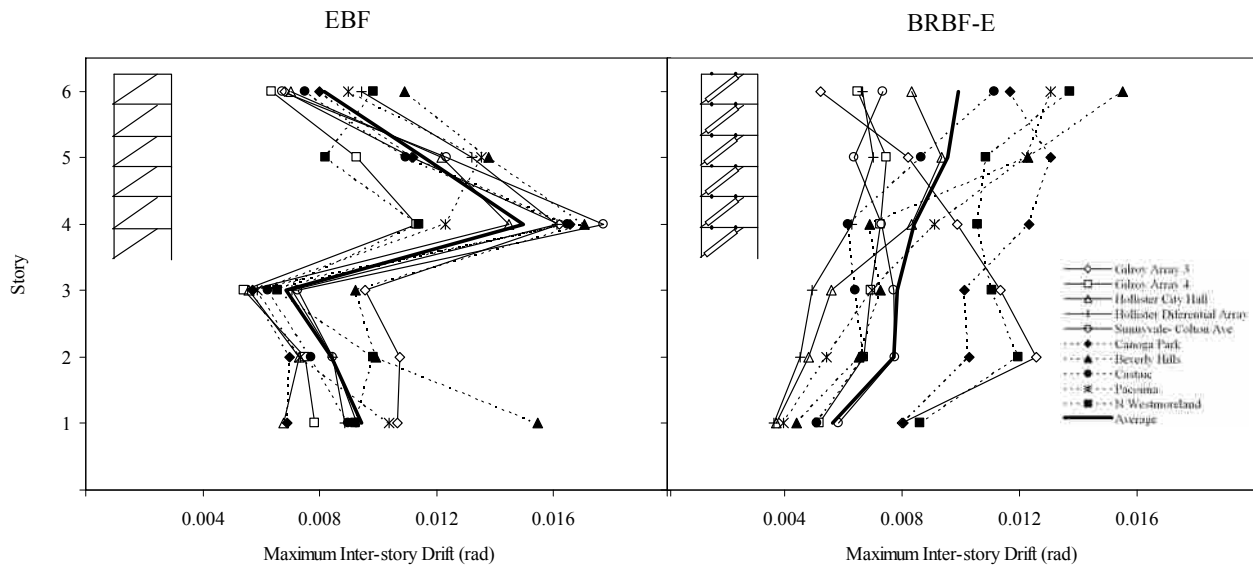
Fig. 3-24 Maximum inter-story drift for 6-story EBF and BRBF-E

3.8.6. Weight Comparison

The weight results for the frames in the design example are similar to those presented earlier in the comparison study. Fig. 3-25 shows the total frame weights and component weights for each EBF and BRBF-E designed in the design example. From Fig. 3-25, the 3-story BRBF-Es and EBFs have similar total frame weight, and the 6-story BRBF-E weighed near double that of the 6-story EBF (similar to weight distributions from the comparison study). By repeating the EBF beam sizes throughout the frame height, the 3- and 6-story frame beam weights increased by 330lb and 240lb respectively. This indicates that repeating EBF beam sizes every few floors has little effect on frame weight.

81
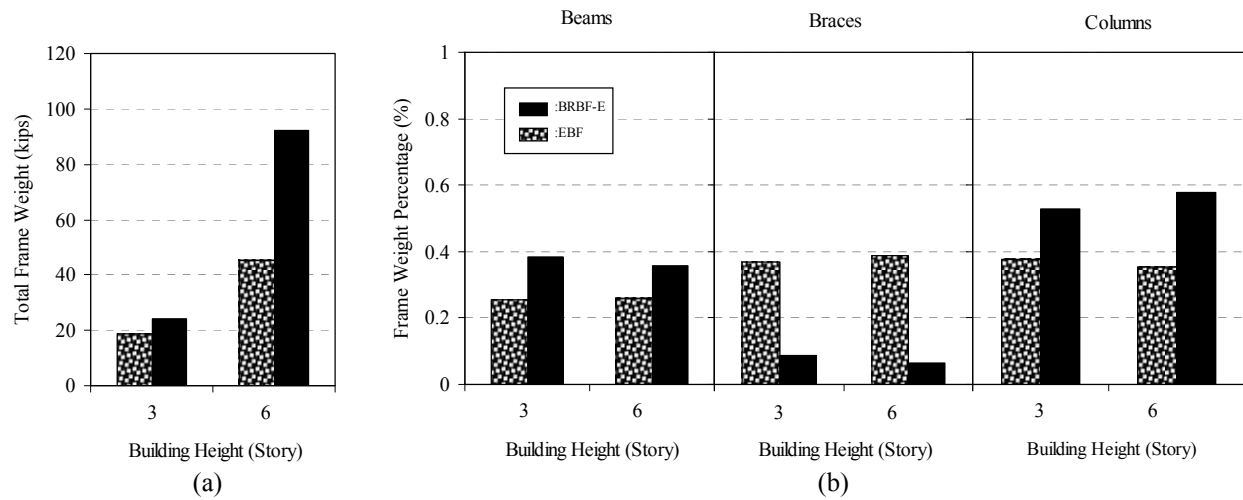
Fig. 3-25 (a) Total frame weights; and, (b) normalized component weights for the 3- and 6-story EBF and BRBF-E designs

3.9. Summary and Conclusions

In this study, the design and seismic performance of buckling-restrained braced frames in eccentric configurations (BRBF-Es) were compared with traditional EBFs. Design considerations for BRBF-E members were developed and BRBF-Es were designed, having strengths similar to code designed EBFs. Twelve BRBF-E and twelve EBF designs were dynamically loaded using multiple design-level ground motions and the seismic performance of each frame type was compared. A ten step design procedure for BRBF-Es was presented and a design example compared EBF and BRBF-E designs having repeated beam sizes.

The following conclusions regarding BRBF-E design and performance are based on 28 frame designs and 244 dynamic analyses of 3-, 6-, and 9-story BRBF-Es and EBFs. The work presented in this chapter suggests the following:

1. BRBF-Es offer a simple alternative to EBFs, especially EBFs with link-to-column connections.

82

2. BRBF-E designs are heavier than EBF designs, with the majority of the BRBF-E weight located in the columns due to the large axial and moment demands.

3. The performance of BRBF-Es is similar to that of typical EBFs. Under dynamic loading and when designed with equal strength, the BRBF-E frame drifts were similar to EBF frame drifts.

4. When designed with repeated beam sizes for better design economy, EBF frame drifts became concentrated within specific floors, while the BRBF-E frame drifts remained more uniform between floors.

5. BRBF-E seismic column demands in the lower stories of taller frames were between 70-80% of the design column demands.

6. Yielding in the BRBF-Es can be isolated to the brace elements by using the design procedures presented in Section 4.1.

Chapter 4: SYSTEM-LEVEL MODELING AND PERFORMANCE OF BRBF-Es SUBJECTED TO MULTI-DIRECTIONAL DYNAMIC LOADING

In the previous chapter system-level BRBF-E behavior was determined using two-dimensional beam and truss element models with inelastic fiber sections. In such models, added stiffness from gusset connections, and localized frame behavior (i.e.; local buckling, localized material yielding, and material fatigue) could not be determined precisely. In addition, the concrete slab and concrete slab-to-beam connection effects were not considered.

This chapter investigates both the system and component behavior of BRBF-Es under multi-directional dynamic loading, including concrete slab effects. The chapter begins with the introduction, discussing the limitations and benefits of various modeling techniques. Following, a description of a BRBF-C control model used to validate various modeling techniques is presented. Next, modeling techniques are described, and two test BRBF-E models are discussed. Lastly, results from multi-directional dynamic loading of the control model and BRBF-E models are presented, and BRBF-E connection demands are quantified and discussed.

4.1. Introduction

Traditional dynamic analyses of steel buildings predict structural response using either elastic beam and truss elements with lumped plasticity, or nonlinear beam elements with inelastic fiber sections ([4], [23], [22], and the analyses in Chapter 3 for example). The lack of precisely defined frame geometry in such models makes it difficult to predict localized frame damage such as member local buckling and gusset or weld connection stresses, and added stiffness from

gussets and panel zones is difficult to simulate. Additionally, analyses using lumped plasticity require inelastic behavior to be determined prior to analysis, which often require experimental testing and time-consuming element development whenever new connections or members are proposed.

Dynamic analyses using shell elements, although less common due to their computational expense, need only frame geometry and material behavior to predict frame component damage. Explicitly modeling frame geometry with shell elements allows for local buckling and determination of material fatigue [24]. In a study by Richards and Prinz [24], system-level frame response of shell element models was similar to that of traditional beam element models with lumped plasticity; however, determination of localized stresses and strains in the shell element models allowed for low-cycle material fatigue predictions within the connection regions.

4.1.1. BRBF-C Control Structure

A five story BRBF-C building was designed and dynamically tested at the E-Defense Hyogo Earthquake Engineering Research Center, in Tokyo, Japan in 2009. The building incorporated BRBs in both directions and was constructed having concrete slabs at each floor. The bay dimensions, and floor weights provided by E-defense [61] are given in Fig. 4-1. Construction details including details of member sizes and connections are presented in Appendix E. The dynamic loading of the test structure are discussed in Section 4.2.3.

| | 23 ft | 17 ft |
| F5: w = 326k |
| F4: w = 176k |
| F3: w = 185k |
| F2: w = 185k |
| F1: w = 190k |

(a) Y- Elevation   (b) X- Elevation

(c) Plan View
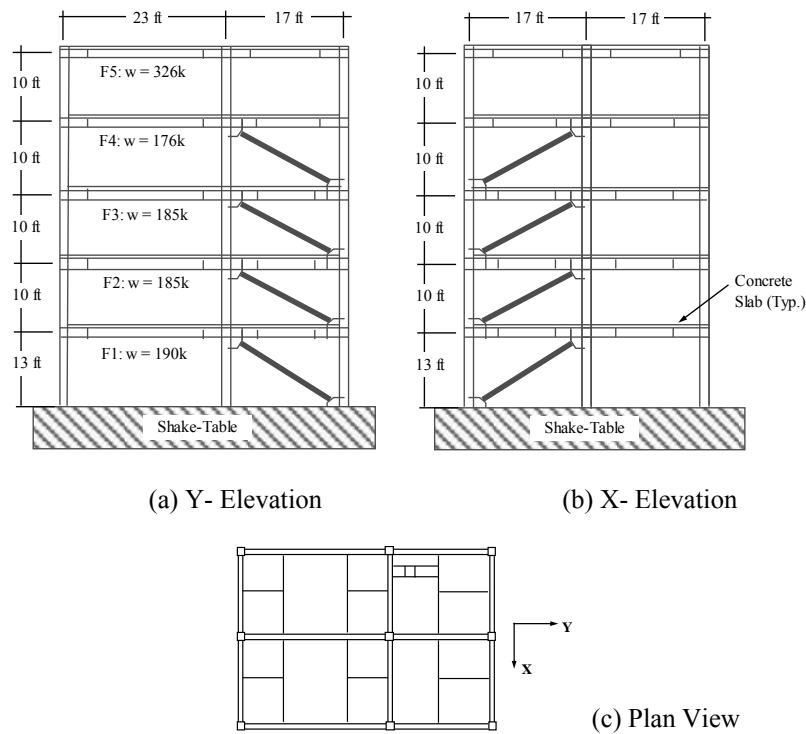
Fig. 4-1 Floor weights and frame dimensions for E-Defense test structure

4.2. Finite Element Modeling

4.2.1. Modeling Methods for Control Structure

4.2.1.1. General

A control model simulated the test setup and dynamic loading used by the 5-story E-Defense test structure. The control model was considered as a 3-dimensional system using ABAQUS [36]. Due to the lack of symmetry in the 5-story E-Defense structure, the entire building was considered. Fig 4-2(a) shows the 3-dimensional control model. The bases of the gravity columns in the control model were assumed to be pinned, while the bases of the seismic frames were assumed to be rigid. Floor masses were lumped at each column based on tributary floor area. Rather than incorporate rigid diaphragm constraints to transfer mass between the

columns, the concrete slabs were explicitly modeled. A description of the slab modeling techniques is provided later in Section 2.1.3.

Mesh size and element type affect the accuracy of analysis. The control model used four-node linear quadrilateral elements at a general mesh size of 6" (0.152 m). In regions of interest, regions with the highest potential for local buckling and stress concentrations, the mesh size was reduced to 3" (0.076 m) for improved strain accuracy. The mesh refinement was implemented near the connection regions, along the beams, and at the edges of the concrete slabs. In regions of little interest, near the middle of the concrete slab, the mesh was coarsened to an element size of 15" (0.381 m). The meshed model resulted in 131,959 elements. Fig 4-2(b) shows the meshed control model.

(a)   (b)
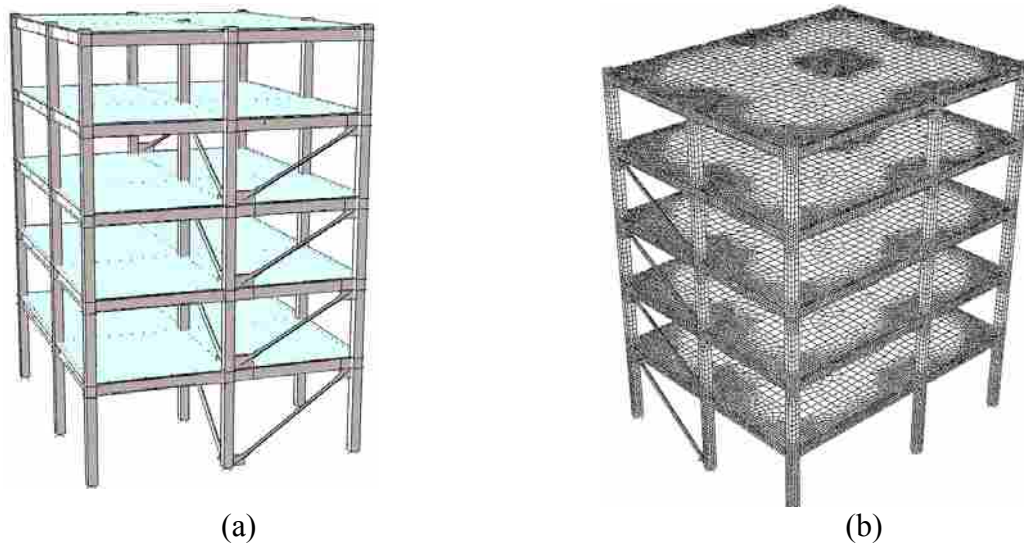
Fig. 4-2 (a) 3-dimensional ABAQUS control model of E-Defense test structure; and, (b) typical model mesh

Five percent stiffness proportional damping was specified in the first mode. All mass proportional damping was neglected. Equation 4-1 was used to calculate the stiffness proportional damping coefficient, β, used in the ABAQUS analysis:

88

$$\beta = \frac{2 \cdot \zeta}{\omega_i} \qquad\qquad (4\text{-}1)$$

In Equation 5-1, ω_i and ζ are the natural frequency at a given mode and damping ratio respectively.

To obtain the fundamental modes of vibration and natural frequencies used to calculate β, frequency analyses were conducted. Fig. 4-3 shows the frequency results for the first three modes of vibration for the control model, with corresponding natural frequencies. Considering five percent damping in the first mode, β of the control model was calculated as 0.0086.

For beams and columns, non-linear material properties and large displacement effects were considered in the analyses. Material plasticity for all beams and columns was based on a von Mises yield surface and an associated flow rule. Plastic hardening was defined using a nonlinear kinematic hardening law. Data from cyclic coupon testing of A572 Gr. 50 steel [37] (similar to A992 steel) was used to calibrate the material parameters. Steel coupon tests from the E-defense structure closely matched the steel material model. Large displacement effects were accounted for by utilizing the nonlinear geometry option in ABAQUS.
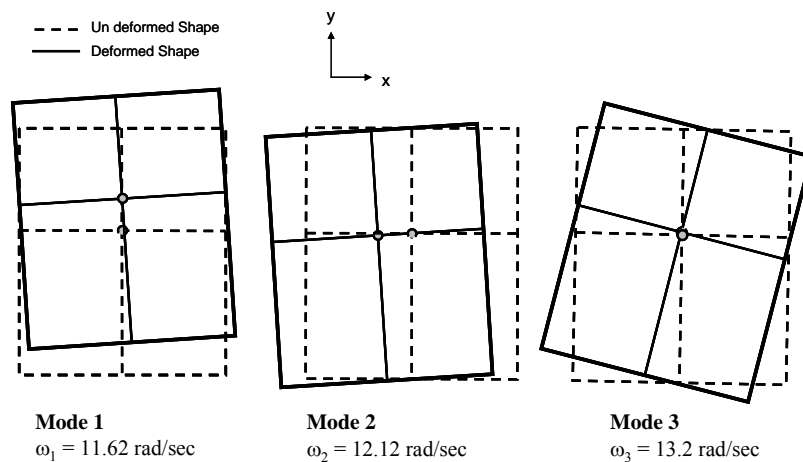
Fig. 4-3 First three mode shapes (plan view) and natural frequencies for BRBF-C control model

4.2.1.2. Buckling-Restrained Brace Specific

The buckling-restrained braces were explicitly modeled using shell elements. To simulate confinement of the brace core and prevent the brace from buckling out of plane, rotation constraints (both in and out of plane) were implemented along the brace core length (see Fig. 4-4). Based on a drift of 4%, the brace core was calculated to extend 4 inches out of the confining material; therefore, the rotation constraints were not implemented within 2 inches of the brace-gusset connection on either end. A multi-linear steel constitutive model developed by Coy [6] modeled the inelastic strength gain of the brace. Consistent with construction details provided by E-Defense, the brace-core yield strength was specified at 32 ksi.
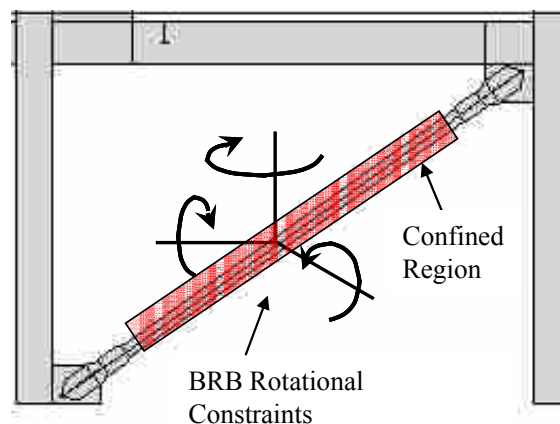
Fig. 4-4 Rotational constraints to simulate BRB confinement

4.2.1.3. Concrete Slab Specific

Shell elements and equivalent concrete material properties modeled the concrete slab. Modeling for the concrete slab followed techniques similar previous studies on composite moment frames [62,63]. Four-node isoperimetric shell elements located at the slab centerline defined the slab geometry. For simplicity, an elasto-plastic compression only constitutive model

with reduced concrete modulus and yield strength defined the concrete material behavior (similar to [62,63]). Calibration of the concrete constitutive behavior is presented in Appendix D.

Load transfer between the concrete slab and steel beam in a composite frame is primarily achieved through embedded stud connectors. For this reason, the interaction between the concrete slab and steel beam was modeled as a discrete connection using two linear springs and nodal displacement constraints (see Fig. 4-5 next page). Two spring elements (SPRING2 in ABAQUS) were oriented in the longitudinal and transverse beam directions to simulate the shear stiffness of a typical stud connector. A constraint joining the beam and slab nodes restricted relative vertical movement. The stiffness of the linear springs was calculated using typical stud properties in Equation 4-2 [62]:

$$K_S = \frac{0.9 \cdot G_S \cdot A_S}{L_S} \tag{4-2}$$

where K_S, G_S, A_S, and L_S are the spring stiffness, shear modulus of a typical stud, stud cross-sectional area, and stud length respectively.

4.2.2. Description of BRBF-E Test Models

Two additional models with brace eccentricities and beam splices were analyzed, representing BRBF-Es. The two BRBF-E models had different beam splice connection locations. The same modeling techniques used to model the braces, beams, slabs, and slab-to-beam connections in the control model, were used in the BRBF-E models. The brace geometry for the BRBF-E models was modified slightly from the control model, to form the eccentric brace connections. Brace areas in the BRBF-Es were modified to match the lateral story strength of the control model. Beam and column sizes were modified from the control model, to ensure

elastic response with the new brace geometry. Fig. 4-6 shows the BRBF-E brace geometry used

for both test models.

(a) Modeling techniques for beam-to-slab connection, 2-direction (Transverse direction)

(b) Modeling techniques for beam-to-slab connection, 1-direction (Longitudinal direction)

(c) Modeling techniques for beam-to-slab connection (Isometric view)
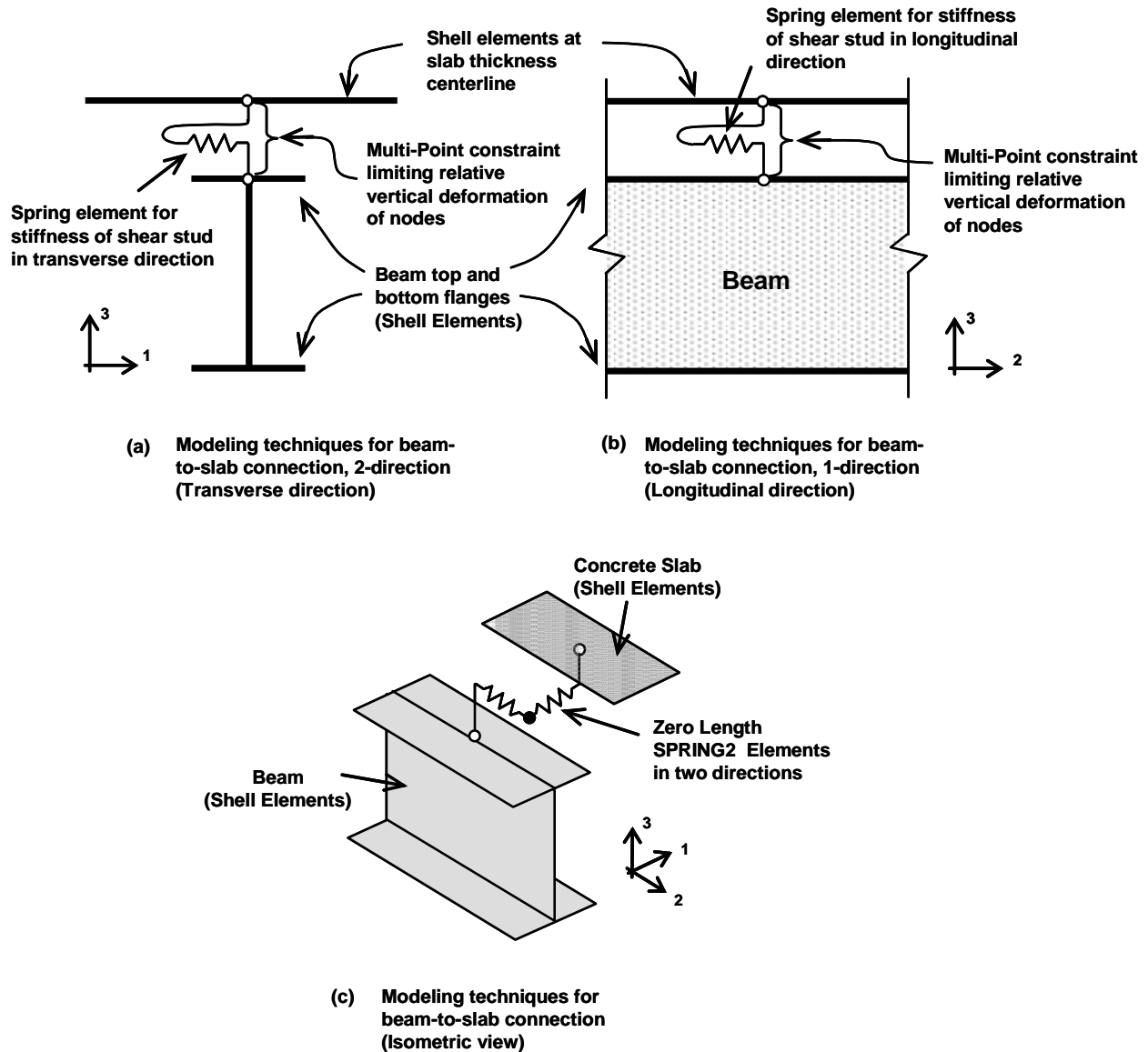
Fig. 4-5 Modeling technique for discrete beam-to-slab connection
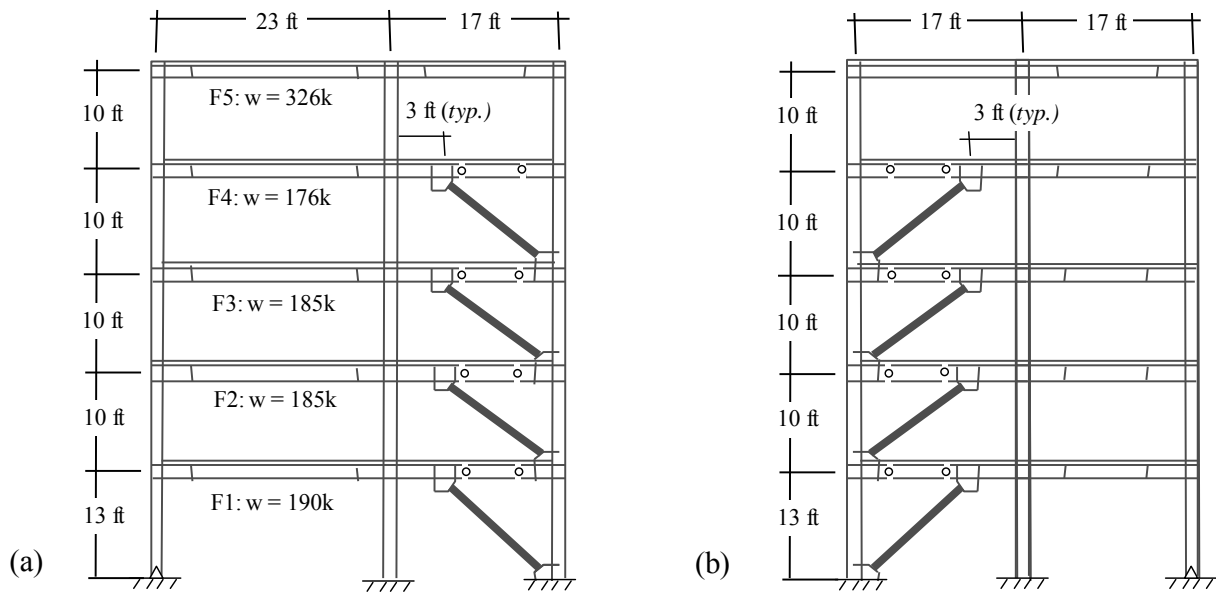
Fig. 4-6   Test model frame geometry for: (a) frames in Y-direction; and, (b) frames in X-direction

The first BRBF-E model, hereafter referred to as model MSC (mid-splice connection), used a beam splice connection in the middle of the beam, similar to the splice connection tested by Fahnestock, et al., [17]. To model the mid-beam splice connection, beam nodes were rigidly constrained to a reference node at the middle of the beam, and tied to the adjacent reference node on the other side of the cut using a hinge multi-point constraint (see Fig. 4-7). Modeling the beam splice connection as a perfect hinge was validated by Prinz and Richards [18].

The second BRBF-E model, hereafter referred to as model TSC (top-splice connection), used a beam splice connection at the top flange of the beam, similar to the connection tested by Coy [6]. Modeling the top-flange-splice connection is similar to that of the mid-splice connection; except the reference nodes are located at the beam top flange (see Fig. 4-8).
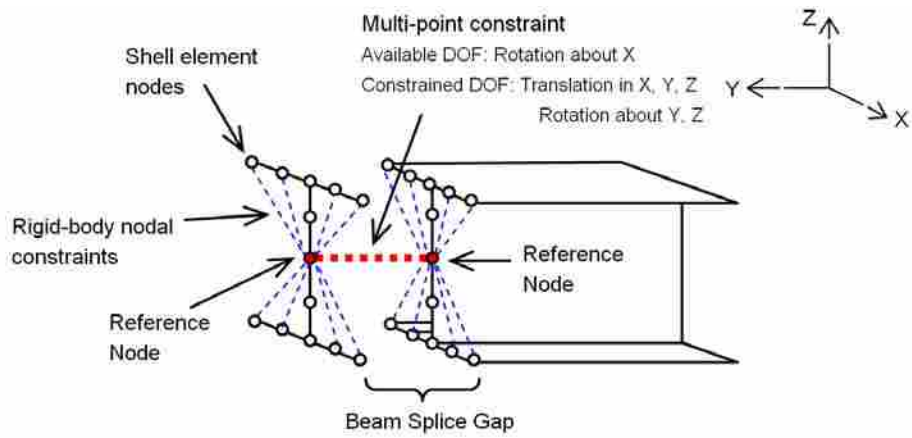
Fig. 4-7 Modeling of mid-beam splice connection (used in model MSC)
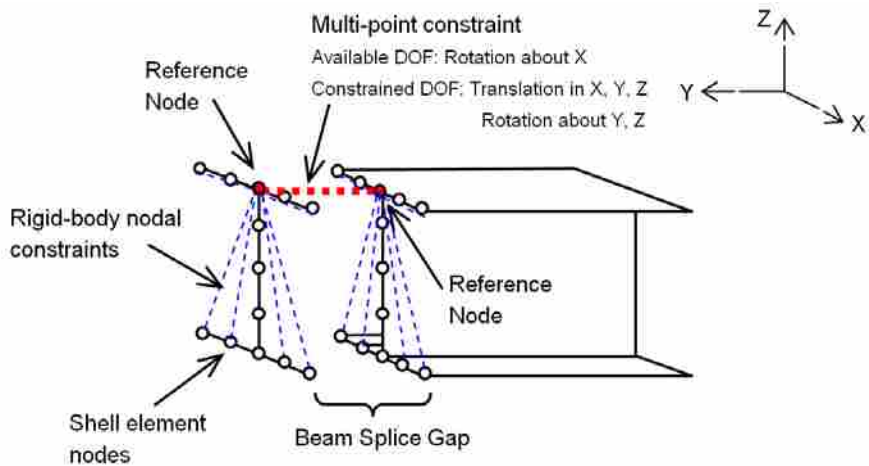
Fig. 4-8 Modeling of top-flange splice connection (used in model TSC)

Since the presence of a beam splice and modified brace geometry have the potential to affect the model stiffness, new damping factors needed to be determined. Similar to the control model, frequency analyses were conducted on each BRBF-E model to determine the natural vibration frequencies. Fig. 4-9 shows the first three mode shapes and corresponding natural frequencies for the two BRBF-E models. Considering five percent damping in the first mode, β was calculated as 0.0086 for both models MSC and TSC (this is the same value calculated for the control model).

94
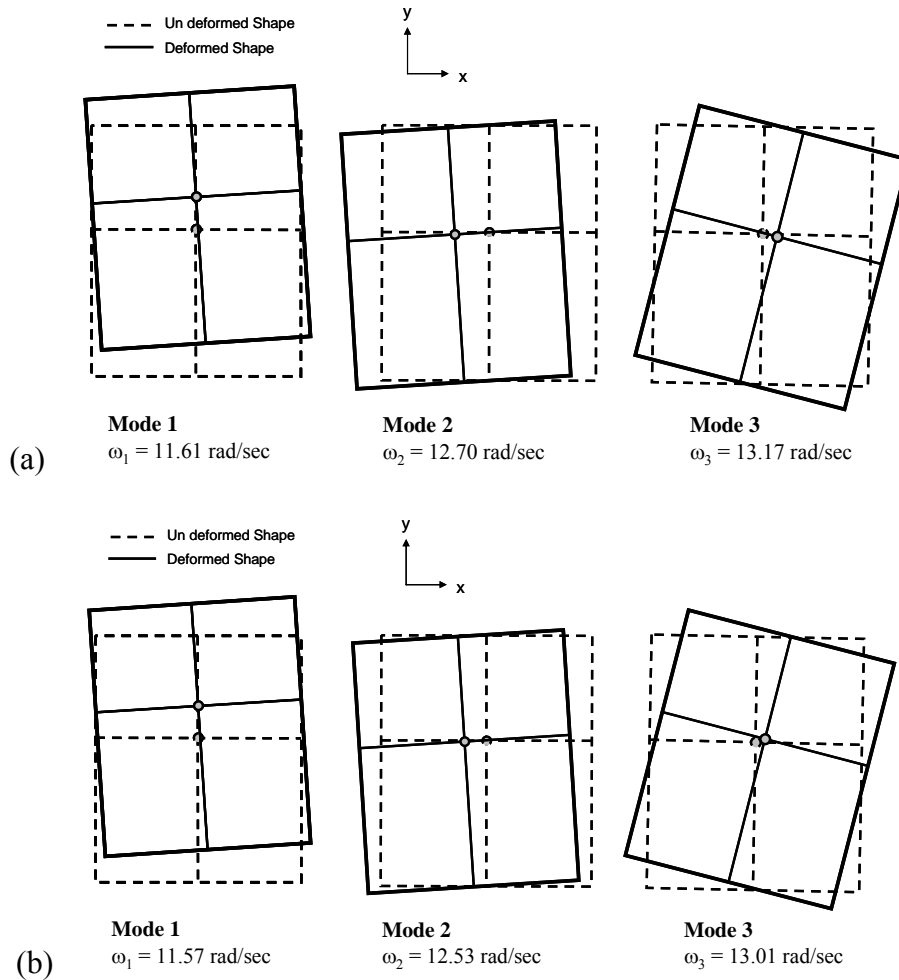
Fig. 4-9 Mode shapes and natural frequencies for: (a) model MSC; and, (b) model TSC

4.2.3. Frame Loading

The E-defense test structure, ABAQUS control model, and BRBF-E models were all dynamically loaded using accelerations derived from the 1995 Kobe earthquake (JR Takatori station). Acceleration components in both the North-South and East-West directions were applied simultaneously during analysis. An acceleration scaling of 1.0 times the recorded shake-table motion was used to directly compare the the control model and BRBF-E models with the E-defense test. Fig. 4-10 shows the target acceleration components recorded at the base of the shake table during the E-defense test.

95
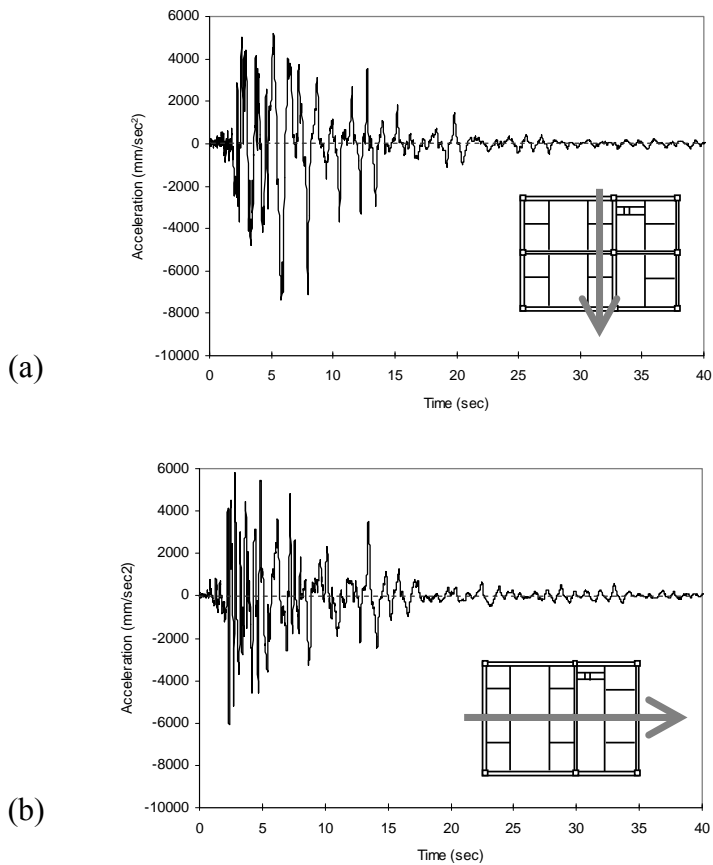
Fig. 4-10 Recorded E-defense shake-table motion for: (a) X direction acceleration component; and, (b) Y direction acceleration component [61]

4.2.4. Description of Computational Environment

The computational environment used for analysis consisted of six HP xw9300 workstations running a Linux operating system and joined on the Brigham Young University Computer Aided Engineering Design and Manufacturing (CAEDM) network. Each machine was equipped with an AMD Opteron 64 processor and 4 GB of memory. Four licenses of ABAQUS, each having five analysis tokens, were available for use.

All analyses were submitted to the CAEDM network batch cluster, which organized the efficient use of computer resources. Parallel computing was not utilized; rather, the analyses were performed on one machine at a time. The batch submission did however allow analyses to

search the network for available computer processors. In the CAEDM batch cluster, each analysis took approximately 168 hours (one week) to complete.

4.3. Control Model Validation

Comparisons of system and component responses (story drifts, displacements, accelerations, and column strains) between the E-defense test and control model provide reasonable confidence in the modeling methods and analysis procedures.

To demonstrate the system-level prediction capabilities of the simpler beam- and truss-element modeling methods, planar OpenSEES models representing the E-defense test structure were also created and analyzed under the same earthquake ground motions. Modeling techniques used for the 2-dimensional OpenSEES models were similar to those used in Chapter 3. Two OpenSEES models represented the braced bays in the X- and Y-directions.

4.3.1. Story Drift, Displacement, and Acceleration

Fig. 4-11 and Fig. 4-12 show the maximum absolute value of story drift and total relative story displacement respectively, for the E-defense test and control model. From the story drifts in Fig. 4-11, similar system behavior between the test and control model can be seen. The control model X-direction story drift values were within 15% of the E-Defense test, and control model Y-direction story drift values were within 15% for stories 1, 3, 4, and 5, and within 25% for story 2). Drift predictions from the OpenSEES models closely matched those of the control model, differing by only 5% on average, in the X- and Y-directions (see Fig. 4-11). The drift discrepancies in the lower stories (see Fig. 4-11) are partly due to the column-base boundary conditions assumed for the control model; the column-base fixity of the actual test was most likely in-between perfectly rigid and perfectly pinned.

97

Maximum X-direction story displacements between the test and control model differed by less than 0.1" in stories 2 through 5, and by less than 0.15" in the first story (see Fig. 4-12). In the Y-direction, maximum story displacements between the test and control model differed by less than 0.5" at all stories.
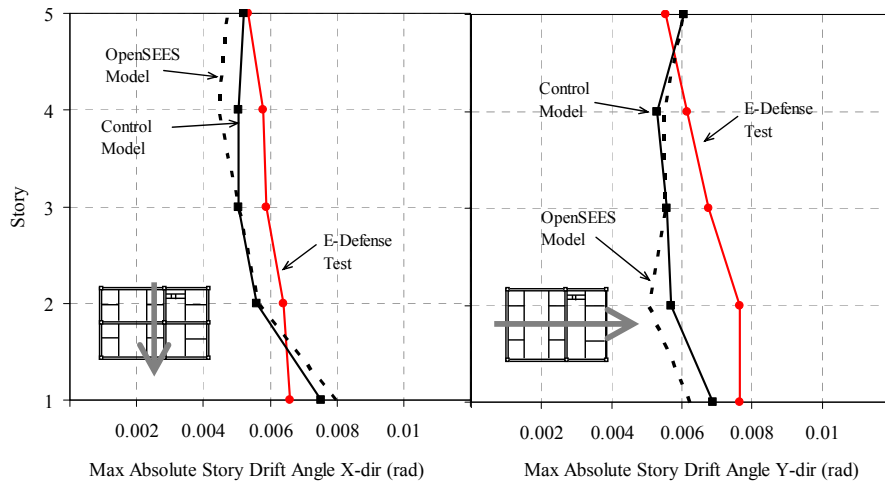
Fig. 4-11 Comparison of X-, and Y-direction inter-story drift between control model and E-Defense test
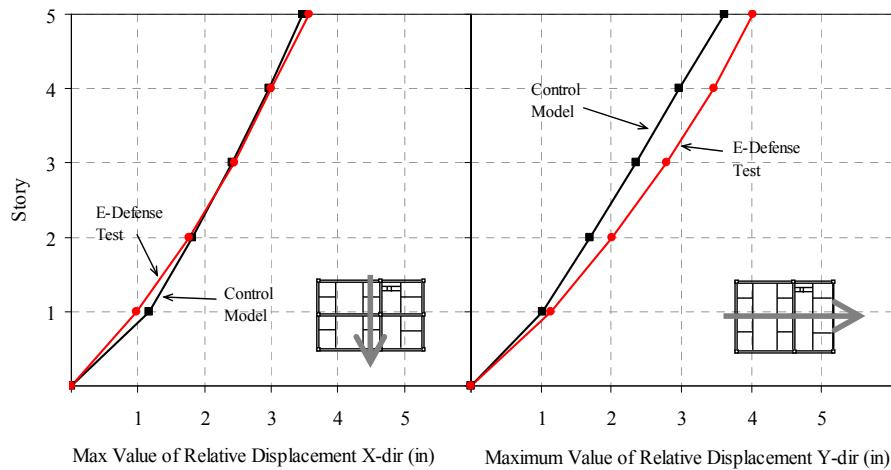
Fig. 4-12 Comparison of X- and Y-direction relative story displacements for control model and E-Defense test

Fig. 4-13 shows the maximum absolute story accelerations for the control model and E-defense test. Story accelerations for the control model were consistently lower than those

recorded during the E-defense test, averaging 21% lower in the X-direction, and 42% lower in the Y-direction. Although the story acceleration values are lower in the control model, the distribution of story shear appears to be relatively consistent with the experiment (note the shape of the control model and E-defense test story accelerations in Fig. 4-13).
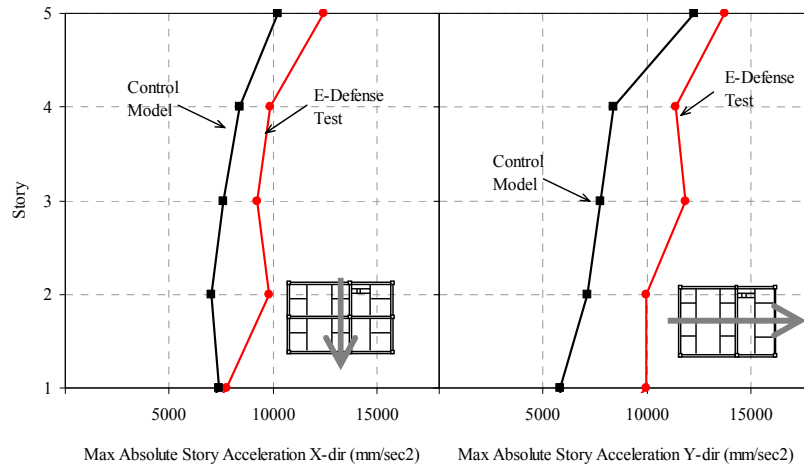
Fig. 4-13 Comparison of X- and Y-direction story accelerations between control model and E-defense test

4.3.2. Column Strains

The E-defense test was instrumented with several strain gauges, allowing localized member strains to be compared between the test and control model. Fig. 4-14 shows a given column strain gauge location within the test structure. Comparing the strain gauge readings with the control model strain calculations indicates that the control model adequately captured the local member behavior. Fig. 4-15 shows the strains in the first floor column for the E-defense test and control model. In Fig.4-15, the control model and E-defense test responses were 710 μ-strain and approximately 622 μ-strain respectively, resulting in less than 14.1% difference in column strain between the model and test.
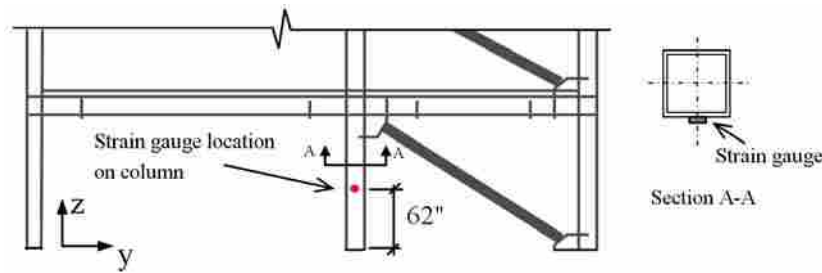
Fig. 4-14 Strain gauge location on column of E-defense test structure
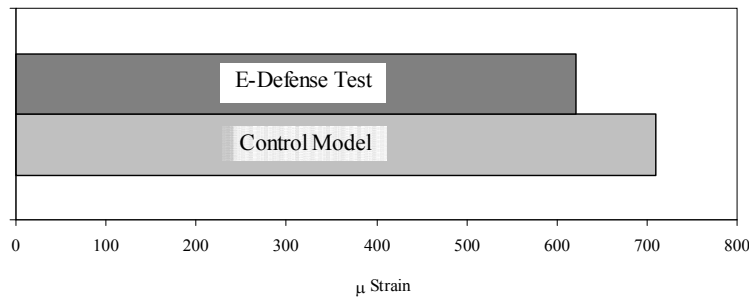
Fig. 4-15 Strain in first floor column of control model and E-defense test

4.4. Results for BRBF-E Test Models

The following results address the seismic performance of the two BRBF-E test models having different beam splice connections (models TSC and MSC). The discussion begins with system-level frame behavior such as story drifts, followed by local behavior, including beam-to-column and gusset connection stresses. Lastly, the performance of each splice connection is compared and a general description of concrete slab damage between the two models is presented. Most of the results for the BRBF-E test models are presented along with results from the control model to provide a reference of BRBF-C behavior.

4.4.1. Inter-Story Drift Angles

Inter-story drift values for the two BRBF-E test models were similar in value, and similar to drifts for the BRBF-C control model. Maximum inter-story drift angles for models TSC,

100

MSC, and the BRBF-C control model are shown in Fig. 4-16. Story drifts between model TSC and MSC were within 4% in the X-direction, and within 16% in the Y-Direction. In the lower stories of the Y-direction frames, drift values for model MSC were slightly larger than those for model TSC and the control model (0.001 rad larger at the base, see Fig. 4-16). Drifts between the BRBF-E models and the control model were reasonably similar, with the largest difference occurring in the first floor of the X-direction frames. First floor X-direction drifts for the control model were 0.002 rad larger than the drifts for models MSC and TSC.
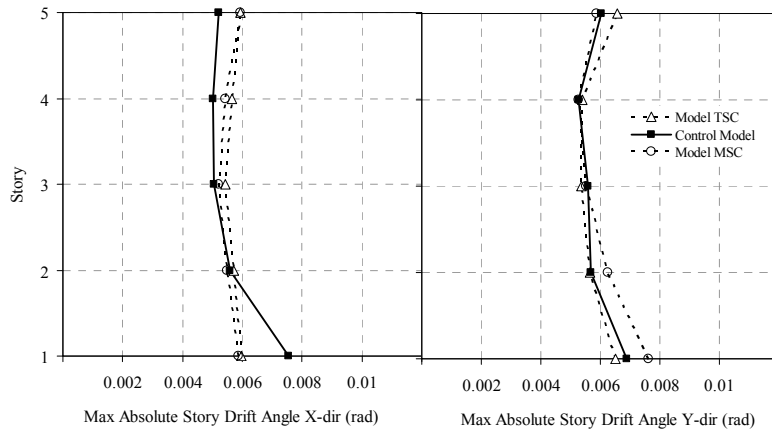
Fig. 4-16 Comparison of X- and Y-direction story drift for model MSC, model TSC, and the control model

The inter-story drift results shown in Fig. 4-16 are somewhat expected, given the results from the frequency analyses provided earlier. Mode 1 (Y-direction) frequency values for models TSC, MSC, and the control model were within 0.4% of each other (ranging from 11.57 rad/sec to 11.62 rad/sec), and mode 2 (X-direction) values for each frame were within 4.5% (12.12 rad/sec to 12.70 rad/sec). The control model had the lowest X-direction frequency (12.12 rad/sec, compared to 12.70 rad/sec and 12.53 rad/sec for models MSC and TSC, respectively) indicating lower stiffness and possibly explaining the larger first floor drift. Overall however, the relatively similar frequency values and drifts suggest similar stiffness between the BRBF-E and BRBF-C models.

101

4.4.2. Beam-to-Column Connection Stresses

The distribution of flange stresses between the BRBF-E test models and control model indicated stress concentrations near the BRBF-E stub-to-column connection. Fig. 4-17 shows the stress contours near the first story beam-to-column connection for the X-direction BRBF-E test models and control models. The stress concentrations near the flange-to-column connections of the BRBF-E models are from the increased beam bending moment caused by the brace eccentricity. With the BRBF-C model, the concentric brace connection reduced the beam moment, resulting in lower flange-to-column connection stresses. In EBFs, flange-to-column stress concentrations lead to early connection failure through material fatigue; however, unlike EBF beams, the stubs of the BRBF-E models didn't yield, eliminating the possibility for material fatigue.
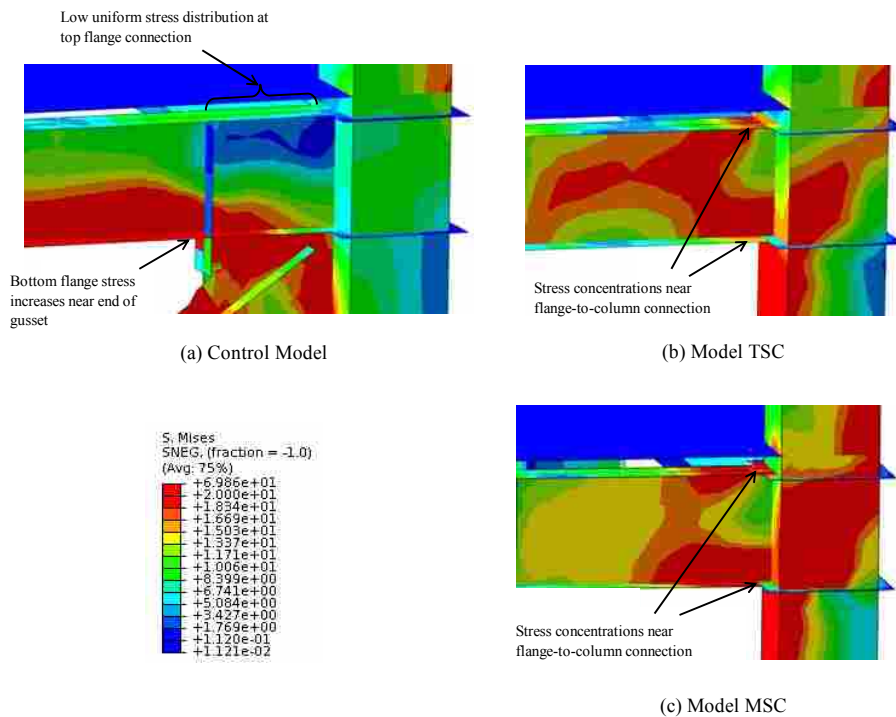
Fig. 4-17 First-story beam-to-column connection stress contours in X-direction frames for: (a) control model; (b) model TSC; and, (c) model MSC

Fig. 4-18 shows the top-flange von Mises stress values for the control model and BRBF-E test models. From Fig. 4-18, stress values near the flange-to-column connection of the BRBF-E models were higher than those of the control model. Flange connection stresses for the BRBF-E models were 4.5 times larger, on average, than the control model for the X-direction frames, and nearly 6 times larger for the Y-direction frames. The BRBF-E flange stresses away from the column connection reduced to values similar to the control model (see Fig. 4-18). The stress values were taken at the time-step corresponding to maximum frame displacement (time$_{y\text{-direction}}$=5.3sec, time$_{x\text{-direction}}$=8.1sec).
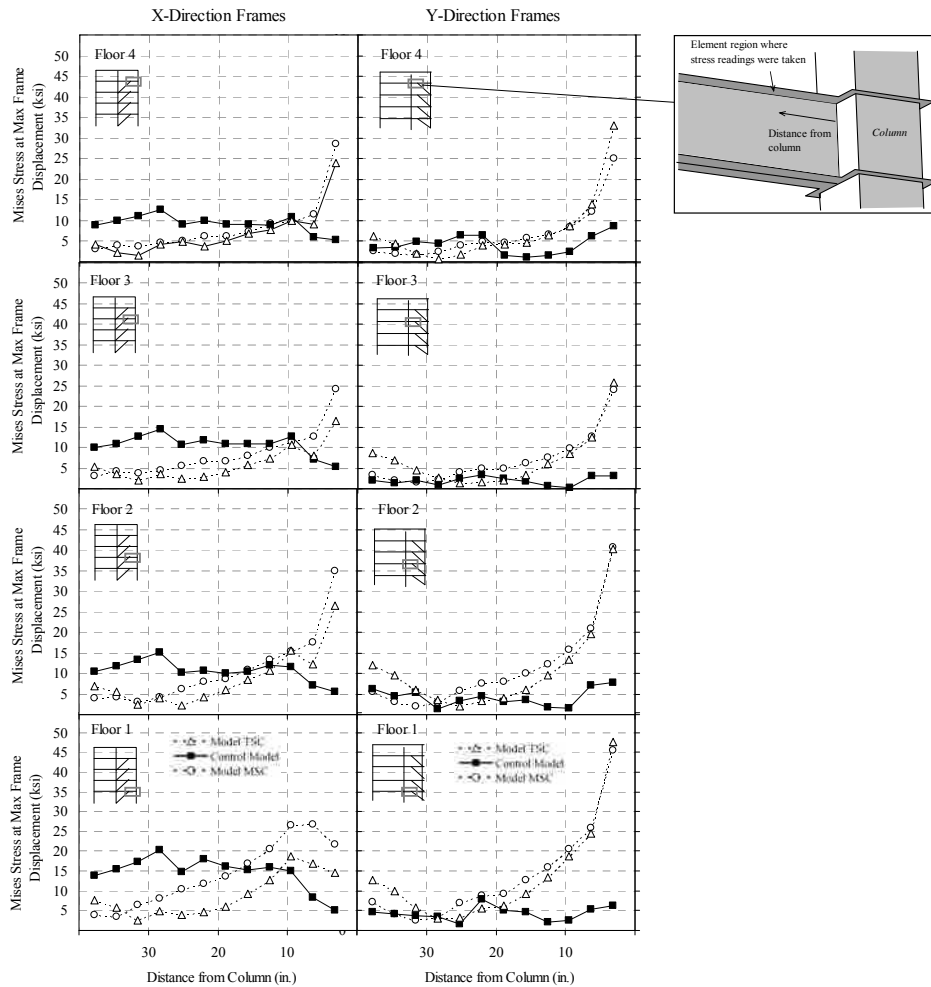
Fig. 4-18 Stress distribution in top flange of model MSC and TSC stubs, and control model beams.

4.4.3. Gusset Connection Stresses

Gusset-to-beam stress contours for the X-direction frames of models MSC, TSC, and the control model are shown in Fig. 4-19. The gusset-to-beam contours for models MSC and TSC in Fig. 4-19 are low and relatively uniform, with only a slight decrease in stress toward the beam splice, away from the column-edge of the gusset. The gusset-to-beam stress contours in the control model increased significantly away from the gusset column-edge (see Fig. 4-19(a)). This increase in gusset stresses away from the gusset column-edge is explained by changes in the beam-to-column connection angle (pinching and expanding the gusset region).

(a) Control Model

(b) Model TSC
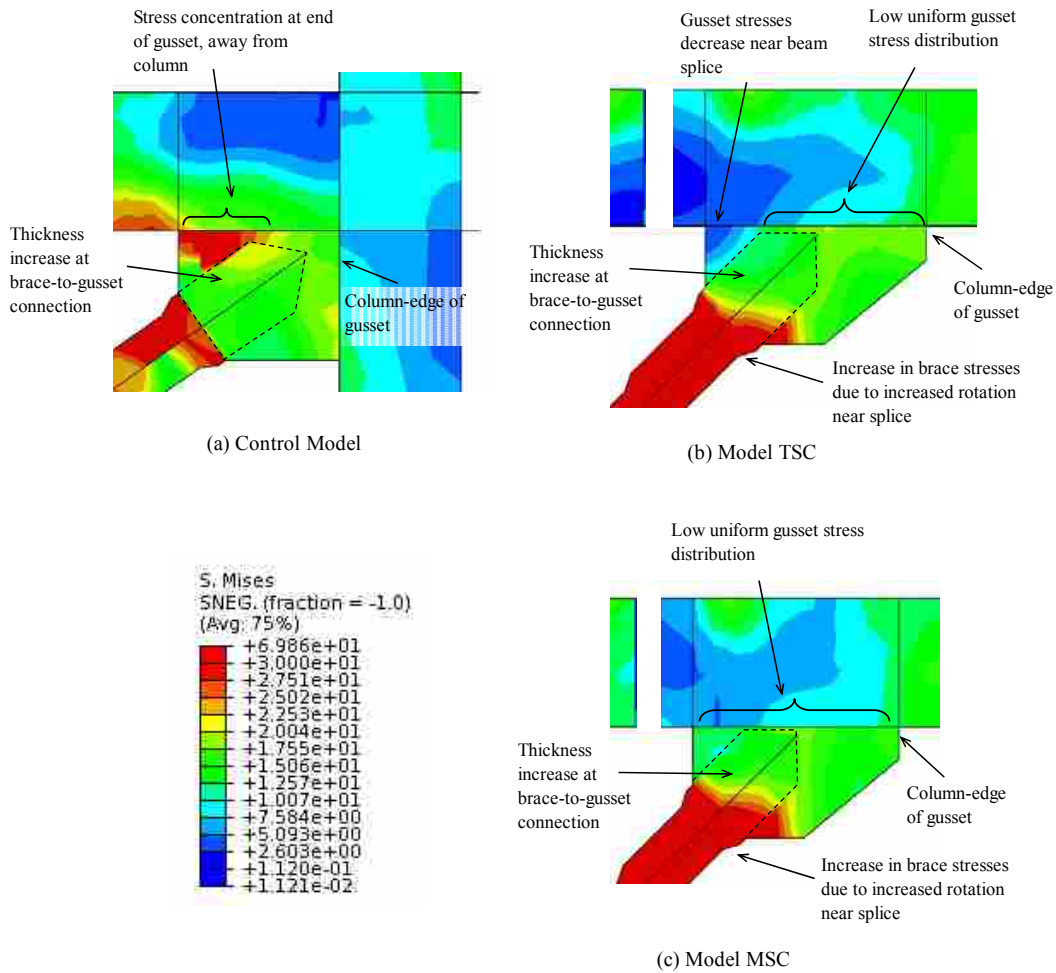
(c) Model MSC

Fig. 4-19 Gusset-to-beam stress contours for: (a) control model; (b) model TSC; and, (c) model MSC

Fig. 4-20 shows the distribution of stress values in the top gusset-to-beam connection for models TSC, MSC and the control model. The maximum gusset-to-beam stress values in the control model were near double those of the BRBF-E models (for the X-direction frames) (see left column of Fig. 4-20). As mentioned earlier, these larger gusset stresses in the BRBF-C control model are due to changes in the beam-to-column angle, resulting in pinching and expansion of the gusset plate. Since the BRBF-E models are only attached to the beams, changes in beam-to-column geometry have less effect on the BRBF-E gusset stresses. Gusset connection stresses for models MSC and TSC were similar in value, and rather uniform, in the X-direction frames. In the Y-direction frames, gusset-to-beam connection stresses for the control model and model TSC were similar and consistently higher than those for model MSC (see right column of Fig. 4-20). This result may be due to slight brace-end and gusset plate distortions (brace-ends and gussets in the lower stories of model TSC slightly distorted out of plane).

4.4.4. Comparison of Beam Splice Connection Performance

Although the beam-splice connections in models TSC and MSC were considered perfectly pinned (using hinged multi-point constraints), force couples between the slab and splice connection allowed the splice to carry moments. Fig. 4-21 shows examples of the force couples generated by the slab and splice connection for the mid-splice and top-flange splice connections. To compare the connection demands of each splice type, stress values were taken along the beam height for both the mid and top-flange splice connections. Stress values were taken at analysis time steps corresponding to maximum frame displacements ($time_{y-direction}=5.3sec$, $time_{x-direction}=8.1sec$). Fig. 4-22 shows the distribution of von Mises stress along the height of the beam at the beam splice. In Fig. 4-22, stresses in the bottom half of the beam for the top-flange splice connection are consistently lower than those of the mid-splice connection (63% lower on

105

average); however stresses at the top flange are higher in the top-flange splice than in the mid splice (40% higher on average). This is somewhat expected given that the force couple in the top-flange splice is closer together and acts closer to the top flange. Also, the magnitude of the beam-stress values is low for both models because of the low concrete slab capacity (compressive forces in the slab limit the forces that can develop at the splice).
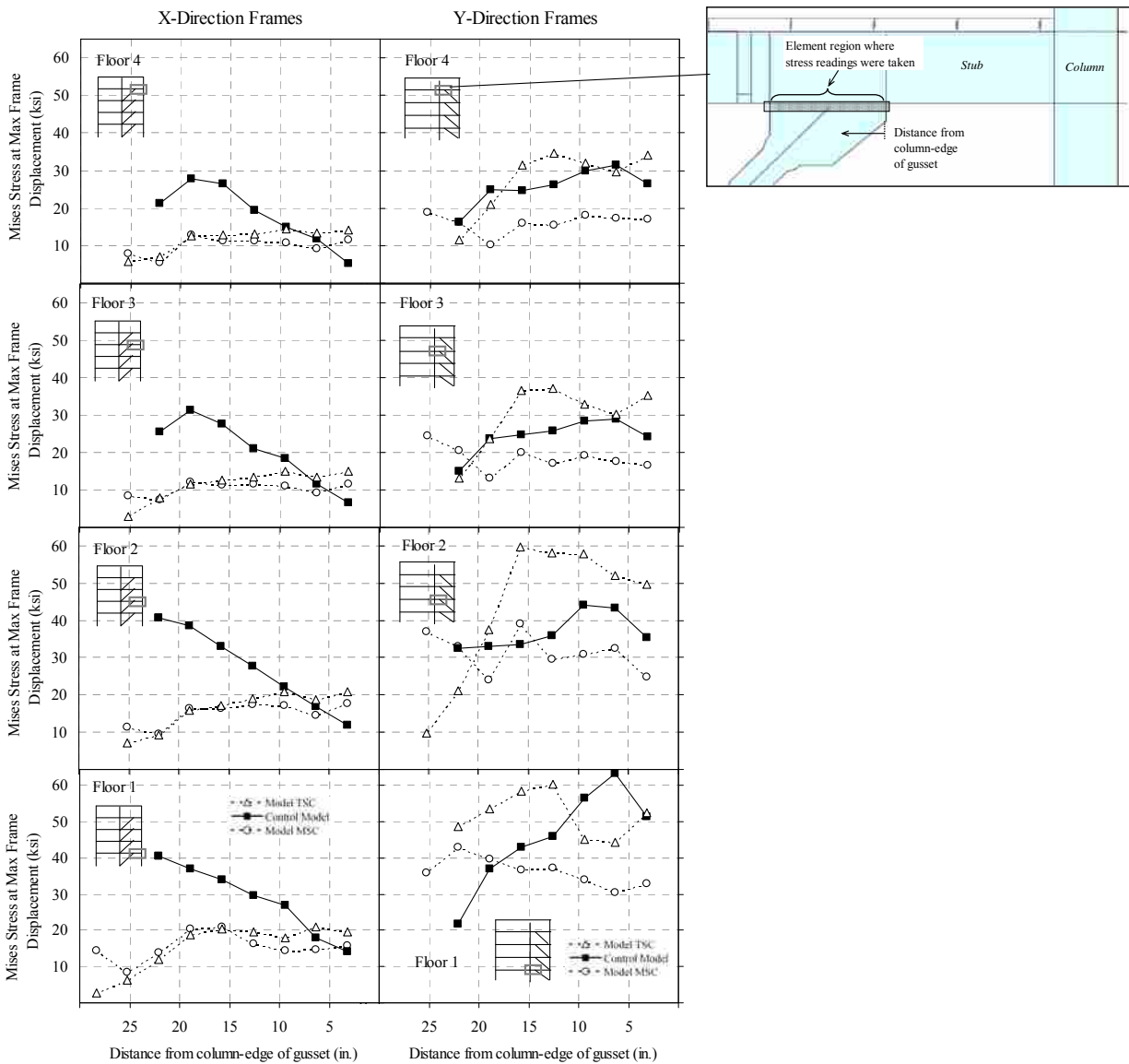
Fig. 4-20 Gusset-to-beam connection stress distributions for models MSC, TSC, and the control model
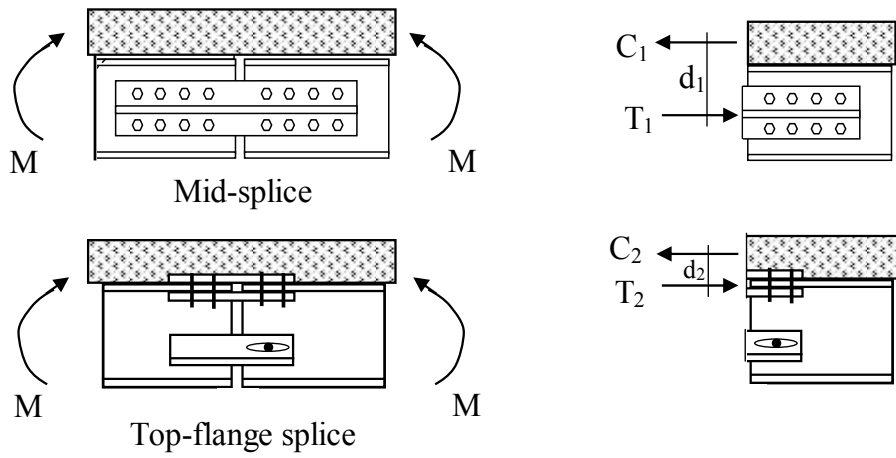
Fig. 4-21 Force couples generated from slab and splice-connection for both mid-splice and top-flange connections
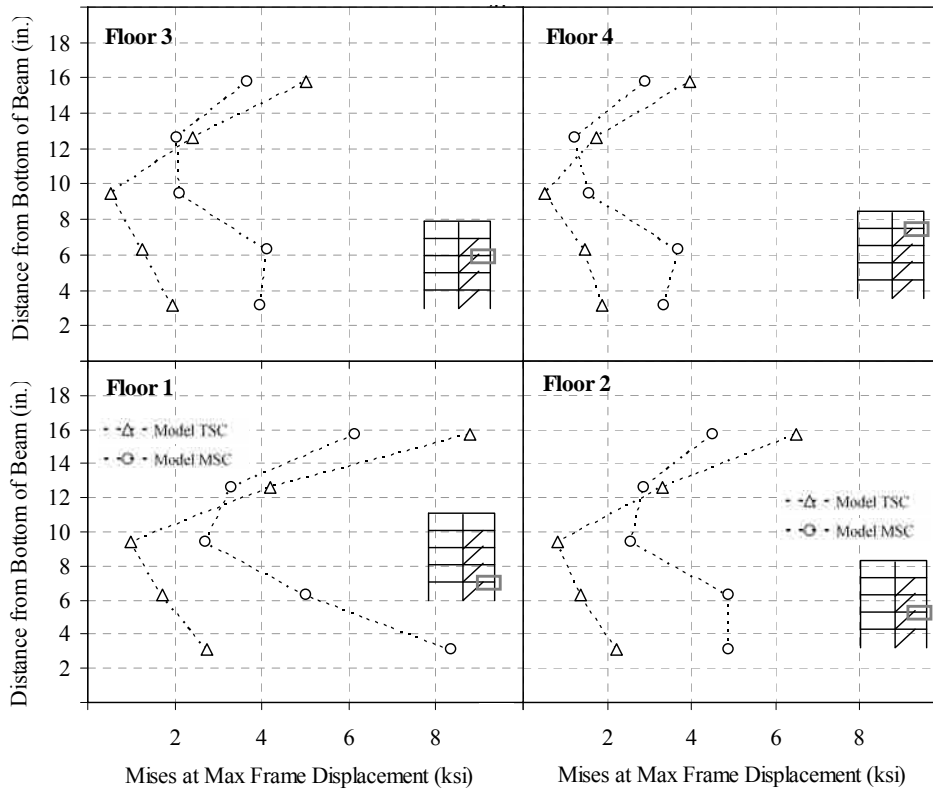
Fig. 4-22 Vertical stress distribution in beam at beam-splice connection (X-direction frames)

4.4.5. Concrete Slab Damage

Due to the simplified modeling techniques used for the concrete slab, prediction of actual slab damage (concrete crack formations, crack propagation, and rebar yielding) is not possible; therefore, in this section, the slab locations with the most slab "yielding" are highlighted and discussed. Fig. 4-23 through Fig. 4-25 show the accumulation of slab material yielding for model MSC, model TSC, and the control model respectively. Note that the discrete modeling technique for the slab-to-beam connection created stress concentrations in the slab, resulting in localized material yielding for all models.

Slab damage for model MSC occurred near the slab-to-beam connections, and was relatively well distributed along the beam length (see Fig. 4-23); slab damage for model TSC was concentrated near the beam-splices (see Fig. 4-24). This difference in slab damage can be explained by the connection force couples discussed earlier (refer to Fig. 4-21). The closer spacing of the force couple in model TSC allowed the top-flange splice connection to behave more like a pinned connection, reducing flexural deformations in the beam and concentrating slab damage near the hinge; the larger spacing of the force couple in model MSC allowed larger moments to develop in the beams, resulting in some flexural beam deformations and distributed slab damage. Slab damage for the control model was minimal and mostly concentrated near the columns and gusset connections (see Fig. 4-25). The majority of the slab damage for all models occurred in the lower stories above the beams in the braced frames, with little-to-no damage occurring above the beams in the gravity frames.
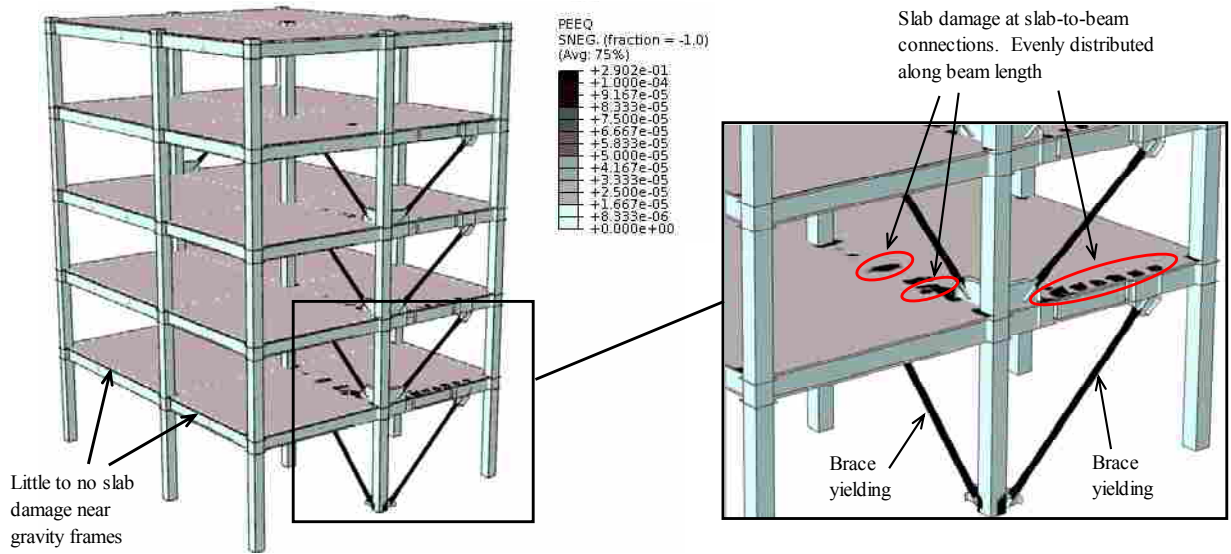
Fig. 4-23 Locations of slab damage for model MSC
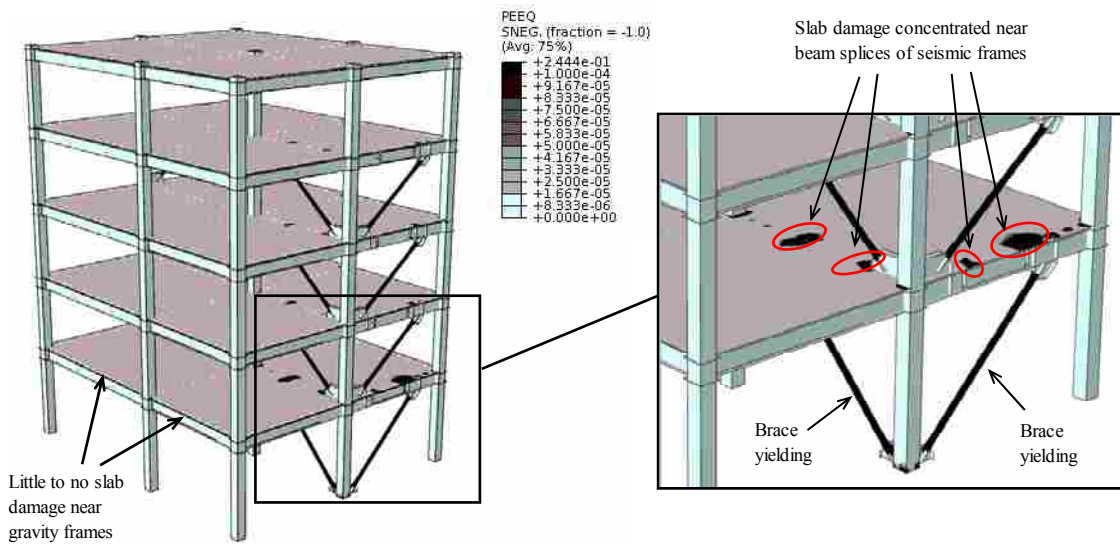
Fig. 4-24 Locations of slab damage for model TSC

109

PEEQ
SNEG. (fraction = -1.0).0)
(Avg: 75%)
+6.507e-01
+1.000e-05
+9.167e-06
+8.333e-06
+7.500e-06
+6.667e-06
+5.833e-06
+5.000e-06
+4.167e-06
+3.333e-06
+2.500e-06
+1.667e-06
+8.333e-07
+0.000e+00

Minimal slab damage concentrated
near gussets and columns

Brace
yielding

Brace
yielding
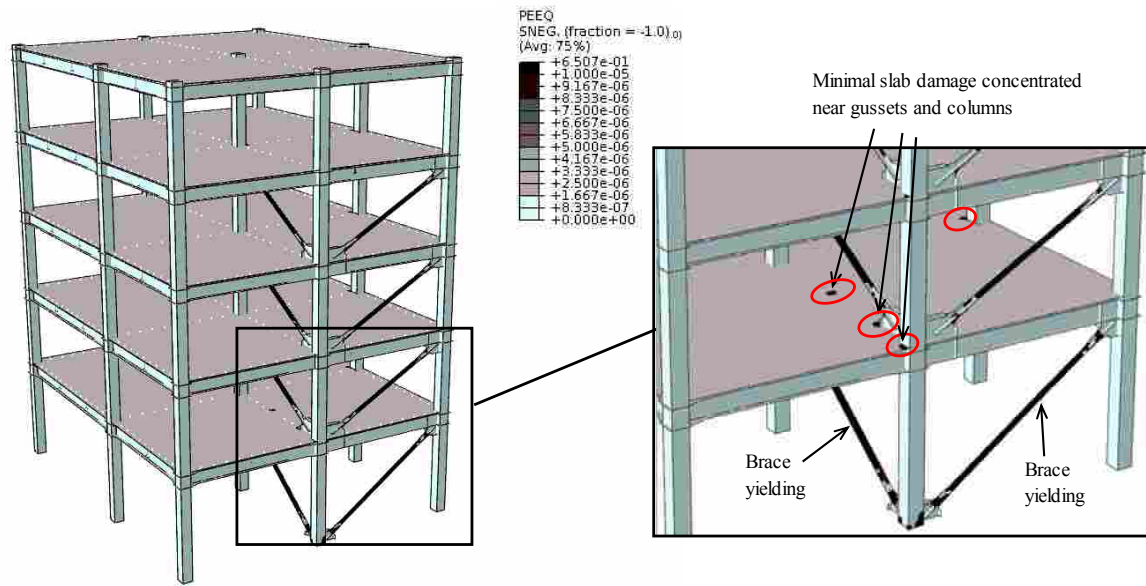
Fig. 4-25 Locations of slab damage for control model

4.5. Summary and Conclusions

In this chapter, multi-directional dynamic loads were applied to three finite element models representing one 5-story BRBF-C and two 5-story BRBF-Es. The geometry of the three finite element models was created using shell elements.   The BRBF-C model allowed for system-level validation of various modeling techniques, as well as comparison between BRBF-C and BRBF-E dynamic response. The two BRBF-E models were created with identical geometry, but different beam-splice connection types (top-flange and mid-splice connections), to help determine the effects of the beam splice location. The specific modeling techniques presented in the chapter included: modeling of the concrete slab, slab-to-beam connection, and buckling-restrained brace. The modeling methods allowed for determination of component connection stresses and strains, as well as system-level frame response. The following conclusions are from the component and system response of the three computer models:

110

1. Modeling composite beams with reduced elastic-perfectly-plastic concrete properties, and discrete slab-to-beam connections can reasonably predict system-level frame behavior.

2. System-level frame response from full-scale dynamic shake-table testing can be reasonably predicted using finite element models with beam and truss elements, and finite element models with shell elements.

3. System-level frame response for BRBF-Cs and BRBF-Es are similar, with similar story strengths, thus indicating similar system stiffness. Modal frequencies between BRBF-C control model and BRBF-E test models were similar.

4. BRBF-E stubs have stress concentrations at the beam-to-column connection similar to EBF link-to-column connections; however, elastic stub responses eliminate material fatigue concerns. The BRBF-E stub stress concentrations were 4-6 times greater than those in the BRBF-C beams.

5. Gusset-to-beam connection stresses for BRBF-Es are relatively uniform, and lower than those of the BRBF-Cs, when the brace-ends remain in-plane. The beam splices and eccentric location of the brace connections prevent gusset stress concentrations due to pinching and expansion of the beam-column joint (a common cause of failure in BRBF-Cs).

6. Due to the spacing between the slab and splice connection, top-flange splice connections similar to those tested by Coy [6] result in lower average connection stresses than mid-splice connections similar to Fahnestock et al. [17].

7. Top-flange splice connections result in higher, more localized slab damage than the mid-splice connections.

Chapter 5: CONCLUSIONS AND RELEVANT CONTRIBUTIONS

5.1. Summary and Conclusions

Ductile braced frame systems are commonly used to resist lateral earthquake loads in steel buildings; however, in certain cases the use of a braced frame system can interfere with architectural openings. One specific type of ductile braced frame system often used to accommodate architectural features is the EBF; however, the poor performance of EBF link-to-column connections limits the number of available economical EBF designs.

Recent testing highlights the limited ductility of EBF link-to-column connections, indicating reductions in link rotation capacity due to connection fractures. The current seismic provisions warn engineers of the issues with EBF link-to-column connections, and suggest avoiding the connections altogether until a practical solution is found.

Chapter 2 investigated the effectiveness of removing portions of the EBF link web and link flange, in an attempt to limit forces that could develop at the EBF link-to-column connections and thereby increase connection rotation capacity. Validated finite element models of several shear yielding links with web and flange cuts were analyzed under cyclic loading. Results indicate that introducing circular cuts into the link web was effective in reducing stress concentrations at the flange connections; however, the resulting stress concentrations at the edges of the web holes ultimately limited the link rotation capacity. Reducing the link web area moved the problem away from the flange connection and into the web. Introducing circular cuts in the link flange had little effect on link rotation capacity.

In Chapter 3, the focus of the research turned away from improving EBF link-to-column rotations, and focused on alternative frame designs that can accommodate architectural features. Design considerations for buckling restrained braced frames in eccentric configurations (BRBF-Es) were developed, and the seismic performance of several BRBF-E and traditional EBFs were compared. The comparison study consisted of 12 BRBF-E and 12 EBF designs. Planar finite element models were subjected to a suite of 10 scaled earthquake accelerations, resulting in a total of 244 dynamic analyses. Following the comparison study, a BRBF-E design example was presented, along with BRBF-E design procedures. The BRBF-E designs isolated damage within the brace region, and responded similar to the EBF designs under dynamic loading. Drifts and residual drifts between the EBF and BRBF-E designs were similar. When the BRBF-Es were designed with repeated beam sizes (for better design economy) drifts remained relatively uniform up the building height; however, the EBF designs with repeated beam sizes sustained large concentrated story drifts.

In Chapter 4, the BRBF-E investigation was taken to the next level by analyzing validated models (created using shell elements) under multi-directional dynamic loads. System level dynamic modeling techniques of ductile braced frames were validated using existing shake table testing. Modeling the frames with shell elements allowed BRBF-E component demands to be investigated, including gusset-to-beam connection demands, beam-to-column connection demands, and the relative performance of different BRBF-E beam-splice connection types. Results from the finite element models indicated similar drift and story displacement values between the control model and E-defense test. The system-level frame response for typical BRBF-Cs and the new BRBF-Es were also similar, indicating similar system stiffness between BRBF-Cs and BRBF-Es. Stress concentrations in the BRBF-E stubs at the beam-to-column

114

connection were similar to those noticed for EBF link-to-column connections; however, the elastic stub responses eliminated material fatigue concerns. Due to the smaller force couple between the slab and splice connection, the top-flange splice connections resulted in lower average splice connection stresses than the mid-splice connections.

With similarities in performance and configuration between BRBF-Es and EBFs, the advantages of the BRBF-E over the EBF are ease of design, ease of reparability, and economy. The BRBF-E was simpler to design than the EBF. With the BRBF-E, damage was isolated within the brace, and in the EBF, damage was isolated within the link, indicating simpler repairs with the BRBF-E. With construction accounting for the majority of a building project's cost, BRBF-Es may be more economical than EBFs, because they are easier to construct. Shop welding of BRBF-E members can replace the multiple field welds required in EBF construction.

5.2. Contributions to the Field of Structural Engineering

The following list represents the original contributions of the dissertation work.

1. Demonstrated the effects of web and flange area reductions on EBF link-to-column connection stresses and material fatigue.

2. Developed design considerations and design steps for BRBF-Es.

3. Performed 244 dynamic analyses on several EBF and BRBF-Es, developing drift profiles and seismic column demands.

4. Demonstrated the satisfactory seismic performance of BRBF-Es that can serve as an alternative to EBFs (especially EBFs with link-to-column connections).

5. Quantified seismic column demands in BRBF-Es.

6. Quantified connection demands for BRBF-E beams with different types of beam splice connections.

7. Demonstrated system-level *dynamic* modeling techniques for BRBF-C and BRBF-E structures, with concrete slabs, and validated them using existing shake table testing.

5.3. Recommendations for Future Work

The results from the dissertation work suggest BRBF-Es as a viable alternative to currently used EBFs; however, experimental verification is needed. The slab representation used in this dissertation was only validated for system-level behavior. It is recommended that full-scale experimental testing of BRBF-E systems and components (stub-to-column connections, and beam-splice connections) be conducted, to further investigate the influence of the concrete slab on frame and connection performance.

Additionally, in the BRBF-E design, design coefficients and factors, Cd, Ω, and *R* were assumed from previous BRBF-C studies. New studies should be conducted to quantify/justify these values for BRBF-Es.

REFERENCES

[1]   Roeder, C.W., and Popov, E.P. (1978). "Eccentrically braced steel frames for earthquakes." *J. Struct. Div. ASCE,* 104(ST3), 391-412.

[2]   Black, C.J., Makris, N., and Aiken, I.D. (2004). "Component testing, seismic evaluation and characterization of buckling-restrained braces." *J. Struct. Eng.,* 130(6), 880-894.

[3]   Inoue, K., Sawaizumi, S., and Higashibata, Y. (2001). "Stiffening requirements for unbonded braces encased in concrete panels." *J. Struct. Eng.,* 127(6), 712-20.

[4]   Sabelli, R., Mahin, S., and Chang, C. (2003). "Seismic demands on steel braced frame buildings with buckling-restrained braces." *Eng. Structures,* 25(2003), 655-666.

[5]   Tremblay, R., Bolduc, P., Neville, R., and DeVall, R. (2006). "Seismic testing and performance of buckling-restrained bracing systems." *Canadian J. of Struct. Eng.,* 33, 183-198.

[6]   Coy, B.B. (2007). "Buckling-restrained brace connection design and testing." *Master's Thesis,* Brigham Young University, Provo, UT.

[7]   Okazaki, T., Engelhardt, M.D., Nakashima, M., and Suita, K. (2006). "Experimental performance of link-to-column connections in eccentrically braced frames." *J. Struct. Eng.,* 132(8), 1201-1211.

[8]   Federal Emergency Management Agency, (FEMA) (2000). "Recommended seismic design criteria for new steel moment-frame buildings." *Publication FEMA-350,* FEMA, Washington, D.C.

[9]   Okazaki, T., Arce, G., Ryu, H-C., and Engelhardt, M.D. (2005). "Experimental study of local buckling, overstrength, and fracture of links in eccentrically braced frames." *J. Struct. Eng.,* 131(10), 1526-35.

[10]   Engelhardt, M.D., and Popov, E.P. (1992). "Experimental performance of long links in eccentrically braced frames." *J. Struct. Eng.,* 118(11), 3067-3088.

[11]   Ramadan, T., and Ghobarah, A. (1995). "Behaviour of bolted link-column joints in eccentrically braced frames." *Canadian J. of Struct. Eng.,* 22, 745-754.

[12]   Tsai, K.C., Chen, C.-H., Engelhardt. M.D., and Nakashima, M. (2000). "Cyclic behavior of link-to-box column connections insteel eccentrically braced frames." *Proceedings of the First International Conference on Structural Stability and Dynamics,* Taipei, Taiwan.

[13]   Okazaki, T. (2004). "Seismic performance of link-to-column connections in steel eccentrically braced frames." <u>Dept. of civil eng.</u>, Austin, Texas, Univ. of Texas at Austin, Ph.D. dissertation.

[14]   Roeder, C.W., Lehman, D.E., and Christopulos, A. (2006). "Seismic performance of special concentrically braced frames with buckling restrained braces." *Proceedings of the 8th U.S. National Conference on Earthquake Engineering,* San Francisco, California, Paper No. 1503.

[15]   Aiken, I.D., Mahin, S.A., and Uriz, P.R. (2002). "Large-scale testing of buckling restrained braced frames." *Proceedings of the Japan Passive Control Symposium,* Tokyo Institute of Technology, Japan, December 2002.

[16]   Chen, C.H., Hsiao, P.C., Lai, J.W., Lin, M.L., Weng, Y.T., and Tsai, K.C. (2004). "Pseudo-dynamic test of full-scale CFT/BRB frame: Part 2- Construction and testing." *Proceedings of the 13th World Conference on Earthquake Engineering,* Vancouver, B.C., Canada, Paper No. 2175.

[17]   Fahnestock, L.A., Ricles, J.M., and Sause, R. (2007). "Experimental evaluation of a large-scale buckling-restrained braced frame." *J. Struct. Eng.,* 133(9), 11205-1214.

[18]   Prinz, G.S., and Richards, P.W. (2008). "Seismic response of buckling-restrained braced frames with beam splices." *Proceedings of the 14th World Conference on Earthquake Engineering,* Beijing, China.

[19]   Kanvinde, A.M. and Deierlein, G.G. (2004). "Micromechanical simulation of earthquake induced fractures in steel structures." *Blume Center TR145,* Stanford Univ., Stanford, Calif.

[20]   Lin, M.L., Weng, Y.T., Tsai, K.C., Hsiao, P.C., Chen, C.H. and Lai, J.W. (2004). "Pseudo-Dynamic Test of a Full-Scale CFT/BRB Frame: Part 3 - Analysis and Performance Evaluation." *Proceedings of the 13th World Conference on Earthquake Engineering,* Vancouver, B.C., Canada, Paper No. 2173.

[21]   Silva, J.G.S., de Lima, L.R.O., da S. Vellasco, P.C.G., de Adrade, S.A.L., and de Castro, R.A. (2008). "Nonlinear dynamic analysis of steel protal frames with semi-rigid connections." *Eng. Structures,* 30, 2566-2579.

[22]   Tremblay, R., and Poncet, L. (2005). "Seismic performance of concentrically braced steel frames in multistory buildings with mass irregularity." *J. Struct. Eng.,* 131(9), 1363-1375.

[23]   Uriz, P., and Mahin, S. (2004). "Seismic performance assessment of concentrically braced steel frames." *Proceedings of the 13th World Conference on Earthquake Engineering,* Vancouver, B.C., Canada, Paper No. 1639.

[24]   Richards, P.W. and Prinz, G.S. (2007). "Nonlinear time-history analysis of refined mesh steel structures." Proc. 9th Canadian Conference on Earthquake Engineering, Ontario, Canada: Paper No. 1365.

[25]   American Institute of Steel Construction, (AISC) (2005). "Seismic provisions for structural steel buildings." Chicago.

[26]   Hjelmstad, K.D., Popov, E.P. (1983). "Cyclic behavior and design of link beams." *j. Struct. Eng.,* 109(10), 2387-2403.

[27]   Malley, J.O., Popov, E.P. (1984). "Shear links in eccentrically braced frames." *J. Struct. Eng.,* 110(9), 2275-95.

[28]   Kasai, K., Popov, E.P. (1986). "Cyclic web buckling control for shear link beams." *j. Struct. Eng.,* 112(3), 505-523.

[29]   American Institute of Steel Construction, (AISC) (2002). "Seismic provisions for structural steel buildings." *Standard ANSI/AISC,* 341-02, AISC, Chicago.

[30]   Aschheim, M., and Halterman, A. (2002). "Reduced web section beams, Phase One: Experimental findings and design implications." 7th U.S. national conference on earthquake engineering, Boston, Massachusetts.

[31]   Timoshenko, S.P. and Goodier, J.N. (1951). "Theory of elasticity 3rd edition." *Mgraw Hill Book Co., Inc.,* New York.

[32]   Richards, P.W. (2004). "Cyclic stability and capacity design of steel eccentrically braced frames." Ph.D. dissertation, Dept. of Structural Engineering, Univ. of California, San Diego, La Jolla, CA.

[33]   Richards, P.W. and Uang, C-M. (2005). "Effect of flange width thickness ratio on eccentrically braced frame link cyclic rotation capacity." *J. Struct. Eng.,* 131(10), 1546-52.

[34]   Berman, J.W., and Bruneau, M. (2007). "Experimental and analytical investigation of tubular links for eccentrically braced frames." *Eng. Structures,* 29(2007), 1929-38.

[35]   Arce, G. (2002). "Impact of higher strength steels on local buckling and overstrength of links in eccentrically braced frames." Masters Thesis, Univ. of Texas at Austin, Austin, Tex.

119

[36]   HKS (2006). "ABAQUS Standard Users Manual, Version 6.4, Hibbitt, Karlsson, and Sorensen, Inc.", Providence, RI.

[37]   Kaufmann, E.J., Metrovich, B.R., and Pense, A.W. (2001). "Characterization of cyclic inelastic strain behavior on properties of A572 Gr. 50 and A913 Gr. 50 rolled sections." ATLSS Rep. No. 01-13, Bethlehem, Pa, National Center for Engineering Research on Advanced Technology for Large Structural Systems, Lehigh Univ.

[38]   Hancock, J.W., and Mackenzie, A.C. (1976). "On the mechanics of ductile failure in high-strength steel subjected to multi-axial stress-states." *J. Mech. Phys. Solids,* 24(3), 147-160.

[39]   Fell, B.V., Myers, A.T., Deierlein, G.G., and Kanvinde, A.M. (2006). "Testing and simulation of ultra-low cycle fatigue and fracture in steel braces." Proc. 8th U.S. National Conference on Earthquake Engineering, San Francisco, CA: Paper No. 587.

[40]   Shih-Ho Chao, Kapil Khandelwal, and Sherif El-Tawil (2006). "Ductile web fracture initiation in steel shear links." *J. Struct. Eng.,* 132(8), 1192-1200.

[41]   Kanvinde, A.M. and Deierlein, G.G. (2006). "Void growth model and stress modified critical strain model to predict ductile fracture in structural steels." *J. Struct. Eng.,* 132(12), 1907-18.

[42]   Chi, W-M., Kanvinde, A.M., and Deierlein, G.G. (2006). "Prediction of ductile fracture in steel connections using SMCS criterion." *J. Struct. Eng.,* 132(2), 171-181.

[43]   Berman, J.W., Okazaki, T., and Hauksdottir, H.O. (2009). "Reduced link sections for improving the ductility of eccentrically braced frame link-to-column connections." *J. Struct. Eng.,* doi:10.1061/(ASCE)ST.1943-541X.0000157.

[44]   MSC_Software (2005). "MSC. Marc User's Guide." MSC.Software Corporation, Santa Ana, CA.

[45]   Hjelmstad, K.D., Popov, E.P. (1982). "Characteristics of eccentrically braced frames." *J. Struct. Eng.,* 110(2), 340-353.

[46]   Popov, E.P., Ricles, J.M., Kasai, K. (1992). "Methodology for optimum EBF link design." Proc. 10th World Conference on Earthquake Engineering, Balkema, Rotterdam,(Vol. 7), 3983-3988.

[47]   ASCE. (2005a). *Minimum design loads for buildings and other structures, ASCE 7-05/ANSI A58,* Reston, Va.

[48]   Merritt, S., Uang, C.-M., and Benzoni, G. (2003). "Subassemblage testing of Corebrace buckling-restrained braces." *TR-2003/01,* Dept. of Struct. Eng., Univ. of California at San Diego, La Jolla, CA.

[49] Reaveley, L., Okahashi, T., and Fatt, C. (2004). "Corebrace Series E buckling-restrained brace test results." Dept. of Civil and Environmental Engineering, Univ. of Utah, Salt Lake City.

[50] Richards, P.W. (2009). "Seismic column demands in ductile braced frames." *J. Struct. Eng.,* 135(1), 33-41.

[51] Mazzoni, S., McKenna, F., Scott, M.H., and Fenves, G.L. (2006). "The Open System for Earthquake Engineering Simulation (OpenSEES) User Command-Language Manual." *Pacific Earthquake Eng. Research Center,* Univ. Calif., Berkeley, CA, (http://opensees.berkeley.edu).

[52] Menegotto, M. and Pinto, P.E. (1973). "Method of analysis of cyclically loaded RC plane frames including changes in geometry and non-elastic behavior of elements under normal force and bending, Preliminary Report." *IABSE, Vol. 13, pp. 15-22.*

[53] Ozborrow, G.T. (2009). "Optimized distribution of strength in buckling-restrained brace frames in tall buildings." *Masters Thesis,* BYU, Provo, UT.

[54] Ramadan, T., and Ghobarah, A. (1995). "Analytical model for shear-link behavior." *J. Struct. Eng.,* ASCE, 121(11), 1574-1580.

[55] Chi, W-M., El-Tawil S., and Deierlein, G.G. (1998). "Inelastic analysis of a 17-story steel framed building damaged during Northridge." *Eng. Structures,* 20(4-6), 481-495.

[56] Tremblay, R., and Robert, N. (2001). "Seismic performance of low- and medium-rise chevron braced steel frames." *Canadian J. of Civ. Eng.,* 28(4), 699-714.

[57] Foutch, D.A., and Yun, S.-Y. (2001). "Modeling of steel moment frames for seismic loads." *J. of Const. Steel Res.,* 58(2002), 529-564.

[58] (FEMA), Federal Emergency Management Agency (2003). "NEHRP recommended prvisions for seismic regulations for new buildings and other structures. 1: Provisions and 2: Commentary." *FEMA 450,* Washington, D.C.

[59] McCormick, J., Aburan, H., Ikenaga, M., and Nakashima, M. (2008). "Permissible residual deformation levels for building structures considering both safety and human elements." *Proc. 14th World Conf. Earthquake Eng.,* Beijing, China, Paper No. 05-06-0071.

[60] Gupta, A., and Krawinkler, H. (1999). "Prediction of seismic demands for SMRFs with ductile connections and elements." *Report No. SAC/BD-99/06,* SAC Joint Venture, Sacrameto, CA.

[61] E-Defense (2009). Blind Analysis Contest Application Site, Website: http://www.blind-analysis.jp/index_e.html.

[62] Zhou, F., Moslam, K.M., and Masayoshi, Nakashima (2007). "Finite-element analysis of a composite frame under large lateral cyclic loading." *J. Struct. Eng.,* 133(7), 1018-1026.

[63] Zhang, X., Ricles, J.M., Lu, L.-W., and Fisher, J.W. (2004). "Analytical and experimental studies on seismic behavior of deep column-to-beam welded reduced beam section moment connections." *13th World Conference on Earthquake Eng.,* Vancouver, B.C., Canada, Paper No. 1599.

[64] Jones, S.L., Fry, G.T., and Engelhardt, M.D. (2002). "Experimental evaluation of cyclically loaded reduced beam section mement connections." *J. Struct. Eng.,* 128(4), 441-51.

Appendix A: OPENSEES SOURCE CODE

The following pages contain the source code for building the 3-story BRBF-E and EBF

frames in OpenSEES. The scripts may be cut and pasted directly into a text editor (i.e.;

WordPad) and then saved as a .tcl file for future use.

A.1 3-Story BRBF-E OpenSEES Source Code

```
# 3-Story BRBF-E Test Frame
# Gary S. Prinz 2009
#
# nonlinear elements, inelastic fiber sections

#       ____o_____o_____
#       |        _ * _   |
#       |     _ *    | | |
#       |_*         |_| |
#       |---o-----o----|
#       |        _ * _   |
#       |     _ *    | | |
#       |_*         |_| |
#       |---o-----o----|
#       |        _ * _   |
#       |     _ *    | | |
#       |_*         |_| |


# SET UP ----------------------------------------------------------------
--------
wipe;                    # clear memory of all past model definitions
model BasicBuilder -ndm 2 -ndf 3;   # Define the model builder,
ndm=#dimension, ndf=#dofs
set dataDir EBRBF_Data;              # set up name of data directory
file mkdir $dataDir;                 # create data directory
set GMdir "../GMfiles/";             # ground-motion file directory
source LibUnits.tcl;                 # define units
source DisplayPlane.tcl;
source DisplayModel2D.tcl;    # procedure for displaying 2D perspective
source Wsection.tcl;          # procedure to define fiber W section
source rotSpring2D.tcl;       # Rotational spring definition for beam splices

# Analysis Type
      set Type "Static"
```

```
            set EQ ""
            set EQfact 2.2
            set Importance "I=1"


#LOMA-PRIETA_GILROY-3    1.4
#LOMA-PRIETA_GILROY-4    1.4
#LOMA-PRIETA_HCH         1.2
#LOMA-PRIETA_HDA         0.93
#LOMA-PRIETA_S-CA        2.35
#Northridge_CanogaPark   0.88
#Northridge_BeverlyHills  1.3
#Northridge_Castaic      0.61
#Northridge_N-Westmoreland   2.2
#Northridge_Pacoima      0.6




# define GEOMETRY ---------------------------------------------------------
--
# define NODAL COORDINATES
            node 1 0.0 0.0              # define nodes for EBRBF test frame
            node 2 0.0 156.0
            node 3 0.0 312.0
            node 4 0.0 468.0
            node 5 36.0 468.0
            node 22 36.0 468.0
            node 6 36.0 312.0
            node 20 36.0 312.0
            node 7 36.0 156.0
            node 18 36.0 156.0
            node 8 288.0 156.0
            node 19 288.0 156.0
            node 9 288.0 312.0
            node 21 288.0 312.0
            node 10 288.0 468.0
            node 23 288.0 468.0
            node 11 312.0 156.0
            node 12 312.0 312.0
            node 13 312.0 468.0
            node 14 360.0 0.0
            node 15 360.0 156.0
            node 16 360.0 312.0
            node 17 360.0 468.0

# Representative Gravity Column
            node 24 370 0
            node 25 370 156
            node 26 370 312
            node 27 370 468




# Set up parameters that are particular to the model for displacement control

set IDctrlNode 4;        # node where displacement is read for displacement
control
set IDctrlDOF 1;         # degree of freedom of displacement read for
displacement control
```

124

```
set NStory 3;              # number of stories above ground level
set NBay 1;        # number of bays
set LBuilding 468;              # total building height

# BOUNDARY CONDITIONS
fix 1 1 1 1;               # Fixed support nodes
fix 14 1 1 1;              # Fixed support nodes
fix 24 1 1 0;              # Fixed support nodes

# calculated MODEL PARAMETERS, particular to this model

# define MATERIAL properties -------------------------------------------------
------------------------------------

# Material properties, column and beam sections all defined in Input.tcl

                # $R0, $cR1, $cR2 control the transition from elastic to
plastic branches.
                # Recommended values:
                # $R0=between 10 and 20, $cR1=0.925, $cR2=0.15
                set R0_BC 20
                set cR1_BC 0.925
                set cR2_BC 0.15

        # Beam and Column Materials
                set b_BC 0.01
                set Fy 50
                set Es 29000
                set BCMat 10
                uniaxialMaterial Steel02 $BCMat $Fy $Es $b_BC $R0_BC
$cR1_BC $cR2_BC

        # Brace Materials

                set Fybrace 46
                set BraceMat1 20000
                set BraceMat2 30000
                set b_Brace 0.025

        # Parameters used in the Giuffré-Menegotto-Pinto equations
    set R0_Brace 1.95;       # exponent that controls the transition between
elastic and hardening branch
    set cR1_Brace 0.001;    # parameter for the change of R with cyclic
loading history
    set cR2_Brace 0.001;    # parameter for the change of R with cyclic
loading history

uniaxialMaterial Steel02 $BraceMat1 [expr $Fybrace*1.65] 62514 $b_Brace
$R0_Brace $cR1_Brace $cR2_Brace
uniaxialMaterial Steel02 $BraceMat2 [expr $Fybrace*1.65] 58398 $b_Brace
$R0_Brace $cR1_Brace $cR2_Brace
# ELEMENT properties ---------------------------------------------------------
------------------------------------
# Structural-Steel W-section properties

# column sections: W21x147
set ColSecTag 1
```

```
set d [expr 22.1*$in];  # depth
set bf [expr 12.5*$in]; # flange width
set tf [expr 1.15*$in]; # flange thickness
set tw [expr 0.72*$in]; # web thickness
set nfdw 16;            # number of fibers along dw
set nftw 2;        # number of fibers along tw
set nfbf 16;            # number of fibers along bf
set nftf 4;             # number of fibers along tf
Wsection  1 $BCMat $d $bf $tf $tw $nfdw $nftw $nfbf $nftf

# beam sections: W27x102
#set BeamSecTag 2
set d [expr 27.1*$in];  # depth
set bf [expr 10*$in];   # flange width
set tf [expr 0.830*$in];     # flange thickness
set tw [expr 0.515*$in];     # web thickness
set nfdw 16;            # number of fibers along dw
set nftw 2;        # number of fibers along tw
set nfbf 16;            # number of fibers along bf
set nftf 4;             # number of fibers along tf
Wsection  2 $BCMat $d $bf $tf $tw $nfdw $nftw $nfbf $nftf

# beam sections: W24x94
#set BeamSecTag 3
set d [expr 24.3*$in];  # depth
set bf [expr 9.07*$in]; # flange width
set tf [expr 0.875*$in];     # flange thickness
set tw [expr 0.515*$in];     # web thickness
set nfdw 16;            # number of fibers along dw
set nftw 2;        # number of fibers along tw
set nfbf 16;            # number of fibers along bf
set nftf 4;             # number of fibers along tf
Wsection  3 $BCMat $d $bf $tf $tw $nfdw $nftw $nfbf $nftf

# beam sections: W21x68
#set BeamSecTag 3
set d [expr 21.1*$in];  # depth
set bf [expr 8.27*$in]; # flange width
set tf [expr 0.685*$in];     # flange thickness
set tw [expr 0.430*$in];     # web thickness
set nfdw 16;            # number of fibers along dw
set nftw 2;        # number of fibers along tw
set nfbf 16;            # number of fibers along bf
set nftf 4;             # number of fibers along tf
Wsection  4 $BCMat $d $bf $tf $tw $nfdw $nftw $nfbf $nftf


# define ELEMENTS -------------------------------------------------------------
----------------------------------------
## element nonlinearBeamColumn $elemID $nodeI $nodeJ $np $ColSecTag
$IDColTransf;
# set up geometric transformations of element
#   separate columns and beams, in case of P-Delta analysis for columns
     set IDColTransf 101; # all columns
     set IDBeamTransf 102; # all beams
     set IDBraceTransf 103; # all braces
```

```
      set ColTransfType Corotational;                      # options, Linear
PDelta Corotational
      geomTransf $ColTransfType $IDColTransf  ;       # only columns can have
PDelta effects (gravity effects)
      geomTransf Corotational $IDBeamTransf
      geomTransf Corotational $IDBraceTransf

      set np 5;   # number of Gauss integration points for nonlinear
curvature distribution

# COLUMNS
      element nonlinearBeamColumn 1 1 2 $np 1 $IDColTransf;
      element nonlinearBeamColumn 2 2 3 $np 1 $IDColTransf;
      element nonlinearBeamColumn 3 3 4 $np 1 $IDColTransf;
      element nonlinearBeamColumn 5 14 15 $np 1 $IDColTransf;
      element nonlinearBeamColumn 6 15 16 $np 1 $IDColTransf;
      element nonlinearBeamColumn 7 16 17 $np 1 $IDColTransf;


# Gravity Column
      element elasticBeamColumn 50 24 25 15.6 29000 507 $IDColTransf
      element elasticBeamColumn 51 25 26 15.6 29000 507 $IDColTransf
      element elasticBeamColumn 52 26 27 15.6 29000 507 $IDColTransf


# BEAMS
      element nonlinearBeamColumn 8 2 7 $np 3 $IDBeamTransf;
      element nonlinearBeamColumn 9 18 8 $np 3 $IDBeamTransf;
      element nonlinearBeamColumn 10 19 11 $np 3 $IDBeamTransf;
      element nonlinearBeamColumn 20 11 15 $np 3 $IDBeamTransf;
      element nonlinearBeamColumn 11 3 6 $np 3 $IDBeamTransf;
      element nonlinearBeamColumn 12 20 9 $np 3 $IDBeamTransf;
      element nonlinearBeamColumn 13 21 12 $np 3 $IDBeamTransf;
      element nonlinearBeamColumn 21 12 16 $np 3 $IDBeamTransf;
      element nonlinearBeamColumn 14 4 5 $np 3 $IDBeamTransf;
      element nonlinearBeamColumn 15 22 10 $np 3 $IDBeamTransf;
      element nonlinearBeamColumn 16 23 13 $np 3 $IDBeamTransf;
      element nonlinearBeamColumn 22 13 17 $np 3 $IDBeamTransf;


# BRACES
      element corotTruss 17 1 11 [expr 6.77*pow($in,2)] $BraceMat1;
      element corotTruss 18 2 12 [expr 5.895*pow($in,2)] $BraceMat1;
      element corotTruss 19 3 13 [expr 4.518*pow($in,2)] $BraceMat1;


# Splice Model
      # Splice with Rotational Stiffness
            #rotSpring2D 25 7 18 $SpringMat
            #rotSpring2D 26 19 8 $SpringMat
            #rotSpring2D 27 6 20 $SpringMat
            #rotSpring2D 28 21 9 $SpringMat
            #rotSpring2D 29 5 22 $SpringMat
            #rotSpring2D 30 23 10 $SpringMat



# Perfectly Pinned Splice
            equalDOF 7 18 1 2
            equalDOF 8 19 1 2
            equalDOF 6 20 1 2
            equalDOF 9 21 1 2
```

```
            equalDOF 5 22 1 2
            equalDOF 10 23 1 2


# Assign masses to nodes
      mass 2 1.02375 1e-9 1e-9
      mass 15 1.02375 1e-9 1e-9
      mass 3 1.02375 1e-9 1e-9
      mass 16 1.02375 1e-9 1e-9
      mass 4 1.1078 1e-9 1e-9
      mass 17 1.1078 1e-9 1e-9


# Attachment of Gravity Column to Frame
      equalDOF 15 25 1 3
      equalDOF 16 26 1 3
      equalDOF 17 27 1 3



# define GRAVITY In Representative Column
pattern Plain 1 Linear {
        load 25 0. -767.5 0.;
        load 26 0. -767.5 0.;
        load 27 0. -820. 0.;
      }

      constraints Plain;       # how it handles boundary conditions
      numberer Plain;          # renumber dof's to minimize band-width
      system BandGeneral;      # how to store and solve the system of
                                 equations in the analysis

      test NormDispIncr 1.0e-8 6 ;  # determine if convergence has been
                                    achieved at the end of an iteration step
      algorithm Newton;             # use Newton's solution algorithm:
                                    updates tangent stiffness at every
                                    iteration
      integrator LoadControl 0.1;   # determine the next time step for an
                                    analysis, # apply gravity in 10 steps
      analysis Static               # define type of analysis static or
                                    transient
      analyze 10;                   # perform gravity analysis
      loadConst -time 0.0;          # hold gravity constant and restart time



# Node and Element Recorders
   # Nodal Displacements and Accelerations
      recorder Node -file
$dataDir/$Importance/3EBRBF/$Type/$EQ/NodeDisp_EBRBF_$EQ.out -time -node 1 2
3 4 5 6 7 8 9 10 11 12 13 14 15 16 17 -dof 1 2 disp;        # Nodal
displacements
      recorder Node -file
$dataDir/$Importance/3EBRBF/$Type/$EQ/NodeDispStaticPush_EBRBF_$EQ.out -time
-node 4 -dof 1 disp;             # Nodal displacements
      recorder Node -file
$dataDir/$Importance/3EBRBF/$Type/$EQ/NodeAccel_EBRBF_$EQ.out -time -node 2
15 3 16 4 17 -dof 1 2 3 accel;          # Nodal Accel

   # Story Drifts
```

```
      recorder Drift -file
$dataDir/$Importance/3EBRBF/$Type/$EQ/Drift1_EBRBF_$EQ.out -time -iNode 1 -
jNode 2 -dof 1 -perpDirn 2;        # drift story 1
      recorder Drift -file
$dataDir/$Importance/3EBRBF/$Type/$EQ/Drift2_EBRBF_$EQ.out -time -iNode 2 -
jNode 3 -dof 1 -perpDirn 2;        # drift story 2
      recorder Drift -file
$dataDir/$Importance/3EBRBF/$Type/$EQ/Drift3_EBRBF_$EQ.out -time -iNode 3 -
jNode 4 -dof 1 -perpDirn 2;        # drift story 3

   # Brace Hysteresis
      recorder Element -file
$dataDir/$Importance/3EBRBF/$Type/$EQ/Brace1Axial_EBRBF_$EQ.out -time -ele 17
axialForce;            # Brace 1 Axial Force
      recorder Element -file
$dataDir/$Importance/3EBRBF/$Type/$EQ/Brace1Deform_EBRBF_$EQ.out -time -ele
17 deformations;             # Brace 1 Axial Force

      recorder Element -file
$dataDir/$Importance/3EBRBF/$Type/$EQ/Brace2Axial_EBRBF_$EQ.out -time -ele 18
axialForce;            # Brace 1 Axial Force
      recorder Element -file
$dataDir/$Importance/3EBRBF/$Type/$EQ/Brace2Deform_EBRBF_$EQ.out -time -ele
18 deformations;             # Brace 1 Axial Force

      recorder Element -file
$dataDir/$Importance/3EBRBF/$Type/$EQ/Brace3Axial_EBRBF_$EQ.out -time -ele 19
axialForce;            # Brace 1 Axial Force
      recorder Element -file
$dataDir/$Importance/3EBRBF/$Type/$EQ/Brace3Deform_EBRBF_$EQ.out -time -ele
19 deformations;             # Brace 1 Axial Force

   # Column Demands (first story columns)
      recorder Element -file
$dataDir/$Importance/3EBRBF/$Type/$EQ/Columnforce(Left)_EBRBF_$EQ.out -time -
ele 1 2 3 globalForce;              # Column Demands(story 1 Left)
      recorder Element -file
$dataDir/$Importance/3EBRBF/$Type/$EQ/Columnforce(Right)_EBRBF_$EQ.out -time
-ele 5 6 7 globalForce;             # Column Demands(story 1 Right)

   # Base Shear
      recorder Node -file
$dataDir/$Importance/3EBRBF/$Type/$EQ/BaseShear_$EQ.out -time -node 1 14 -dof
1 reaction;             # Nodal Reaction at Base


set Tol 1.0e-8;   # Convergence tolerance

#DisplayModel2D NodeNumbers


# ------------ PeriodFreq&Damping ------------------------------------
# determine Natural Period, Frequency & damping parameters for SDOF

set xDamp 0.05; # damping ratio (0.02-0.05-typical)
set lambda [eigen 1]
set omega [expr pow($lambda,0.5)]
```

129

```
set Tperiod [expr 2*$PI/$omega]; # period (sec.)
puts $Tperiod
set alphaM 0; # stiffness-prop. RAYLEIGH damping parameter; D = alphaM*M
set betaK 0; # stiffness proportional damping; +betaK*KCurrent
set betaKcomm [expr 2*$xDamp/$omega]; # mass-prop. RAYLEIGH damping
parameter; +betaKcomm*KlastCommitt
set betaKinit 0; # initial-stiffness proportional damping +beatKinit*Kini
```

A.2 3-Story EBF OpenSEES Source Code

```
# 3-Story EBF Comparison Frame
# Gary S. Prinz 2009
#
# nonlinear elements, inelastic fiber sections

#      _____
#      |       _ * _  |
#      |    _ *    | | |
#      |_ *        |_| |
#      |-------------|
#      |       _ * _  |
#      |    _ *    | | |
#      |_ *        |_| |
#      |-------------|
#      |       _ * _  |
#      |    _ *    | | |
#      |_ *        |_| |


# SET UP ---------------------------------------------------------------------
--------
wipe;                    # clear memory of all past model definitions
model BasicBuilder -ndm 2 -ndf 3;   # Define the model builder,
ndm=#dimension, ndf=#dofs
set dataDir EBF_Data;               # set up name of data directory (can
remove this)
file mkdir $dataDir;                # create data directory
set GMdir "../GMfiles/";                # ground-motion file directory
source LibUnits.tcl;              # define units
source DisplayPlane.tcl;          # procedure for displaying a plane in
model
source DisplayModel2D.tcl;        # procedure for displaying 2D perspective
of model
source Wsection.tcl;          # procedure to define fiber W section
source rotSpring2D.tcl;       # Rotational spring definition for beam splices

# Analysis Type
     set Type "Static"
     set EQ ""
     set EQfact 2.9
     set Importance "I=1"

#LOMA-PRIETA_GILROY-3   1.2
#LOMA-PRIETA_GILROY-4   1.25
```

```
#LOMA-PRIETA_HCH          0.68
#LOMA-PRIETA_HDA          0.7
#LOMA-PRIETA_S-CA         2
#Northridge_CanogaPark    0.7
#Northridge_BeverlyHills  1.6
#Northridge_Castaic       0.6
#Northridge_N-Westmoreland  2.9
#Northridge_Pacoima       0.67


# define GEOMETRY -------------------------------------------------------------
--
# define NODAL COORDINATES
            node 1 0.0 0.0            # define nodes for EBRBF test frame
            node 2 0.0 156.0
            node 3 0.0 312.0
            node 4 0.0 468.0
            node 5 312 156
            node 6 312 312
            node 7 312 468
            node 8 312 156
            node 9 312 312
            node 10 312 468
            node 11 360 0
            node 12 360 156
            node 13 360 312
            node 14 360 468
            node 15 360 156
            node 16 360 312
            node 17 360 468

# Representative Gravity Column
            node 18 370 0
            node 19 370 156
            node 20 370 312
            node 21 370 468

# Set up parameters that are particular to the model for displacement control
set IDctrlNode 4;        # node where displacement is read for displacement
control
set IDctrlDOF 1;         # degree of freedom of displacement read for
displacement control
set NStory 3;            # number of stories above ground level
set NBay 1;        # number of bays
set LBuilding 468;              # total building height

# BOUNDARY CONDITIONS
fix 1 1 1 1;             # Fixed support nodes
fix 11 1 1 1;           # Fixed support nodes
fix 18 1 1 0;           # Fixed support nodes

# calculated MODEL PARAMETERS, particular to this model

# define MATERIAL properties ---------------------------------------------------
-------------------------------------
```

```
            # Beam, Brace and Column Materials
                # $R0, $cR1, $cR2 control the transition from elastic to
plastic branches.
                # Recommended values:
                # $R0=between 10 and 20, $cR1=0.925, $cR2=0.15
                set R0_BC 20
                set cR1_BC 0.925
                set cR2_BC 0.15
                set b_BC 0.01
                set Fy 50
                set Es 29000
                set BCMat 10
                uniaxialMaterial Steel02 $BCMat $Fy $Es $b_BC $R0_BC
$cR1_BC $cR2_BC

            # Link Material Properties

             # Link Flexural-Hinge Material
                set b 0.05
                set E0 29000

                set LinkMat1 150
                set Fy1 4790.5

                set LinkMat2 160
                set Fy2 3954.5

                set LinkMat3 170
                set Fy3 3019.5

                uniaxialMaterial Steel01 $LinkMat1 $Fy1 $E0 $b
                uniaxialMaterial Steel01 $LinkMat2 $Fy2 $E0 $b
                uniaxialMaterial Steel01 $LinkMat3 $Fy3 $E0 $b

             # Link Tri-Spring Shear Material

                set G 11153
                set e 48

              # First Story Link
                set Ashear 4.65;         #Link Shear Area
                set Vp 140;              #Link Shear Capacity
                set SpringMat1 245

              # Backbone Curve for Linear Springs
                set s1p [expr 1.1*$Vp]
                set s2p [expr 1.3*$Vp]
                set s3p [expr 1.5*$Vp]

                set E1 [expr 2*$G*$Ashear/$e]
                set E2 [expr 0.03*$E1]
                set E3 [expr 0.015*$E1]
                set E4 [expr 0.002*$E1]

                set Em1 [expr (1-(0.03-(0.015-0.002)))*2*$G*$Ashear/$e]
                set Em2 [expr (0.03-(0.015-0.002))*2*$G*$Ashear/$e]
                set Em3 [expr (0.015-0.002)*2*$G*$Ashear/$e]
```

```
          set Em4 [expr 0.002*2*$G*$Ashear/$e]

          set e1p [expr $s1p/$E1]
          set e2p [expr (0.2*$Vp)/$E2]
          set e3p [expr (0.2*$Vp)/$E3]

       # Material Model for Linear Springs
          uniaxialMaterial ElasticPP 1 $Em1 $e1p
          uniaxialMaterial ElasticPP 2 $Em2 [expr $e2p+$e1p]
          uniaxialMaterial ElasticPP 3 $Em3 [expr $e3p+$e2p+$e1p]
          uniaxialMaterial ElasticPP 4 $Em4 3
          uniaxialMaterial Parallel $SpringMat1 1 2 3 4


       # Second Story Link
          set Ashear2 4.04
          set Vp2 [expr 121*$kip]
          set SpringMat2 246

       # Backbone Curve for Linear Springs
          set s1p2 [expr 1.1*$Vp2]
          set s2p2 [expr 1.3*$Vp2]
          set s3p2 [expr 1.5*$Vp2]

          set E12 [expr 2*$G*$Ashear2/$e]
          set E22 [expr 0.03*$E12]
          set E32 [expr 0.015*$E12]
          set E42 [expr 0.002*$E12]

          set Em12 [expr (1-(0.03-(0.015-0.002)))*2*$G*$Ashear2/$e]
          set Em22 [expr (0.03-(0.015-0.002))*2*$G*$Ashear2/$e]
          set Em32 [expr (0.015-0.002)*2*$G*$Ashear2/$e]
          set Em42 [expr 0.002*2*$G*$Ashear2/$e]

          set e1p2 [expr $s1p2/$E12]
          set e2p2 [expr (0.2*$Vp2)/$E22]
          set e3p2 [expr (0.2*$Vp2)/$E32]

       # Material Model for Linear Springs
          uniaxialMaterial ElasticPP 12 $Em12 $e1p2
          uniaxialMaterial ElasticPP 22 $Em22 [expr $e2p2+$e1p2]
          uniaxialMaterial ElasticPP 32 $Em32 [expr
$e3p2+$e2p2+$e1p2]
          uniaxialMaterial ElasticPP 42 $Em42 3
          uniaxialMaterial Parallel $SpringMat2 12 22 32 42


       # Third Story Link
          set Ashear3 3.10
          set Vp3 [expr 93*$kip]
          set SpringMat3 247

       # Backbone Curve for Linear Springs
          set s1p3 [expr 1.1*$Vp3]
          set s2p3 [expr 1.3*$Vp3]
          set s3p3 [expr 1.5*$Vp3]
```

```
                set E13 [expr 2*$G*$Ashear3/$e]
                set E23 [expr 0.03*$E13]
                set E33 [expr 0.015*$E13]
                set E43 [expr 0.002*$E13]

                set Em13 [expr (1-(0.03-(0.015-0.002)))*2*$G*$Ashear3/$e]
                set Em23 [expr (0.03-(0.015-0.002))*2*$G*$Ashear3/$e]
                set Em33 [expr (0.015-0.002)*2*$G*$Ashear3/$e]
                set Em43 [expr 0.002*2*$G*$Ashear3/$e]
                set e1p3 [expr $s1p3/$E13]
                set e2p3 [expr (0.2*$Vp3)/$E23]
                set e3p3 [expr (0.2*$Vp3)/$E33]

            # Material Model for Linear Springs
                uniaxialMaterial ElasticPP 13 $Em13 $e1p3
                uniaxialMaterial ElasticPP 23 $Em23 [expr $e2p3+$e1p3]
                uniaxialMaterial ElasticPP 33 $Em33 [expr
$e3p3+$e2p3+$e1p3]
                uniaxialMaterial ElasticPP 43 $Em43 3
                uniaxialMaterial Parallel $SpringMat3 13 23 33 43


# ELEMENT properties ---------------------------------------------------------
-----------------------------------
# Structural-Steel W-section properties

# column sections: W14x120
set ColSecTag 1
set d [expr 14.5*$in];  # depth
set bf [expr 14.7*$in]; # flange width
set tf [expr 0.94*$in]; # flange thickness
set tw [expr 0.59*$in]; # web thickness
set nfdw 16;            # number of fibers along dw
set nftw 2;        # number of fibers along tw
set nfbf 16;            # number of fibers along bf
set nftf 4;             # number of fibers along tf
Wsection  1 $BCMat $d $bf $tf $tw $nfdw $nftw $nfbf $nftf


# column sections: W14x61
set ColSecTag 2
set d [expr 13.9*$in];  # depth
set bf [expr 10*$in];   # flange width
set tf [expr 0.645*$in];     # flange thickness
set tw [expr 0.375*$in];     # web thickness
set nfdw 16;            # number of fibers along dw
set nftw 2;        # number of fibers along tw
set nfbf 16;            # number of fibers along bf
set nftf 4;             # number of fibers along tf
Wsection  2 $BCMat $d $bf $tf $tw $nfdw $nftw $nfbf $nftf


# beam sections: W14x53
#set BeamSecTag 3
set d [expr 13.9*$in];  # depth
set bf [expr 8.06*$in]; # flange width
set tf [expr 0.66*$in]; # flange thickness
set tw [expr 0.37*$in]; # web thickness
set nfdw 16;            # number of fibers along dw
```

134

```
set nftw 2;          # number of fibers along tw
set nfbf 16;              # number of fibers along bf
set nftf 4;              # number of fibers along tf
Wsection   3 $BCMat $d $bf $tf $tw $nfdw $nftw $nfbf $nftf


# beam sections: W12x50
#set BeamSecTag 4
set d [expr 12.2*$in];  # depth
set bf [expr 8.08*$in]; # flange width
set tf [expr 0.64*$in]; # flange thickness
set tw [expr 0.37*$in]; # web thickness
set nfdw 16;             # number of fibers along dw
set nftw 2;          # number of fibers along tw
set nfbf 16;             # number of fibers along bf
set nftf 4;             # number of fibers along tf
Wsection   4 $BCMat $d $bf $tf $tw $nfdw $nftw $nfbf $nftf


# beam sections: W12x79
#set BeamSecTag 5
set d [expr 12.4*$in];  # depth
set bf [expr 12.1*$in]; # flange width
set tf [expr 0.735*$in];       # flange thickness
set tw [expr 0.47*$in]; # web thickness
set nfdw 16;             # number of fibers along dw
set nftw 2;          # number of fibers along tw
set nfbf 16;             # number of fibers along bf
set nftf 4;             # number of fibers along tf
Wsection   5 $BCMat $d $bf $tf $tw $nfdw $nftw $nfbf $nftf


# beam sections: W10x45
#set BeamSecTag 6
set d [expr 10.1*$in];  # depth
set bf [expr 8.02*$in]; # flange width
set tf [expr 0.62*$in]; # flange thickness
set tw [expr 0.35*$in]; # web thickness
set nfdw 16;             # number of fibers along dw
set nftw 2;          # number of fibers along tw
set nfbf 16;             # number of fibers along bf
set nftf 4;             # number of fibers along tf
Wsection   6 $BCMat $d $bf $tf $tw $nfdw $nftw $nfbf $nftf


# Link Hinge Section
set LinkSecTag1 12
section Uniaxial $LinkSecTag1 $LinkMat1 Mz
set LinkSecTag2 13
section Uniaxial $LinkSecTag2 $LinkMat2 Mz
set LinkSecTag3 14
section Uniaxial $LinkSecTag3 $LinkMat3 Mz



# define ELEMENTS -------------------------------------------------------------
---------------------------------------
## element nonlinearBeamColumn $elemID $nodeI $nodeJ $np $ColSecTag
$IDColTransf;
# set up geometric transformations of element
#   separate columns and beams, in case of P-Delta analysis for columns
      set IDColTransf 101; # all columns
```

```
      set IDBeamTransf 102; # all beams
      set IDBraceTransf 103; # all braces
      set ColTransfType Corotational;                  # options, Linear
PDelta Corotational
      geomTransf $ColTransfType $IDColTransf  ;       # only columns can have
PDelta effects (gravity effects)
      geomTransf Corotational $IDBeamTransf
      geomTransf Corotational $IDBraceTransf

      set np 5;   # number of Gauss integration points for nonlinear
curvature distribution

# COLUMNS
      element nonlinearBeamColumn 1 1 2 $np 1 $IDColTransf;
      element nonlinearBeamColumn 2 2 3 $np 1 $IDColTransf;
      element nonlinearBeamColumn 3 3 4 $np 1 $IDColTransf;
      element nonlinearBeamColumn 5 11 12 $np 2 $IDColTransf;
      element nonlinearBeamColumn 6 12 13 $np 2 $IDColTransf;
      element nonlinearBeamColumn 7 13 14 $np 2 $IDColTransf;

# Gravity Column
      element elasticBeamColumn 50 18 19 15.6 29000 507 $IDColTransf
      element elasticBeamColumn 51 19 20 15.6 29000 507 $IDColTransf
      element elasticBeamColumn 52 20 21 15.6 29000 507 $IDColTransf

# BEAMS
      element nonlinearBeamColumn 8 2 5 $np 3 $IDBeamTransf;
      element beamWithHinges 10 8 15 $LinkSecTag1 0 $LinkSecTag1 0 29000 15.6
541 $IDBeamTransf; #Link 1
      element zeroLength 21 5 8 -mat $SpringMat1 -dir 2
      element zeroLength 41 12 15 -mat $SpringMat1 -dir 2

      element nonlinearBeamColumn 11 3 6 $np 4 $IDBeamTransf;
      element beamWithHinges 13 9 16 $LinkSecTag2 0 $LinkSecTag2 0 29000 14.6
391 $IDBeamTransf; #Link 2
      element zeroLength 22 6 9 -mat $SpringMat2 -dir 2
      element zeroLength 42 13 16 -mat $SpringMat2 -dir 2

      element nonlinearBeamColumn 14 4 7 $np 6 $IDBeamTransf;
      element beamWithHinges 16 10 17 $LinkSecTag3 0 $LinkSecTag3 0 29000
13.3 248 $IDBeamTransf; #Link 3
      element zeroLength 23 7 10 -mat $SpringMat3 -dir 2
      element zeroLength 43 14 17 -mat $SpringMat3 -dir 2

# BRACES
      element nonlinearBeamColumn 18 1 5 $np 5 $IDBeamTransf;
      element nonlinearBeamColumn 19 2 6 $np 5 $IDBeamTransf;
      element nonlinearBeamColumn 20 3 7 $np 5 $IDBeamTransf;

# Link-End compatability with surrounding beams/columns
      equalDOF 5 8 1 3
      equalDOF 6 9 1 3
      equalDOF 7 10 1 3
      equalDOF 12 15 1 3
      equalDOF 13 16 1 3
      equalDOF 14 17 1 3
```

```
# Assign masses to nodes
      mass 2 1.02375 1e-9 1e-9
      mass 12 1.02375 1e-9 1e-9
      mass 3 1.02375 1e-9 1e-9
      mass 13 1.02375 1e-9 1e-9
      mass 4 1.1078 1e-9 1e-9
      mass 14 1.1078 1e-9 1e-9

# Attachment of Gravity Column to Frame
      equalDOF 15 19 1 3
      equalDOF 16 20 1 3
      equalDOF 17 21 1 3

# Rigid Diaphragm; Forces the horizontal displacement of column nodes to be
equal
      #equalDOF 2 12 1
      #equalDOF 3 13 1
      #equalDOF 4 14 1

# define GRAVITY In Representative Column
      pattern Plain 1 Linear {
        load 19 0. -767.5 0.;              # node#, FX FY MZ --
superstructure-weight
        load 20 0. -767.5 0.;              # node#, FX FY MZ --
superstructure-weight
        load 21 0. -820. 0.;              # node#, FX FY MZ --
superstructure-weight
      }

      constraints Plain;                       # how it handles boundary
conditions
      numberer Plain;                          # renumber dof's to minimize
band-width (optimization), if you want to
      system BandGeneral;                      # how to store and solve the
system of equations in the analysis
      test NormDispIncr 1.0e-8 6 ;             # determine if
convergence has been achieved at the end of an iteration step
      algorithm Newton;                        # use Newton's solution
algorithm: updates tangent stiffness at every iteration
      integrator LoadControl 0.1;              # determine the next
time step for an analysis, # apply gravity in 10 steps
      analysis Static                          # define type of analysis
static or transient
      analyze 10;                              # perform gravity analysis
      loadConst -time 0.0;                     # hold gravity constant and
restart time

# Node and Element Recorders
   # Story acceleration
      recorder Node -file
$dataDir/$Importance/6EBF/$Type/$EQ/Accelerations_$EQ.out -time -node 2 3 4 -
dof 2 accel;

   # Story Drifts
      recorder Drift -file $dataDir/$Importance/3EBF/$Type/$EQ/Drift1_$EQ.out
-time -iNode 1 -jNode 2 -dof 1 -perpDirn 2;          # drift story 1
```

137

```
        recorder Drift -file $dataDir/$Importance/3EBF/$Type/$EQ/Drift2_$EQ.out
-time -iNode 2 -jNode 3 -dof 1 -perpDirn 2;           # drift story 2
        recorder Drift -file $dataDir/$Importance/3EBF/$Type/$EQ/Drift3_$EQ.out
-time -iNode 3 -jNode 4 -dof 1 -perpDirn 2;           # drift story 3

        recorder Node -file
$dataDir/$Importance/3EBF/$Type/$EQ/NodeDispStaticPush_$EQ.out -time -node 4
-dof 1 disp;                    # Nodal displacements

   # Link Hysteresis Recorders
        recorder Node -file
$dataDir/$Importance/3EBF/$Type/$EQ/Link1disp_$EQ.out -time -node 5 12 2 -dof
2 disp;                 # Link 1 displacement
        recorder Element -file
$dataDir/$Importance/3EBF/$Type/$EQ/Link1force_$EQ.out -time -ele 10
localForce;             # Elem force (Link 1)
        #recorder Element -file
$dataDir/$Importance/3EBF/$Type/$EQ/Spring1force_$EQ.out -time -ele 21 force;
                # Combined Spring force (Link 1)
        #recorder Element -file
$dataDir/$Importance/3EBF/$Type/$EQ/Spring1disp_$EQ.out -time -ele 21
deformation;                    # Combined Spring force (Link 1)

        recorder Node -file
$dataDir/$Importance/3EBF/$Type/$EQ/Link2disp_$EQ.out -time -node 6 13 3 -dof
2 disp;                 # Link 2 displacement
        recorder Element -file
$dataDir/$Importance/3EBF/$Type/$EQ/Link2force_$EQ.out -time -ele 13
localForce;             # Elem force (Link 2)
        #recorder Element -file
$dataDir/$Importance/3EBF/$Type/$EQ/Spring2force_$EQ.out -time -ele 22 force;
                # Combined Spring force (Link 2)
        #recorder Element -file
$dataDir/$Importance/3EBF/$Type/$EQ/Spring2disp_$EQ.out -time -ele 22
deformation;                    # Combined Spring force (Link 2)

        recorder Node -file
$dataDir/$Importance/3EBF/$Type/$EQ/Link3disp_$EQ.out -time -node 7 14 4 -dof
2 disp;                 # Link 3 displacement
        recorder Element -file
$dataDir/$Importance/3EBF/$Type/$EQ/Link3force_$EQ.out -time -ele 16
localForce;             # Elem force (Link 3)
        #recorder Element -file
$dataDir/$Importance/3EBF/$Type/$EQ/Spring3force_$EQ.out -time -ele 23 force;
                # Combined Spring force (Link 3)
        #recorder Element -file
$dataDir/$Importance/3EBF/$Type/$EQ/Spring3disp_$EQ.out -time -ele 23
deformation;                    # Combined Spring force (Link 3)

   # Column Demands (first story columns)
        recorder Element -file
$dataDir/$Importance/3EBF/$Type/$EQ/Columnforce(Left)_$EQ.out -time -ele 1 2
3 globalForce;                  # Column Demands(story n Left)
        recorder Element -file
$dataDir/$Importance/3EBF/$Type/$EQ/Columnforce(Right)_$EQ.out -time -ele 5 6
7 globalForce;                  # Column Demands(story n Right)
```

```
    recorder Element -file
$dataDir/$Importance/3EBF/$Type/$EQ/Brace1LocForce_$EQ.out -time -ele 18
localForce;                # Brace 1 Axial Force

   # BASE SHEAR
      recorder Node -file
$dataDir/$Importance/3EBF/$Type/$EQ/BaseShear_$EQ.out -time -node 1 20 -dof 1
reaction;                  # Nodal reactions at base of columns


set Tol 1.0e-8;   # Convergence tolerance

#DisplayModel2D NodeNumbers
#DisplayModel2D DeformedShape


# ------------ PeriodFreq&Damping ------------------------------------
# determine Natural Period, Frequency & damping parameters for SDOF

set xDamp 0.05; # damping ratio (0.02-0.05-typical)
set lambda [eigen 1]
set omega [expr pow($lambda,0.5)]
set Tperiod [expr 2*$PI/$omega]; # period (sec.)
puts "Building Period"
puts $Tperiod
set alphaM 0; # stiffness-prop. RAYLEIGH damping parameter; D = alphaM*M
set betaK 0; # stiffness proportional damping; +betaK*KCurrent
set betaKcomm [expr 2*$xDamp/$omega]; # mass-prop. RAYLEIGH damping
parameter; +betaKcomm*KlastCommitt
     set   betaKinit   0;   #   initial-stiffness   proportional   damping

+beatKinit*Kini
```

Appendix B: DESCRIPTION AND VALIDATION OF OPENSEES EBF LINK MODEL

B.1 Overview of Link Model

The EBF shear links analyzed in Chapter 3 were modeled using the techniques proposed by Ramadan and Ghobarah [54] and modified slightly by Richards 2004 [32]. Fig. B-1 shows the link element used, consisting of an elastic beam element with lumped plasticity, and translational springs in series at each end. In OpenSEES, beamWithHinges elements modeled the elastic beam element with lumped plasticity, and zero-length elements modeled the translational springs (see Fig. B-1). To achieve the combined translational spring behavior described in [32], individual springs were modeled using an elastic-perfectly-plastic material model, and then combined into a single uniaxial parallel material model. The parallel material model was then applied to the zero-length element. Fig. B-2 shows the constitutive behavior for the parallel material model.
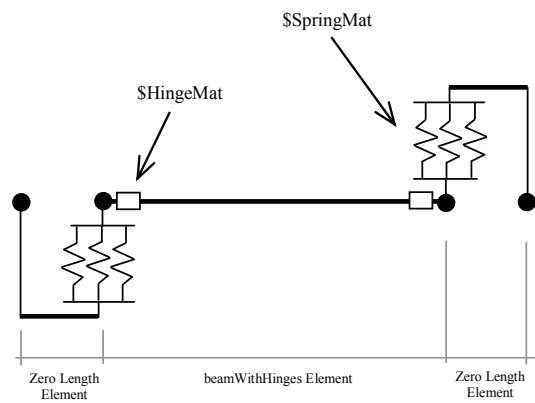
Fig. B-1 EBF link element [54]
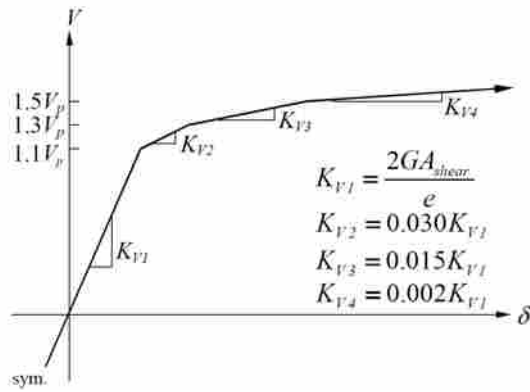
Fig. B-2 Combined behavior of parallel translational springs [32]

B.1.1. Link Model Validation Study

To validate the link model described above, the experimental setup and loading used by Okazaki et al. [7] was recreated in OpenSEES. Fig. B-3 shows the experimental setup used by [7] and Fig. B-4 shows the corresponding OpenSEES model. The loading for both the experiment and model consisted of reversed cyclic static loading with displacement amplitudes varying according to the protocol outlined in the 2002 AISC Seismic Provisions [29].

Hysteretic plots of link force versus displacement for both the experiment and OpenSEES model are shown in Fig. B-5. From Fig. B-5, similar link behavior can be seen between the experiment and OpenSEES model. Both the model and experiment sustained loads near 1068kN (240 kips) at 0.06 rad, and showed similar inelastic strength gain. The similar system-level link behavior in Fig. B-5, provides reasonable confidence in the OpenSEES link model.
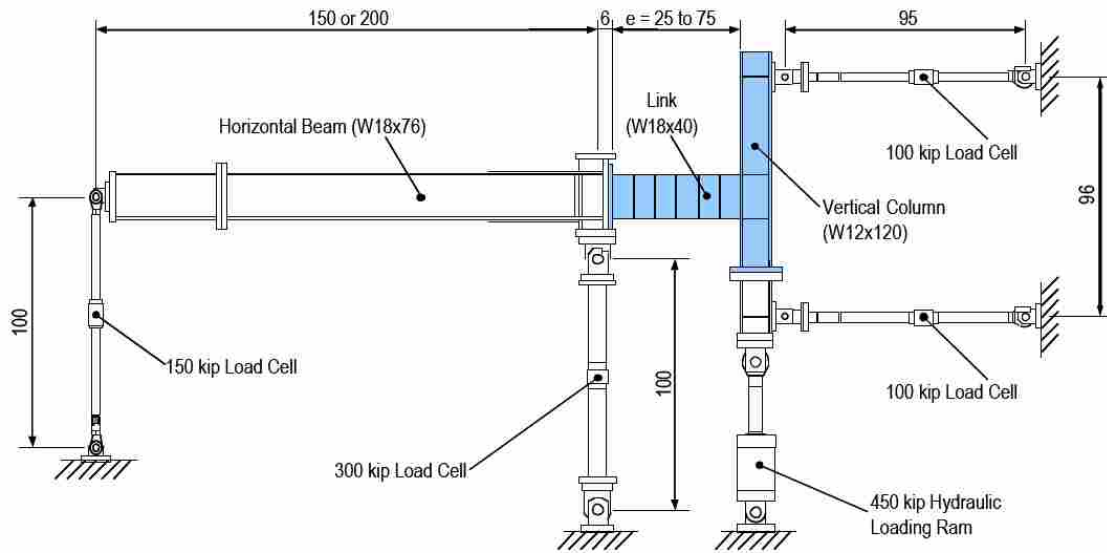
Fig. B-3 Experimental setup used by Okazaki et al [7]
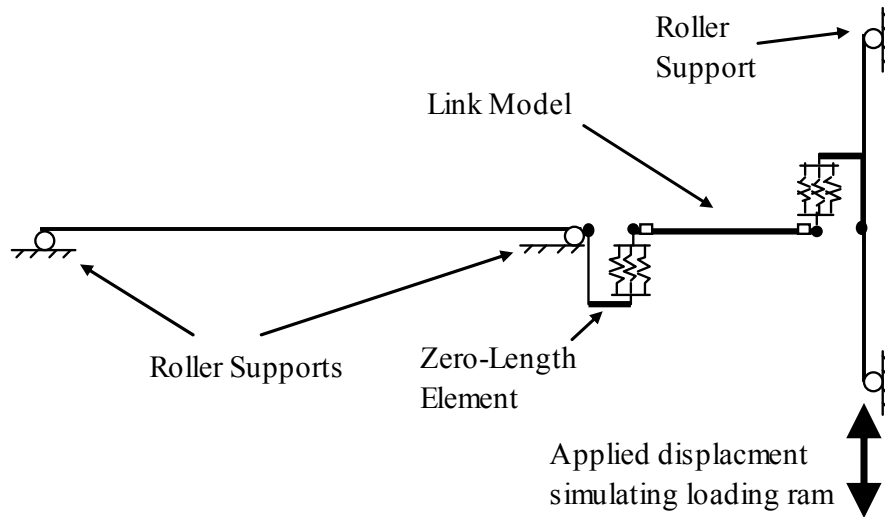
Fig. B-4 OpenSEES model simulating experimental setup

(a)

(b)
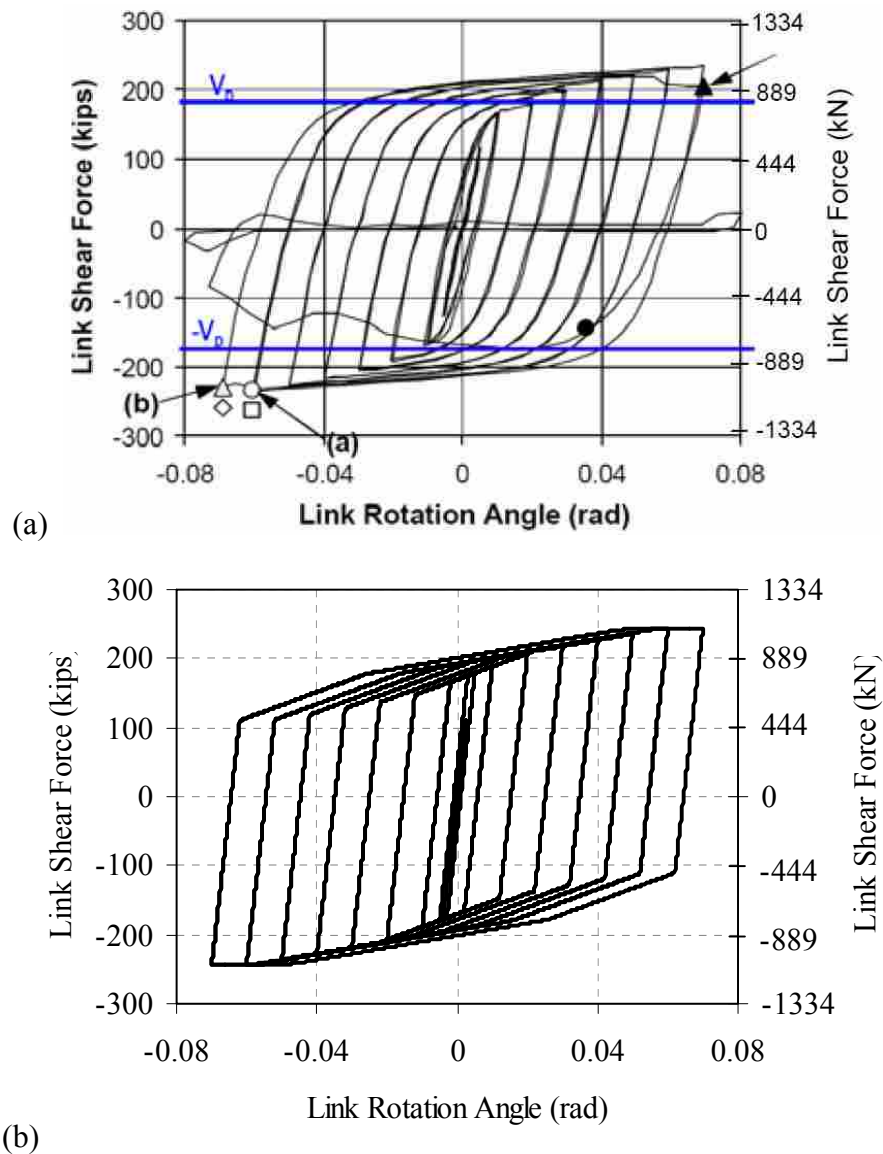
Fig. B-5 Hysteretic link behavior for: (a) experimental test [7]; and, (b) OpenSEES link model

B.1.2. Explanation of Source Code for EBF Flexural-Hinge and Tri-Spring Link Material Model

The following represents the OpenSEES code used to generate the Flexural-Hinge and Tri-Spring uniaxial material models for modeling EBF link behavior. Comments and descriptions have been added to help explain the various code parameters. The following source code can be copied and pasted into an existing OpenSEES .tcl analysis file for future use.

144

```
# MATERIAL DEFINITIONS

    # Link Flexural-Hinge Material ($HingeMat)

        set b 0.05;             #Ratio of Kyield to Kelastic
        set E0 29000;           #Kelastic
        set HingeMat 100;       #HingeMat Identifier
        set Fy $Mp;             #Sets Hinges to yield at Mp

        uniaxialMaterial Steel01 $HingeMat $Fy $E0 $b

    # Link Tri-Spring Shear Material ($SpringMat)

        set G 11153;            #Shear modulus
        set e 48;               #Link length

        set Ashear 4.65;        #Link Shear Area
        set Vp 140;             #Link Shear Capacity
        set SpringMat 245;      #SpringMat Identifier

# Backbone Curve for Linear Springs
        set s1p [expr 1.1*$Vp]
        set s2p [expr 1.3*$Vp]
        set s3p [expr 1.5*$Vp]

        set E1 [expr 2*$G*$Ashear/$e]
        set E2 [expr 0.03*$E1]
        set E3 [expr 0.015*$E1]
        set E4 [expr 0.002*$E1]

        set e1p [expr $s1p/$E1]
        set e2p [expr (0.2*$Vp)/$E2]
        set e3p [expr (0.2*$Vp)/$E3]

set Em1 [expr (1-(0.03-(0.015-0.002)))*2*$G*$Ashear/$e]
set Em2 [expr (0.03-(0.015-0.002))*2*$G*$Ashear/$e]
set Em3 [expr (0.015-0.002)*2*$G*$Ashear/$e]
set Em4 [expr 0.002*2*$G*$Ashear/$e]

# Material Model for Individual Elasto-Plastic Springs
        uniaxialMaterial ElasticPP 1 $Em1 $e1p
        uniaxialMaterial ElasticPP 2 $Em2 [expr $e2p+$e1p]
        uniaxialMaterial ElasticPP 3 $Em3 [expr $e3p+$e2p+$e1p]
        uniaxialMaterial ElasticPP 4 $Em4 3

# Material Model for Combined Elasto-Plastic Springs
        uniaxialMaterial Parallel $SpringMat 1 2 3 4
```

Force-deformation relationship for combined spring action

Individual spring moduli

Appendix C: INDIVIDUAL EBF AND BRBF-E INTER-STORY DRIFT RESULTS FROM CHAPTER 3 COMPARISON STUDY

Individual story drift results from the comparison study performed in Chapter 3 are provided in Fig. C-1 through Fig. C-4. The figures represent the maximum story response of each frame under each of the ten earthquake ground motions described in Chapter 3. Fig. C-1 shows the individual inter-story drift values for the 30 ft bay width EBF and BRBF-E frames having strength level I=1.0. Fig. C-2 shows the individual inter-story drift values for the 30 ft bay width EBF and BRBF-E frames having strength level I=1.5. Fig. C-3 shows the individual inter-story drift values for the 20 ft bay width EBF and BRBF-E frames having strength level I=1.0. Fig. C-4 shows the individual inter-story drift values for the 20 ft bay width EBF and BRBF-E frames having strength level I=15.
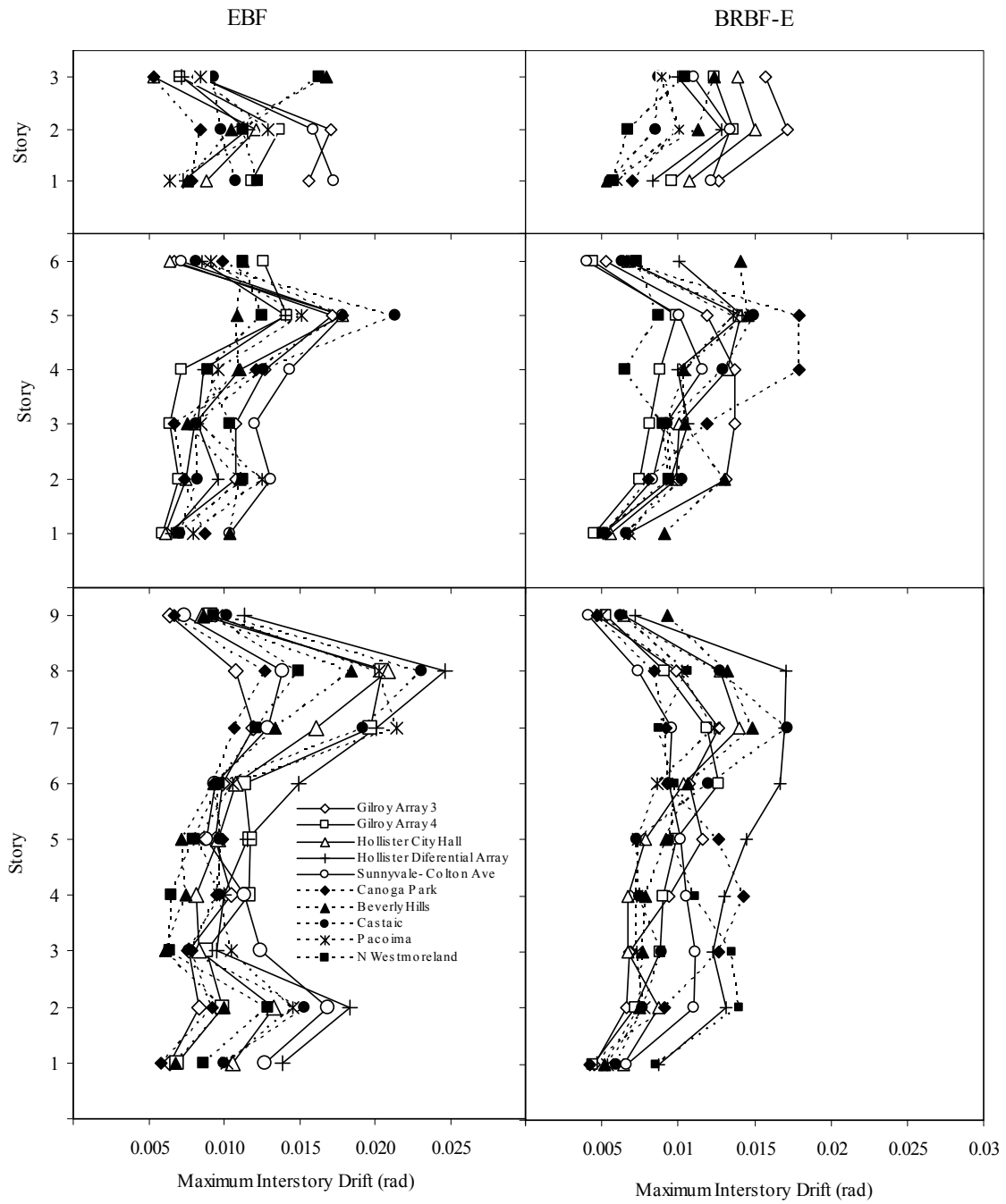
Fig. C-1 Individual story drift responses for EBF and BRBF-Es with 30 ft bay width and strength level I=1.0

EBF   BRBF-E
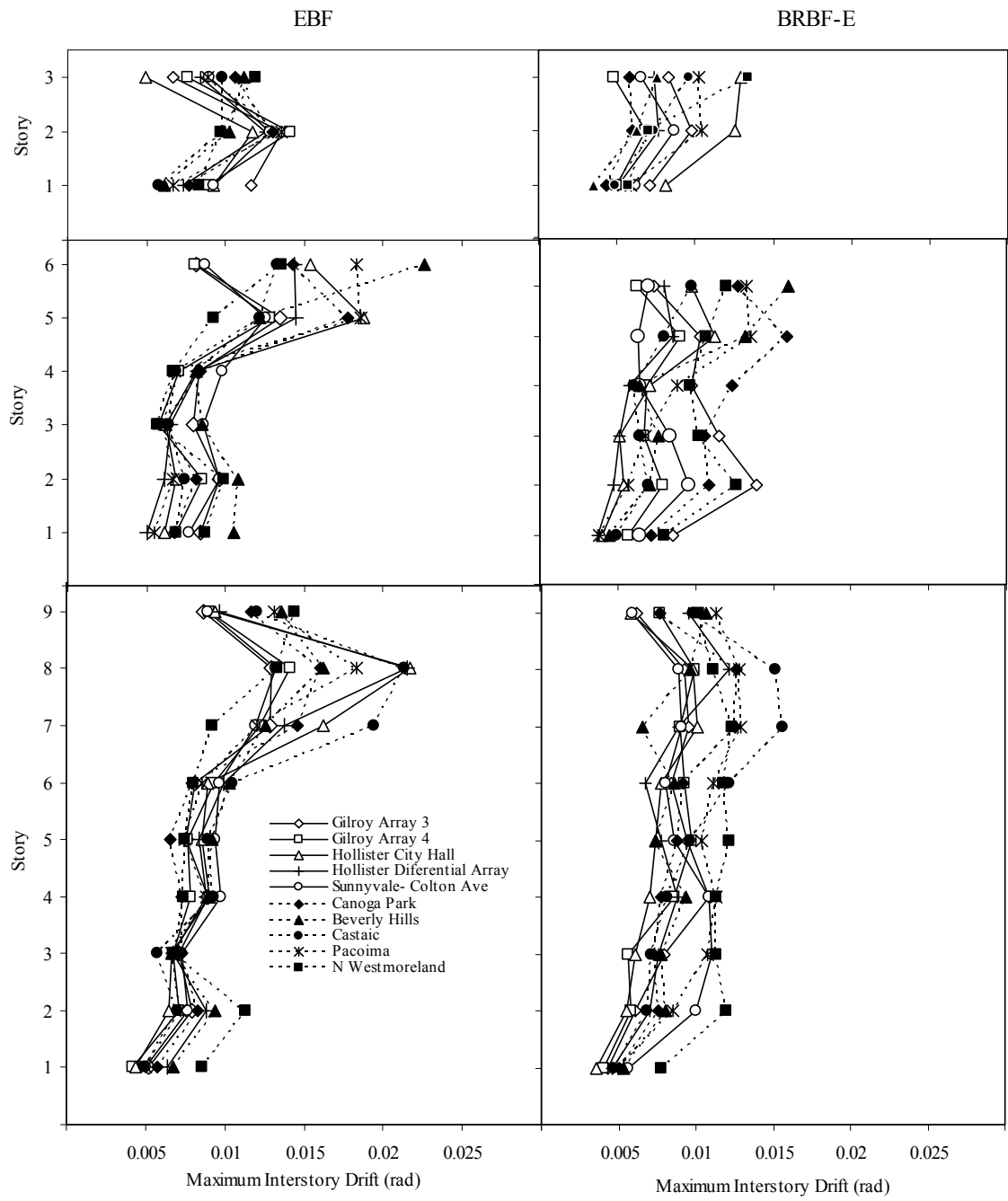
Fig. C-2 Individual story drift responses for EBF and BRBF-Es with 30 ft bay width and strength level I=1.5

149

EBF   BRBF-E
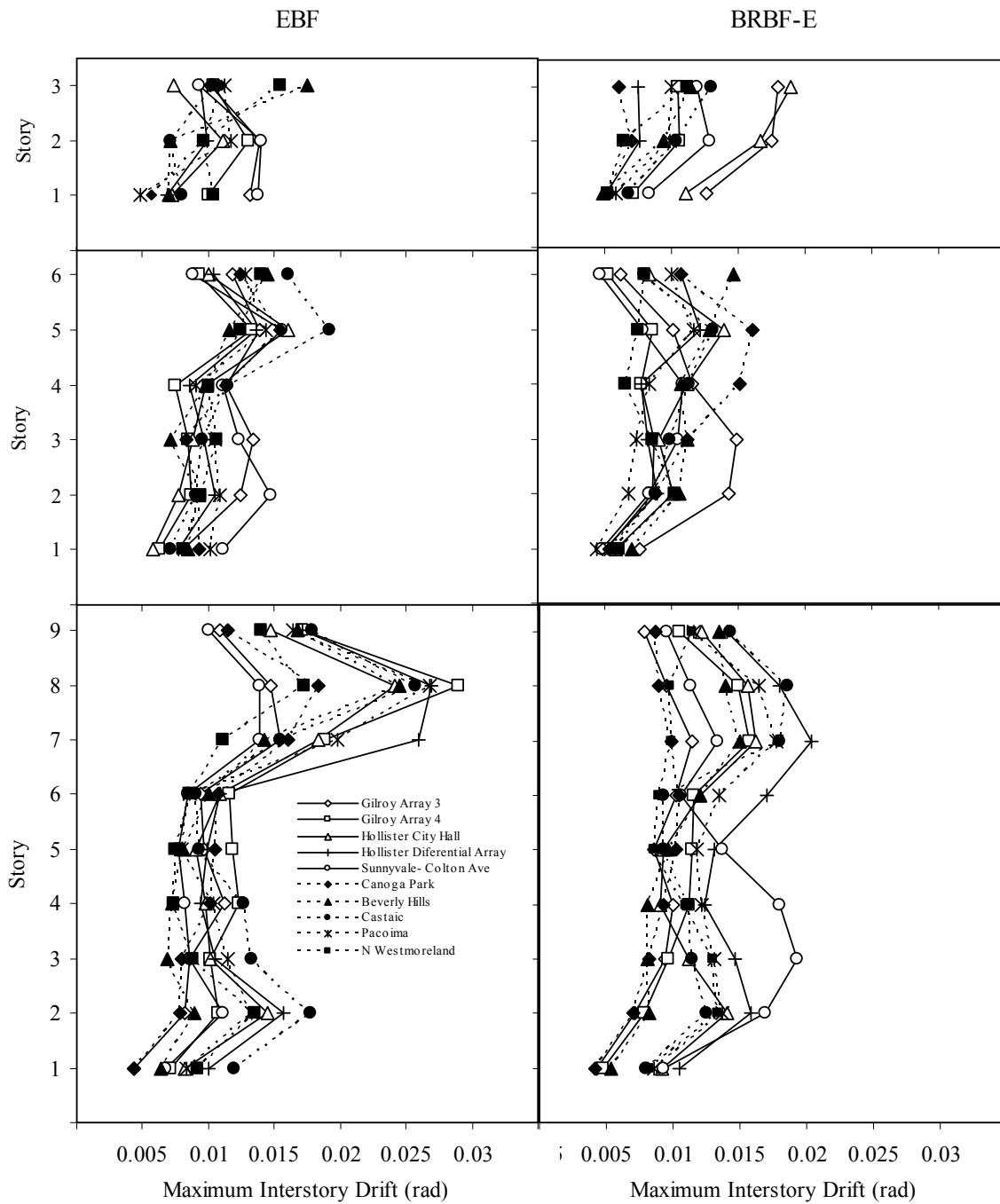
Fig. C-3 Individual story drift responses for EBF and BRBF-Es with 20 ft bay width and strength level I=1

150

EBF   BRBF-E
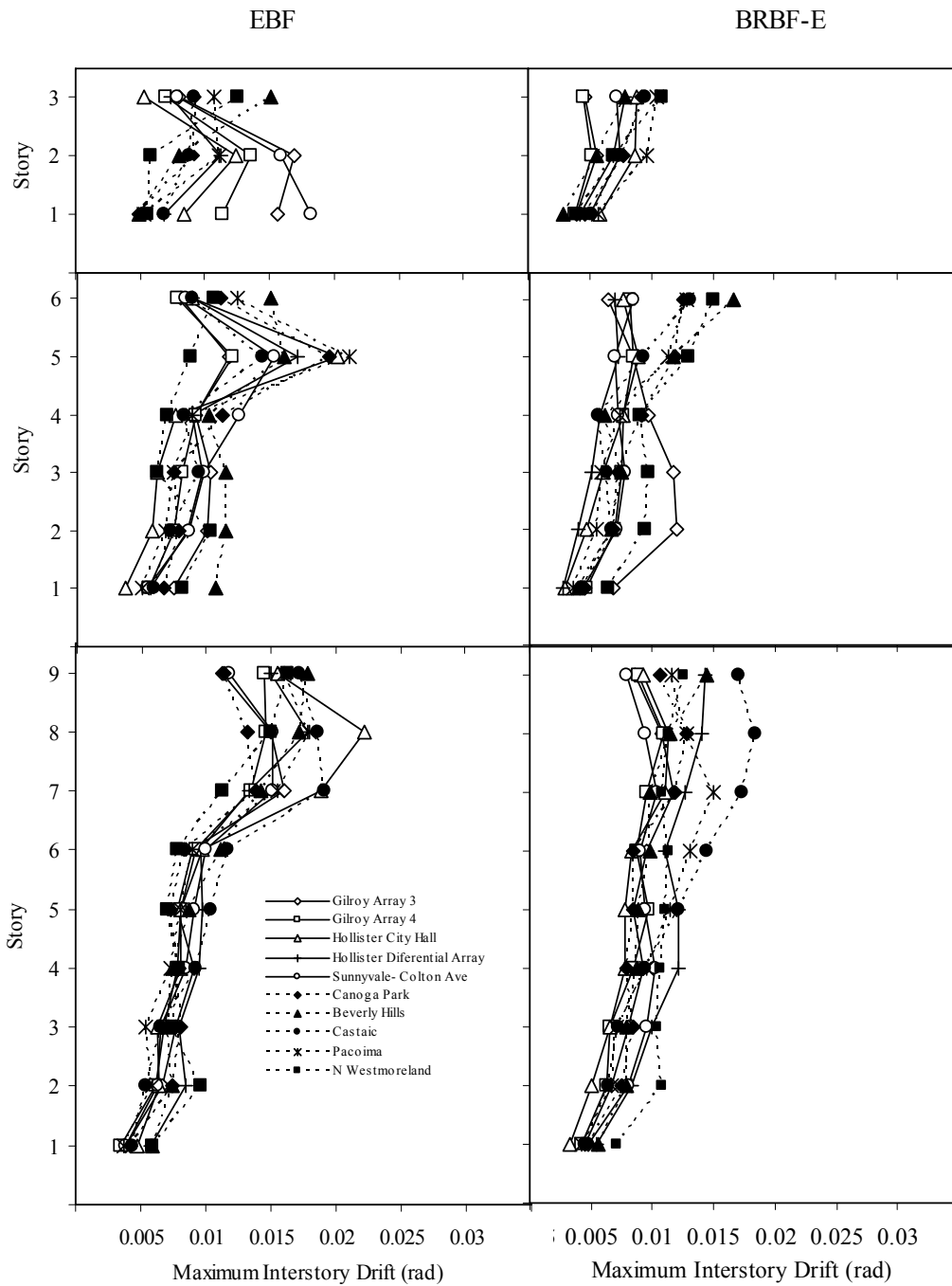
Fig. C-4 Individual story drift responses for EBF and BRBF-Es with 20 ft bay width and strength level I=1.5

151

Appendix D: CALIBRATION OF CONCRETE-SLAB CONSTITUTIVE MODEL

D.1. Description of Concrete Calibration Study

The reduced concrete modulus and yield strength used for the slab model in Chapter 4 were calibrated based on cyclic composite beam tests performed by Jones et al. [64]. Jones et al. tested several composite moment frame specimens under quasi-static cyclic loading, quantifying the system-level behavior of the RBS moment frame connections. Fig. D-1 shows the experimental setup used by [64]. In Fig. D-1, supports were located at the column and beam ends, representing beam and column mid-spans where moment inflection points were expected. The supports at the ends of the beam allowed for horizontal translation, and restricted out-of-plane deformations. A hydraulic loading ram simulated cyclic frame displacements though lateral column displacements. The cyclic loading protocol used to load the frame is presented in Table D-1.

The experimental setup used by [64] was re-created using the finite element program ABAQUS. The ABAQUS model was created to allow direct comparison with experimental specimen DBWWC. Shell elements were used to model all member geometry. The supports used in the experiment were simulated by roller supports on the ends of the beams, a pinned constraint at the column base, and out-of-plane constraints at the beam and column ends. Fig. D-2 shows the ABAQUS model with applied boundary conditions.

To calibrate the concrete constitutive behavior, varying reductions in concrete strength and stiffness were considered in the ABAQUS model, and results were compared with the

experimental test data. Concrete models having stiffness and strength reductions of 0%, 70%, and 100% of the nominal concrete compressive behavior, were considered. The concrete strength and stiffness reductions were to pre-account for damage expected during tension cycles, explicitly modeling the concrete tensile strength degradation is computationally expensive. The performance of each model is discussed next.
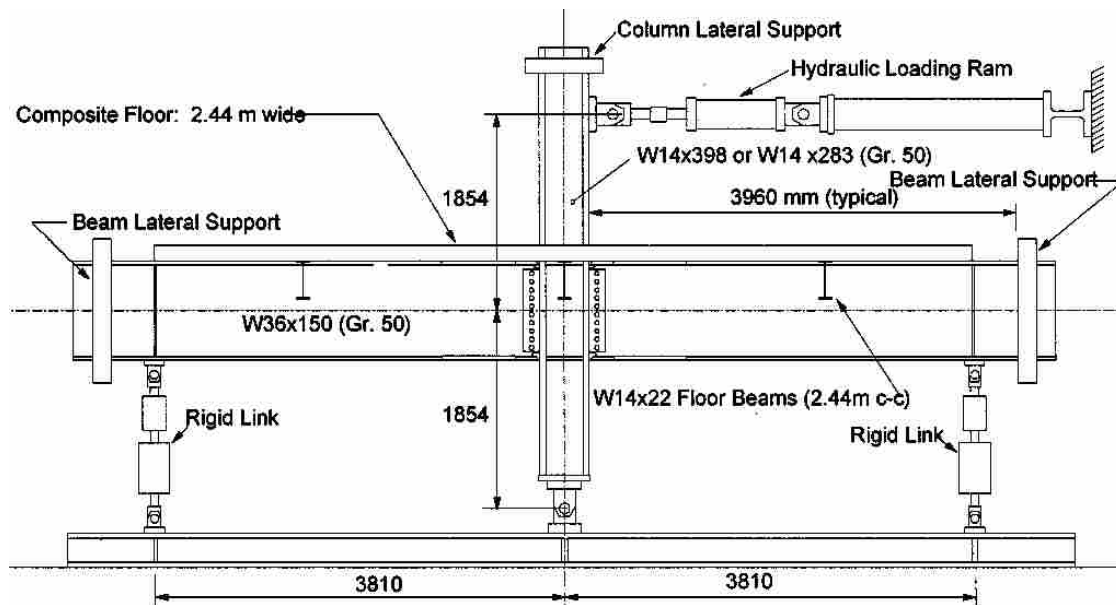
Fig. D-1 Experimental test setup for concrete calibration study [64]

Table D-1: Cyclic Loading Protocol used by Jones et al.

Story Drift Angle (rad)	Number of Loading Cycles
0.00375	6
0.005	6
0.0075	6
0.01	4
0.015	2
0.02	2
0.03	2
0.04	2
0.05	2
0.06*	2

*continue with increments of 0.01 rad with
cycles of loading at each increment
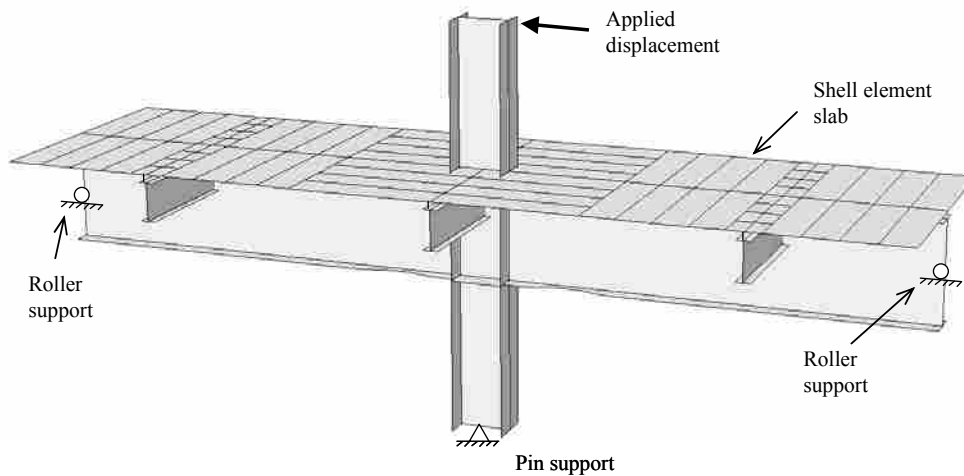
Fig. D-2   ABAQUS model simulating Jones et al. test

D.2. Concrete Calibration Findings

The concrete model having a 70% reduction in strength and stiffness matched the closest with the experimental result. Fig. D-3 shows the hysteretic behavior for specimen DBWWC and the ABAQUS models (having 0%, 70%, and 100% concrete strength reduction).   Similar stiffness, strength, and strength degradation behavior is evident between the experimental result and model with 70% concrete stiffness and strength. The good agreement between model and experiment confirms that modeling composite beams with reduced elastic-perfectly-plastic concrete properties can reasonably predict system-level frame behavior. From Fig. D-3(b) the model with 100% concrete strength significantly over predicted the frame strength, while the model with 0% concrete strength under predicted the frame strength observed in the experimental test.
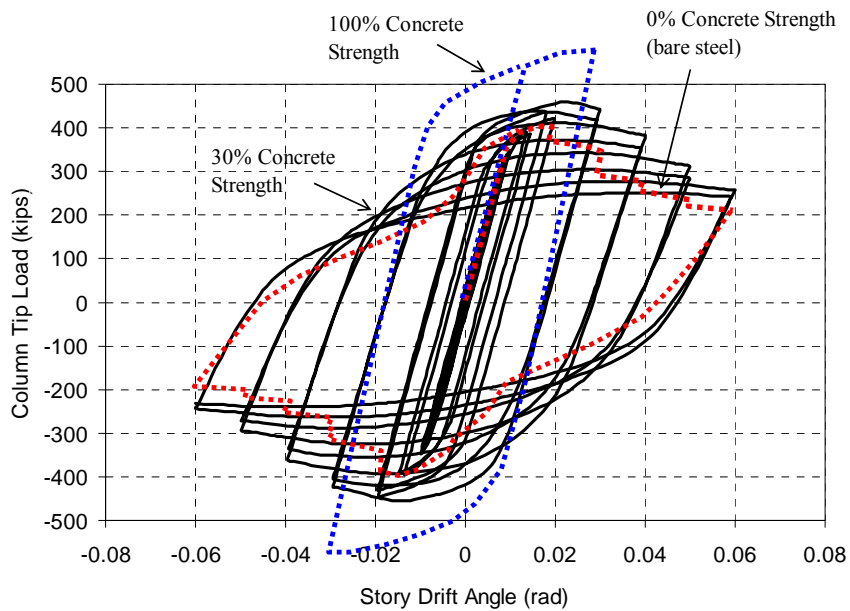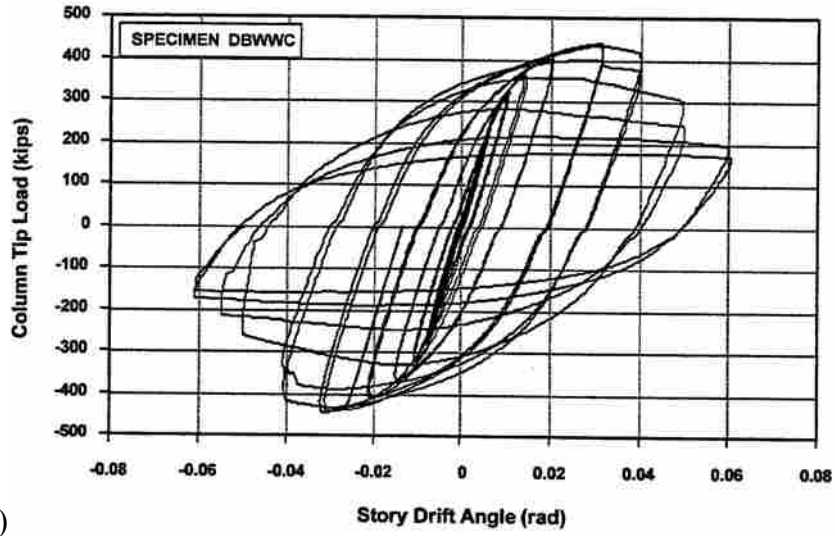
Fig. D-3 Load vs. drift hysteresis for: (a) experiment [64]; and, (b) ABAQUS model

156

Appendix E: CONSTRUCTION DETAILS FOR E-DEFENSE TEST FRAME

Fig. E-1 through Fig. E-17 represent the construction details prepared by E-defense [61], for the five-story BRBF test frame analyzed in Chapter 4. These drawings are provided to describe, in detail, the member sizes and connection details used to create the analytical model described in Chapter 4.
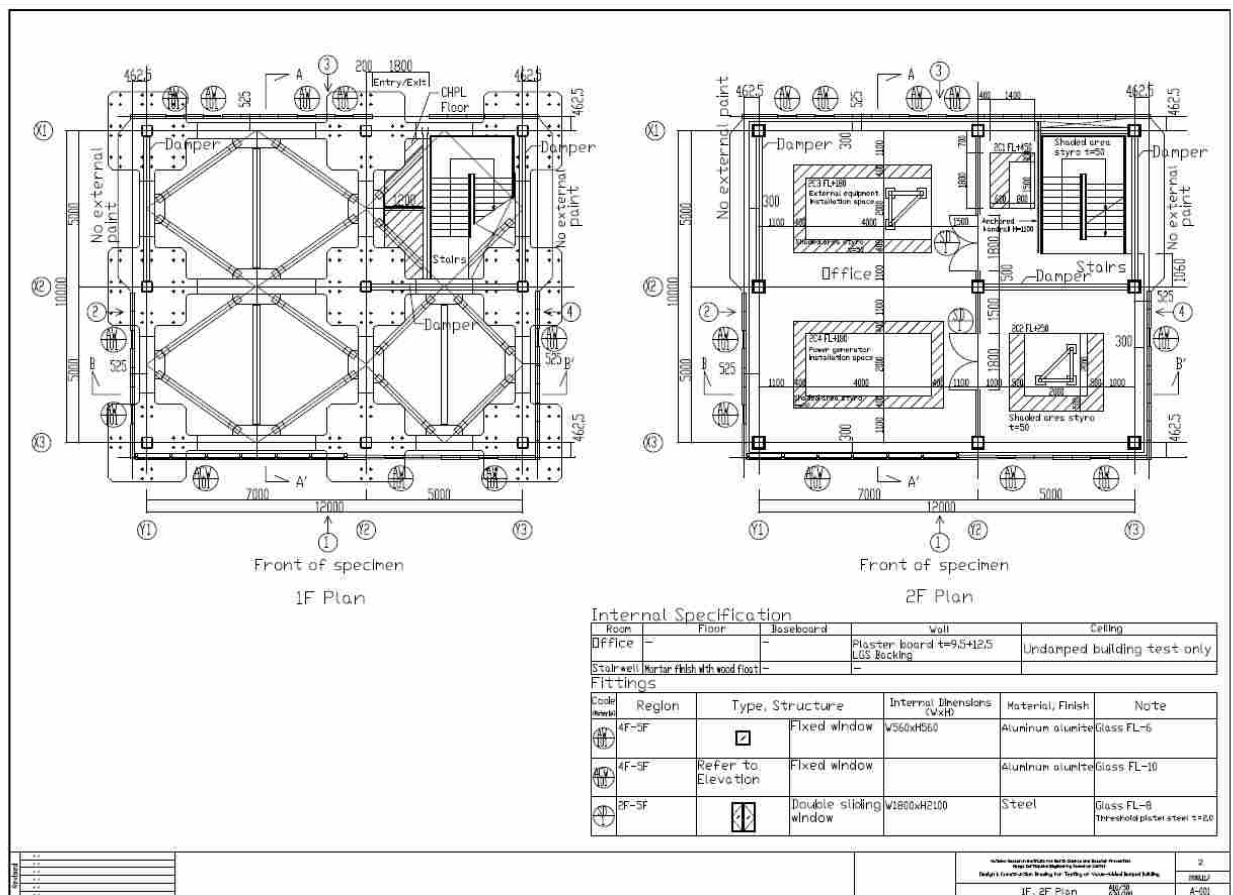
Fig. E-1 E-defense test structure detail, page 2 [61]

Fig. E-2 E-defense test structure detail, page 3 [61]

158

Fig. E-3 E-defense test structure detail, page 4 [61]

159
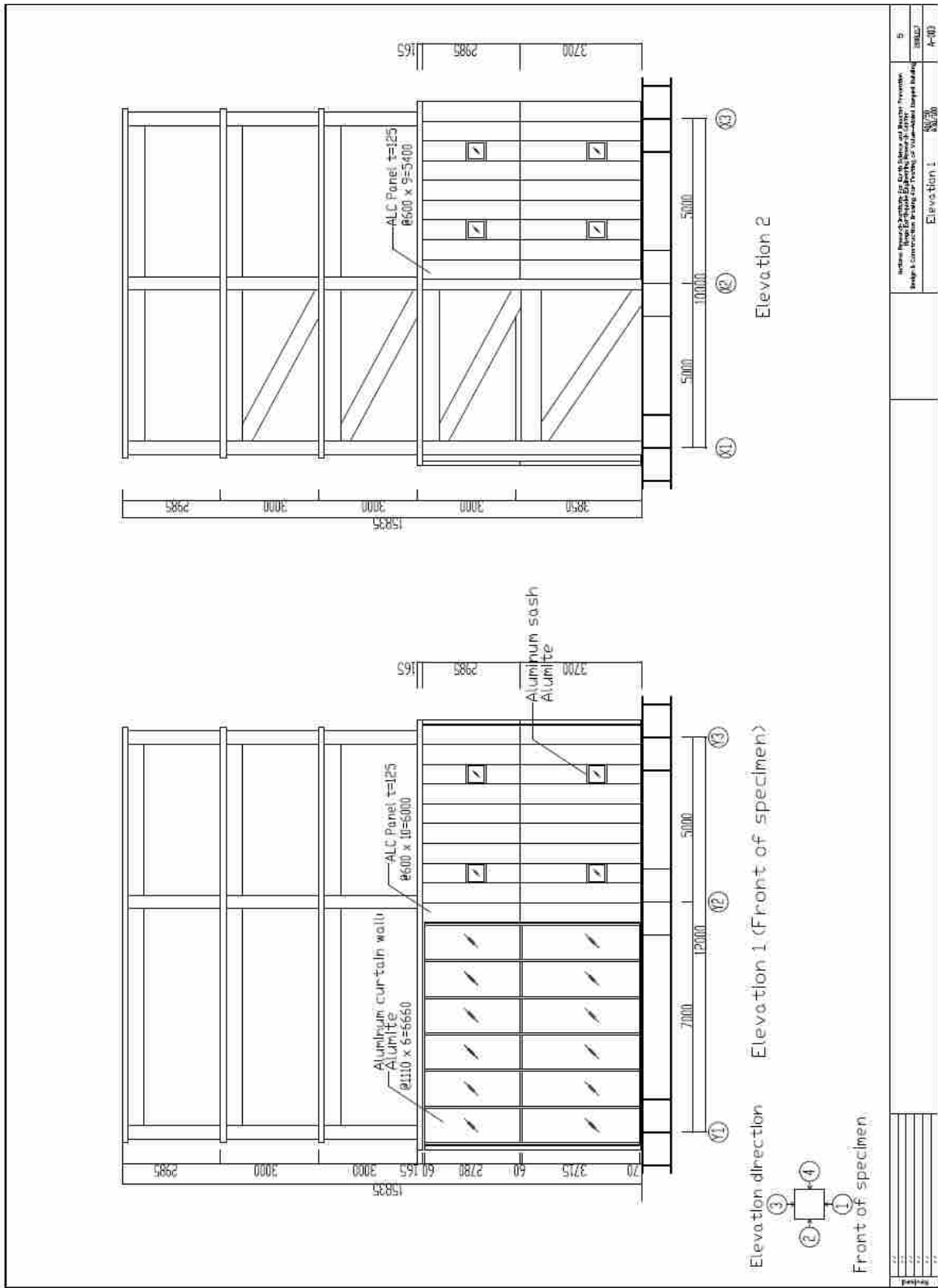
Fig. E-4 E-defense test structure detail, page 5 [61]

160

Fig. E-5 E-defense test structure detail, page 6 [61]

Fig. E-6 E-defense test structure detail, page 7 [61]

Fig. E-7 E-defense test structure detail, page 8 [61]

163

Fig. E-8 E-defense test structure detail, page 12 [61]

Fig. E-9 E-defense test structure detail, page 13 [61]

165

Fig. E-10 E-defense test structure detail, page 14 [61]

166

Fig. E-11 E-defense test structure detail, page 15 [61]

167

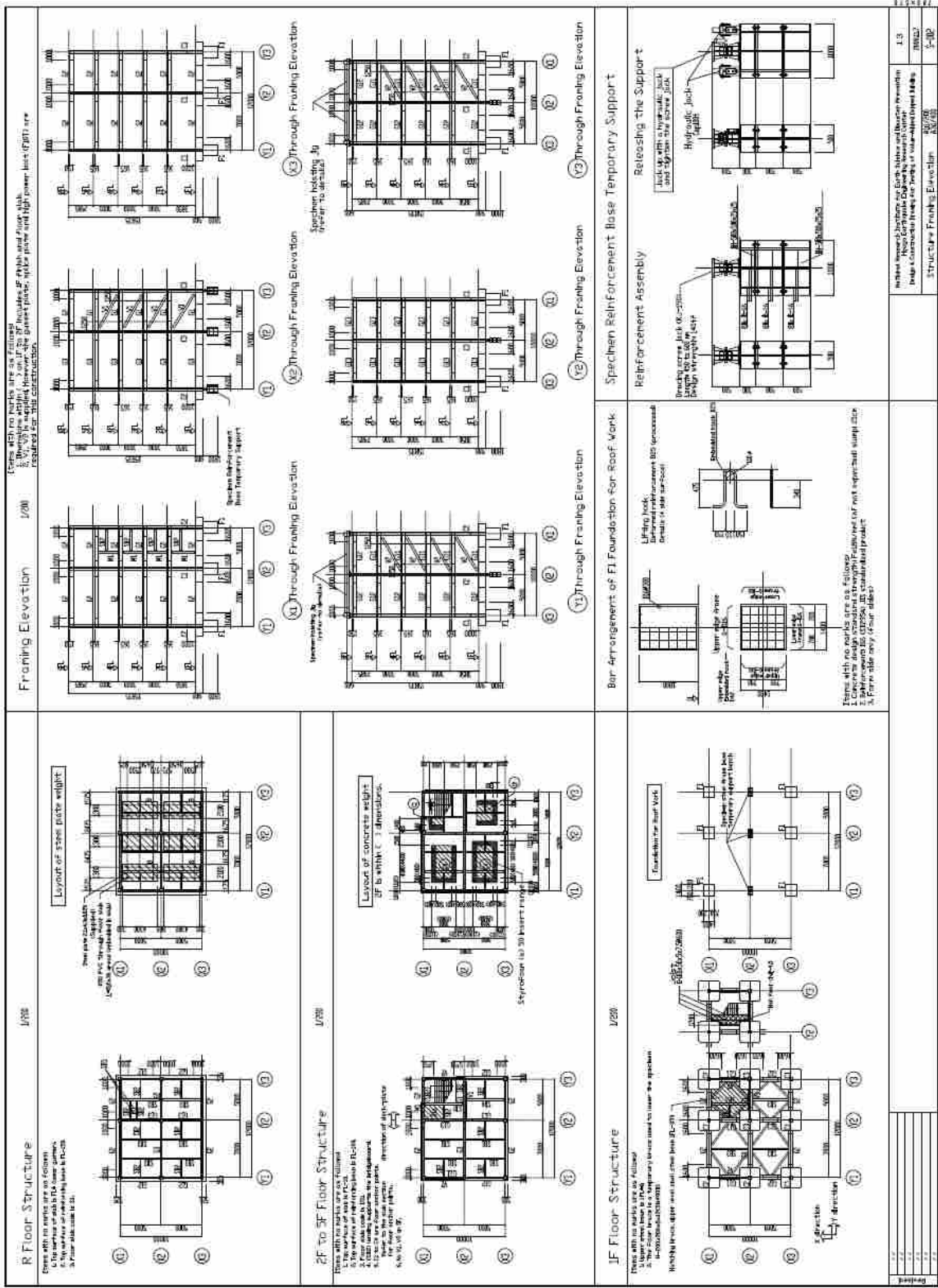Fig. E-12 E-defense test structure detail, page 17 [61]
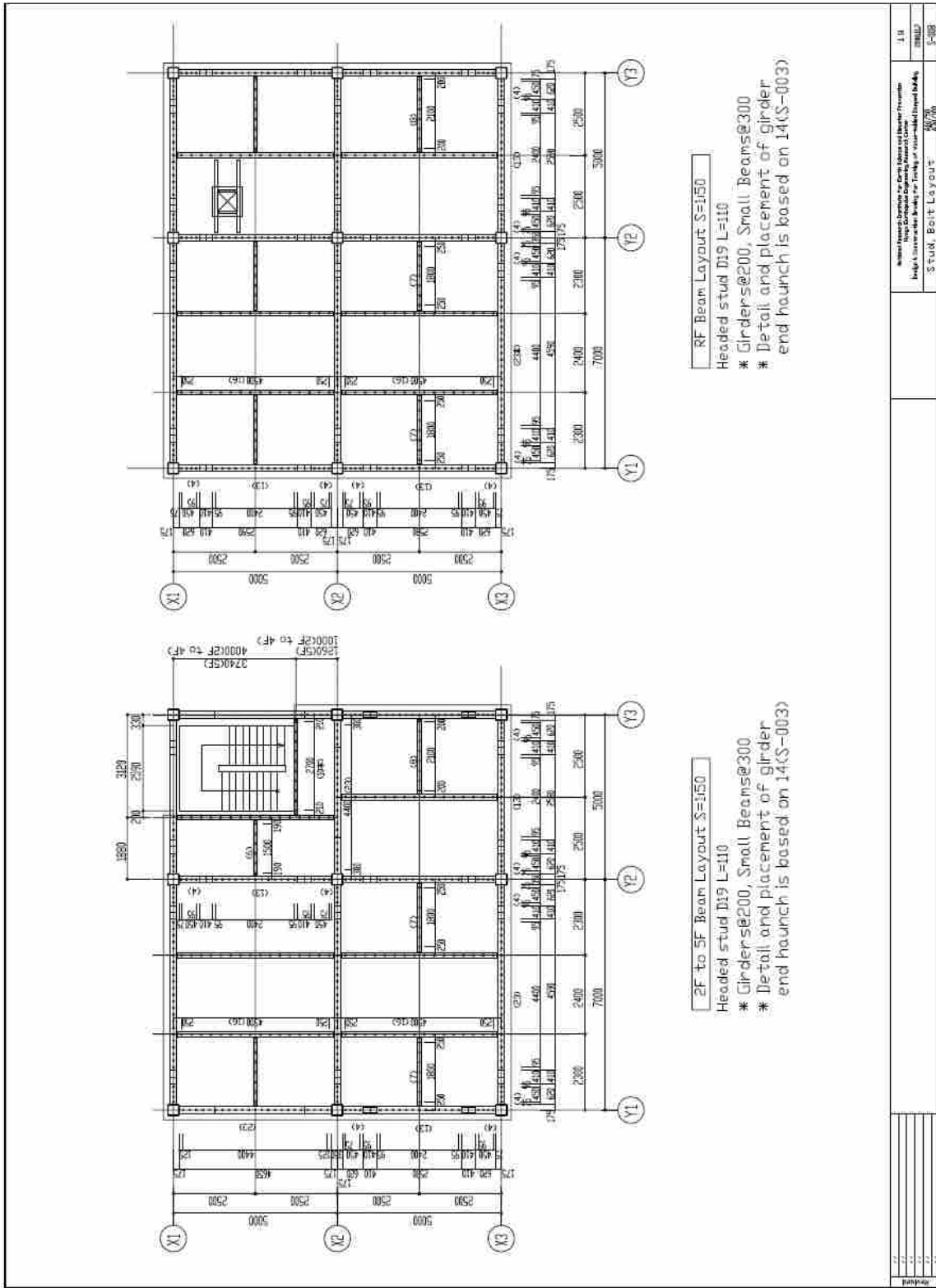
Fig. E-13 E-defense test structure detail, page 18 [61]

Fig. E-14 E-defense test structure detail, page 19 [61]

170

Fig. E-15 E-defense test structure detail, page 20 [61]

Fig. E-16 E-defense test structure detail, page 21 [61]

Fig. E-17 E-defense test structure detail, page 22 [61]